BRNO UNIVERSITY OF TECHNOLOGY

Faculty of Electrical Engineering
and Communication

MASTER'S THESIS

Brno, 2020 Bc. Marek Zemek

BRNO UNIVERSITY OF TECHNOLOGY
VYSOKÉ UČENÍ TECHNICKÉ V BRNĚ

FACULTY OF ELECTRICAL ENGINEERING AND COMMUNICATION
FAKULTA ELEKTROTECHNIKY
A KOMUNIKAČNÍCH TECHNOLOGIÍ

DEPARTMENT OF BIOMEDICAL ENGINEERING
ÚSTAV BIOMEDICÍNSKÉHO INŽENÝRSTVÍ

METHOD FOR EXTENDING THE FIELD OF VIEW FOR X-RAY COMPUTED TOMOGRAPHY WITH SUBMICRON RESOLUTION

METODA ROZŠÍŘENÍ ZORNÉHO POLE PRO RENTGENOVOU VÝPOČETNÍ TOMOGRAFII SE SUBMIKRONOVÝM ROZLIŠENÍM

MASTER'S THESIS
DIPLOMOVÁ PRÁCE

AUTHOR
AUTOR PRÁCE

Bc. Marek Zemek

SUPERVISOR
VEDOUCÍ PRÁCE

Ing. Martin Mézl, Ph.D.

BRNO 2020

BRNO UNIVERSITY OF TECHNOLOGY
FACULTY OF ELECTRICAL ENGINEERING AND COMMUNICATION

Master's Thesis

Master's study program **Biomedical Engineering and Bioinformatics**

Department of Biomedical Engineering

Student: Bc. Marek Zemek ***ID:*** 185960

Year of study: 2 ***Academic year:*** 2019/20

TITLE OF THESIS:

Method for Extending the Field of View for X-ray Computed Tomography with Submicron Resolution

INSTRUCTION:

1) Study the limits of X-ray computed tomography regarding the effect of field-of-view size on practical CT data acquisition, and investigate the formation of related artifacts. 2) Survey the available literature with a focus on field-of-view extension for X-ray computed tomography and tomographic reconstruction of samples larger than the field of view. 3) Propose a method for reconstructing samples larger than the field of view, with a focus on submicron-resolution, and using available hardware or software tools. 4) Implement the proposed method. 5) Evaluate the performance of the proposed method in comparison to selected common solutions. 6) Discuss the results reached, benefits of individual methods, their limits and possibilities of application in specific circumstances.
This work has been assigned in cooperation with CEITEC BUT.

RECOMMENDED LITERATURE:

[1] KAK, Avinash C. a Malcolm SLANEY. Principles of computerized tomographic imaging. Philadelphia: SIAM, 2001. ISBN 978-0-89871-494-4.

[2] HSIEH, Jiang. Computed tomography: principles, design, artifacts, and recent advances. Third edition. Bellingham, Wash., USA: SPIE, 2015. ISBN 978-162-8418-255.

[3] LI, Yinsheng, Yang CHEN, Yining HU, Ahmed OUKILI, Limin LUO, Wufan CHEN a Christine TOUMOULIN. Strategy of computed tomography sinogram inpainting based on sinusoid-like curve decomposition and eigenvector-guided interpolation. JOSA A. 2012, 29(1). DOI: 10.1364/JOSAA.29.000153. ISSN 1084-7529.

Date of project specification: 3.2.2020 ***Deadline for submission:*** 29.5.2020

Supervisor: Ing. Martin Mézl, Ph.D.
Consultant: Ing. Jakub Šalplachta

prof. Ing. Ivo Provazník, Ph.D.
Chair of study program board

ABSTRACT

Computed tomography is a tool for nondestructive evaluation of samples, commonly used in many industrial and scientific fields. Some tomographic devices produce images with sub-micrometer spatial resolution. The field of view of such devices can be very small, in the range of single millimeters or less. This restricts possible sizes of samples, which is a major limitation. Various field-of-view extension techniques exist which are able to overcome this restriction. In this thesis, a previously published technique was adapted and implemented specifically for the Rigaku Nano3DX X-Ray microscope. This technique almost doubles the lateral extent of the field of view without the need for a larger detector array. The approach was tested using both synthetic and real data, and its performance is evaluated subjectively and objectively, through visual inspection and image quality metrics. The evaluation is largely based on comparing images reconstructed using this method to ones acquired using a larger detector array. The field-of-view extension method yields faithful reconstructions of samples, comparable in quality to their larger-detector counterparts.

KEYWORDS

computed tomography, field-of-view extension, offset scan

ABSTRAKT

Výpočetní tomografie je nástroj pro nedestruktivní inspekci vzorků, který je běžně používán v mnoha oblastech průmyslu a výzkumu. Některé tomografické přístroje umožňují snímání obrazů s prostorovým rozlišením pod jeden mikrometr. Zorné pole takovýchto přístrojů bývá malé, v rozsahu jednotek milimetrů či méně. Tím jsou omezeny rozměry vzorků, což je značně limitující. Toto omezení lze překonat pomocí různých technik pro rozšíření zorného pole. Jedna takováto dříve publikovaná metoda byla v této práci upravena a implementována pro přístroj Rigaku Nano3DX. Tato technika téměř zdvojnásobuje zorné pole přístroje bez nutnosti většího detektoru. Implementovaný přístup byl testován pomocí umělých i skutečných dat, a jeho účinnost byla zhodnocena subjektivně i objektivně, pomocí vizuální kontroly a metrik kvality obrazu. Hodnocení je převážně založeno na srovnání obrazů rekonstruovaných pomocí této metody s obrazy získanými pomocí většího detektoru. Implementovaná technika rozšíření zorného pole poskytuje věrné rekonstrukce vzorku, srovnatelné se zmíněnými protějšky.

KLÍČOVÁ SLOVA

výpočetní tomografie, rozšíření zorného pole, vychýlené snímání

ZEMEK, Marek. *Method for Extending the Field of View for X-ray Computed Tomography with Submicron Resolution*. Brno, Rok, 89 p. Master's Thesis. Brno University of Technology, Faculty of Electrical Engineering and Communication, Department of Biomedical Engineering. Advised by Ing. Martin Mézl, Ph.D.

ROZŠÍŘENÝ ABSTRAKT

Výpočetní tomografie (Computed Tomography, CT) je nástroj pro nedestruktivní zobrazení vnitřních struktur vzorků. Tento nástroj je znám především v oblasti medicíny, ale často je využíván i v mnoha sférách průmyslu a výzkumu. Principem transmisní CT je akvizice velkého počtu projekcí pod různými úhly kolem vzorku. Vzorek je vystaven proudu energie, nejčastěji elektromagnetického vlnění v podobě rentgenových paprsků. Rentgenový svazek je utlumen strukturami vzorku a zachycen detektorem na druhé straně. Z těchto projekčních dat je pak pomocí takzvaného rekonstrukčního algoritmu vytvořen obraz příčného řezu vzorkem.

Značným omezením CT je rozsah zorného pole (field of view, FoV) přístroje, který je závislý na velikosti použitého detektoru a limituje rozměry snímaných vzorků. Toto omezení se projevuje zejména u CT přístrojů s vysokým rozlišením, jejichž FoV jsou velmi malá, řádově v jednotkách milimetrů. Z tohoto důvodu byla vyvinuta celá řada technik pro rozšíření FoV a snímání vzorků větších než je snímací plocha použitého detektoru.

Tato práce se zabývá laterálním rozšířením FoV přístroje Rigaku Nano3DX. Kapitoly 1 a 2 rekapitulují proces akvizice dat a tomografické rekonstrukce. Kapitola 3 je stručným výčtem metod pro rozšíření FoV dostupných v literatuře. V kapitole 4 je vybraná metoda pro laterální rozšíření FoV upravena a implementována pro přístroj Nano3DX. Tato metoda je následně testována na umělých i skutečných datech, a její výsledky jsou hodnoceny subjektivně i objektivně.

Pro laterální rozšíření FoV přístroje Nano3DX byla vybrána metoda, u které je využito vychýlení osy rotace (axis of rotation, AoR). Takováto metoda je vhodná pro svou relativní jednoduchost a snadnou implementaci v porovnání s ostatními způsoby rozšíření FoV. Vyžaduje pouze jediné měření v úhlovém rozsahu 2π a zprostředkovává FoV takřka dvakrát širší, než je šířka snímací plochy použitého detektoru. K odchylkám způsobeným posunem AoR mezi měřeními, ke kterým může docházet u některých jiných technik, zde nedochází. Hlavním omezením této metody je maximální míra rozšíření FoV, ale tento nedostatek je vykoupen snazším zpracováním měřených dat. V následujícím textu na tuto metodu odkazuje název „vychýlený scan.“

Metoda vychýleného scanu se skládá z několika kroků. Prvním z nich je akvizice projekcí vzorku s vychýlenou AoR. Dále je v těchto projekcích nalezena pozice, na kterou se AoR promítá. Toto je důležitý parametr pro CT rekonstrukci obecně a odchylky způsobují artefakty v rekonstruovaných obrazech. V této práci je doporučen poloautomatický přístup, při němž je pozice AoR nejdříve odhadnuta automatickým algoritmem a následně je manuálně zkontrolována a v případě potřeby korigována. K prvotnímu odhadu lze přitom využít jeden ze dvou přístupů zde popsaných a implementovaných. První z těchto přístupů je založen na symetrii sinogramu podle

AoR, druhý vybírá vhodnou pozici této osy pomocí objektivního hodnocení rekonstruovaných obrazů.

Data jsou pak transformována na virtuální detektor, u kterého je paprsek protínající osu rotace v pravém úhlu ortogonální s plochou detektoru. Tento krok je nutný kvůli vybranému rekonstrukčního algoritmu, který takovéto uspořádání předpokládá. Virtuální detektor je vůči reálnému pootočen o určitý úhel, závislý na pozici AoR.

Po transformaci jsou data kolem AoR váhována, čímž je eliminován vliv přebytečnosti dat v této oblasti. Rentgenové paprsky v úzkém okolí AoR jsou během akvizice změřeny dvakrát, zatímco v okrajových oblastech jsou data změřena pouze jednou. Váhování je realizováno pomocí váhovací funkce tvaru sinusoidy, která nabývá hodnot v rozsahu jedna až nula. Tato váhovací funkce váhuje data tak, aby se suma vah dvou bodů se stejnou informací vždy rovnala jedné. Paprskům změřeným pouze jednou je přidělena jednotková váha. Plynulý průběh váhovací funkce brání vzniku artefaktů v rekonstruovaném obraze, způsobených ostrými přechody mezi úrovněmi šedi.

Takto upravená data jsou doplněna nulovými hodnotami tak, aby se projekce AoR nacházela v jejich středu. Posledním krokem je samotná rekonstrukce, ke které je využit analytický algoritmus Feldkamp-Davis-Kress. Jedná se o široce používaný algoritmus pro rekonstrukci z projekcí kuželového rentgenového svazku.

Testování metody se skládalo z rekonstrukce a následného hodnocení umělých i reálných dat. Testy metody vychýleného scanu byly nejdříve provedeny na projekčních datech pěti umělých obrazů. Prvním z nich byl fantom obsahující páry čar o různé šířce. Zbylé čtyři byly tvořeny různě složitými obrazci. Z každého obrazu byl vytvořen soubor projekcí simulující akvizici přístrojem Nano3DX při vychýlené AoR. Na tyto soubory projekcí byl aplikován navržený postup, čímž byly získány tomografické řezy. Následně byl pro všech pět vzorků vytvořen druhý soubor, simulující podobnou akviziční geometrii, ovšem bez vychýlení AoR a se širším detektorem. Tato data byla rekonstruována běžným způsobem a výsledné řezy sloužily jako zlatý standard, tedy rekonstrukce bez vychýlení AoR.

Pro ověření funkčnosti metody na skutečných datech byly vybrány tři vzorky: dílek plastové stavebnice, tabletka a polyetylénová destička s příměsí uhlíkových vláken. U každého z těchto vzorků bylo provedeno CT měření s vychýlenou AoR a rekonstrukce pomocí navržené metody. Při tomto měření byl detektor vybaven optickým členem s nominálním FoV 3.6×2.8 mm^2, které bylo vychýlením laterálně rozšířeno 1.8-krát. Rovněž bylo u všech vzorků provedeno druhé, standardní měření s optickým členem s větším FoV, a to 7.2×5.6 mm^2. Tato měření opět sloužila jako referenční a pro jejich rekonstrukci byl použit konvenční rekonstrukční algoritmus. Vzorky byly voleny tak, aby přesahovaly FoV detektoru s menší optikou, ale

aby nepřesahovaly FoV rozšířené vychýlením AoR. Použitá optika s menším FoV umožňuje menší efektivní velikost pixelu. Proto byl na data s vychýlemným AoR aplikován binning, díky čemuž byla výsledná velikost pixelu obou optik srovnatelná.

Pro objektivní hodnocení simulovaných dat byly použity metriky *peak signal-to-noise ratio* (PSNR) a *Feature Similarity Index* (FSIM). PSNR bylo vybráno pro svou jednoduchost, zatímco FSIM umožňuje sofistikovanější hodnocení vycházející z vlastností lidského zraku. V případě reálných dat, kdy není k dispozici nezkreslený původní obraz, byl použit *Natural Image Quality Evaluator* (NIQE). Metriky byly použity k porovnání kvality běžných rekonstrukcí s velkým FoV a rekonstrukcí dat pořízených pomocí menšího detektoru a vychýleného AoR. Výsledky umělých i reálných dat byly rovněž hodnoceny subjektivně. Hodnocena byla především vizuální podoba řezů získaných konvenčním způsobem a pomocí vychýleného scanu.

Objektivní metriky v případě umělých dat naznačují, že navržená metoda produkuje rekonstrukce, které jsou kvalitou velmi blízké referenčním datům s větším FoV. To samé platí i pro subjektivní hodnocení, při kterém nebyly zjištěny žádné výrazné odchylky od referenčních dat. Na základě hodnocení dosaženého prostorového rozlišení s využitím vytvořeného fantomu bylo zjištěno, že navržená metoda pro rozšíření FoV zachovává prostorové rozlišení vůči refenčnímu měření.

Také u rekonstrukcí reálných dat byly hodnoty metriky NIQE velmi podobné pro rekonstrukce vychýleného a běžného scanu. Výsledky obou si tedy jsou objektivně velmi blízké. Při subjektivním hodnocení rovněž nebyly mezi oběma typy rekonstrukce shledány výrazné rozdíly. Vedlejším efektem u dat vychýleného scanu byl díky binningu kratší expoziční čas a snížený výskyt prstencových artefaktů. Další možnou aplikací vychýleného scanu je snímání dat bez aplikace binningu a tudíž rekonstrukce s rozšířeným FoV a současně vysokým rozlišením.

Navržená metoda pro rozšíření FoV je tedy jednoduše implementovatelná a díky tomu rozšiřuje možnosti přístroje Nano3DX. Dosažené zorné pole u praktických testů metody činilo až 1.8-násobek původního FoV. Dalšími možnými kroky ke zdokonalení navržené metody jsou integrace s ostatními existujícími metodami měření či optimizace založená na testování v praktickém provozu.

DECLARATION

I declare that I have written the Master's Thesis titled "Method for Extending the Field of View for X-ray Computed Tomography with Submicron Resolution" independently, under the guidance of the advisor and using exclusively the technical references and other sources of information cited in the thesis and listed in the comprehensive bibliography at the end of the thesis.

As the author I furthermore declare that, with respect to the creation of this Master's Thesis, I have not infringed any copyright or violated anyone's personal and/or ownership rights. In this context, I am fully aware of the consequences of breaking Regulation § 11 of the Copyright Act No. 121/2000 Coll. of the Czech Republic, as amended, and of any breach of rights related to intellectual property or introduced within amendments to relevant Acts such as the Intellectual Property Act or the Criminal Code, Act No. 40/2009 Coll., Section 2, Head VI, Part 4.

Brno ....

author's signature

ACKNOWLEDGEMENT

I would like to thank my supervisor, Ing. Martin Mézl, Ph.D., and my consultant, Ing. Jakub Šalplachta, for their valuable mentoring, helpful consulting, patience, insightful suggestions, and tremendous help during my work on this thesis. I would also like to thank Dr. Yoshihiro Takeda and Dr. Kazuhiko Omote for their kind help and indispensable insight into the inner workings of the hardware I worked with while developing this thesis, as well as during my internship in their X-ray research laboratory. My sincere thanks go out to my family for their unwavering support throughout my studies. Finally, I thank everybody in the laboratory of X-ray micro and nano computed tomography at CEITEC BUT, and especially prof. Ing. Jozef Kaiser, PhD. and Ing. Tomáš Zikmund, PhD., for their support and for having me as part of the team.

I acknowledge that parts of this work were carried out under the project CEITEC 2020 (LQ1601) with financial support from the Ministry of Education, Youth and Sports of the Czech Republic under the National Sustainability Programme II and CzechNanoLab Research Infrastructure supported by MEYS CR (LM2018110).

Contents

List of Figures

List of Tables

Introduction

Computed tomography (CT) is a powerful *nondestructive evaluation* (NDE) tool capable of visualizing internal features of samples. While it is most known for its application in medicine, it has also been utilized in various industrial and scientific fields. In transmission CT, a range of projection images from various angles is acquired for by illuminating a sample by a beam of energy, such as X-rays, and detecting the attenuated beam on the other side. A reconstruction algorithm is then used to retrieve cross-sectional images of the scanned sample from the recorded data. [1, 2]

The task of CT reconstruction can generally be approached in two ways. One is based on linear algebra, and turns the reconstruction process into a problem of solving a set of linear equations. An iterative method is applied to find the solution. Such a method allows the incorporation of noise statistics and prior information about the sample into the reconstruction process, improving the result. The downside of this type of algorithms is the considerable computational cost, even for modestly sized datasets. Computer hardware has only recently become powerful enough to allow for a more widespread adoption of these iterative methods. [3]

The second reconstruction approach is currently more common. Referred to as analytic reconstruction, it is based mainly on Fourier analysis, and requires only a single pass to form a cross-sectional image from projections. The computational cost of this approach is much lower compared to iterative schemes. On the other hand, analytic algorithms were originally formulated for noiseless, continuous data, and may perform poorly in some cases due to sparse sampling, noise, or misalignment of the CT scanner. Nevertheless, these methods offer reasonable performance when the quality of projection data is good. [3]

A major limitation of CT is the extent of a scanner's *field of view* (FoV), which in many modern scanners depends on the size of the detector array used. This imposes considerable restrictions on the size of samples, particularly in high-resolution CT, where FoV sizes are often minuscule. [4] Various FoV extension techniques have been developed to mitigate this and allow for reconstructions of samples that are larger than the physical detector of the scanner used. [5, 6, 7, 8, 9]

The aim of this work is to propose and implement a FoV extension method for the Rigaku Nano3DX X-ray microscope. This method is then tested on synthetic and real data to validate its efficacy. This thesis is divided into several parts. The process of projection acquisition and CT reconstruction is outlined in chapter 1 and chapter 2, respectively. Then, a brief summary of various FoV extension methods is given in chapter 3. Chapter 4 describes the implementation of a FoV method for the Nano3DX, as well as a rationale for why this particular method was chosen.

The FoV is extended laterally to accommodate samples almost twice as wide as the scanner's detector array. The final part of this chapter describes test results of this method on synthetic and real data, using subjective evaluation and objective metrics.

1 X-ray Computed Tomography

1.1 Nondestructive X-ray Imaging

The ability to visualize an object's internal structure without compromising its integrity is very useful in many circumstances. Techniques that accomplish this task are referred to as NDE or noninvasive measurement, among others. Various imaging modalities are used for NDE. Perhaps the most prominent of these is the group of techniques utilizing X-rays. [1] This group is also the one most relevant to this work.

X-rays, like visible light, are quanta of electromagnetic radiation called photons. The difference is that X-ray photons carry much higher amounts of energy – roughly 100 electron volts (eV) or more. That is at least two orders of magnitude more than visible light. [1] Some sources also specify an upper bound – usually around 100 keV – and label higher-energy radiation as γ rays. [10] Others distinguish high-energy X-rays and γ rays by how the two are formed. The former are said to come from the interaction of accelerated electrons with matter, while the latter are created by radioactivity or other means. [1]

Electromagnetic radiation can be described in terms of its wavelength λ , frequency f, or energy E, are related as follows:

$$E = hf = \frac{hc}{\lambda}, \tag{1.1}$$

where h is Planck's constant ($6.626 \cdot 10^{-34}\, Js$), and c is the speed of light in vacuum (roughly $2.9979 \cdot 10^{8}\ ms^{-1}$). The upper bound of X-ray wavelengths is around 10 nanometers or less, corresponding to frequencies of 20 Terahertz or more. [1, 10]

The X-rays' high energy allows them to penetrate objects fairly easily. When the rays travel through an object, they are attenuated by interacting with materials inside it. [1, 2] X-rays interact with atoms of materials primarily through physical phenomena known as Rayleigh scattering, Compton scattering, and the photoelectric effect. [2]

The rate at which a single-energy (monochromatic) X-ray beam is attenuated by traveling through a homogeneous material is expressed in terms of the linear attenuation coefficient, µ $[m^{-1}]$. Different materials absorb X-rays at different rates, so the imaged object may be modeled as a function of µ in space. [2, 11] The value of µ is also influenced by the material's density and by the energy of the X-ray beam. [2] The intensity I of a monochromatic X-ray beam at point r_1 along its path is expressed in terms of Beer's law:

$$I = I_0 \exp\left(-\int_0^{r_1} \mu(r)dr\right), \tag{1.2}$$

where I_0 is the beam's initial intensity. [2] This means that rays are attenuated exponentially. A logarithmic operation may then be applied to isolate the attenuation value in the exponent:

$$A = -\ln\left(\frac{I}{I_0}\right) = \int_0^{r_1} \mu(r)dr. \tag{1.3}$$

Real X-ray sources are not monochromatic, but rather produce rays with a range of different energies. Nevertheless, eq. (1.2) is commonly used as an approximation. [2]

The X-rays' penetrative ability has lead to their utilization for many NDE purposes. The most basic X-ray imaging modality is planar X-ray radiography, or attenuation transmission imaging. [1] X-rays are generated on one side of a sample and detected on the other, after being attenuated by the materials in their path. In radiography, information about the three-dimensional sample is projected onto a two-dimensional detector plane. [1, 2] This forms an image that is immediately viewable without any need for post-processing or reconstruction. The values of the image, however, depend on the total attenuation of the X-ray beams along their path from source to detector. Put differently, a single value in the image depends on both the length of a ray's path and on the values of μ along that path. This makes assessment of the radiograph difficult when no prior knowledge about the imaged object is available. [2]

X-ray CT remedies this limitation of planar radiography. CT is an NDE technique that produces cross-sectional images of a sample from what is essentially a set of radiographic images, projections, acquired at various angles. The cross-sectional image is not readily available for viewing after the acquisition process; the projections need to go through a mathematical operation known as tomographic reconstruction. Since these projections are scanned along a circular path, they are often expressed as a function of angle relative to a reference direction. [1, 11]

X-ray imaging techniques, including CT, are used in a number of fields, most notably medicine and industry. Medical applications are aimed at diagnosis of diseases, as well as image-guided intervention. [12] The use of X-ray imaging in medicine is constrained by the need to keep acquisition times short and radiation doses absorbed by patients low. [2] CT scanners are built with patient comfort in mind – the source and detector rotate around a stationary patient. Voxel resolutions are usually in the range of millimeters to hundreds of micrometers. In contrast to industrial applications, the range of energies used is quite narrow, most commonly around 100 keV. [1, 13] Multiple different geometries and scanner configurations are used, each designed for specific use cases. [2]

In industrial applications, samples vary widely in terms of shape, size, composition, and other characteristics, which means that the CT hardware used is also much more varied. Unlike in medicine, dose is often of less concern here. Scan

times are usually longer, with the exception of some inline applications. Resolutions of industrial CT scanners are varied; depending on sample size and level of detail required in images, voxel sizes can range between hundreds of nanometers to single centimeters. Values of energies used vary widely, depending on the size and chemical makeup of the sample. In general, energies between tens and low hundreds of keV are used, but X-ray imaging in the MeV range is not unheard of. [1, 4, 13]

X-ray-based NDE methods, including CT, are an invaluable tool for scientific research, too. The range of sample sizes and materials is similar to what has been mentioned for the industrial area, meaning the scanners used for research are similarly varied. [1, 4, 13] The throughput required in research is often much lower than in industry and medicine.

1.2 CT Scanner Hardware and Geometry

A variety of CT scanners has been developed for the purpose of acquiring projections suitable for CT reconstruction. These scanners typically take the form of one of several common form factors. [2] All of them, however, consist of the same core components. At the center is a sample stage, a place to situate the scanned object. It is flanked by an X-ray source on one side, and a detector on the other; these two components are usually static relative to one another. The last crucial component is a mechanism for rotating the source-detector system around the sample. Note that rotation of the source-detector pair around a static sample is equivalent to rotation of the sample in between a static source and detector. [1]

An X-ray tube is typically used to generate X-rays in CT scanners. This is an evacuated tube, in which electrons are emitted from a heated filament at the cathode end, and accelerated onto an anode by high voltage. The electron beam is focused onto a small area on the anode called the focal spot. Upon hitting this spot, electrons are stopped by the material of the anode, and a fraction of their energy is converted into X-rays; the rest turns into heat. [1, 2]

Voltages between the two electrodes of an X-ray tube are generally in the order of tens to hundreds of kilovolts (kV), and are directly proportional to the maximum energy of generated X-rays. Higher-energy radiation is said to be "harder," and tends to penetrate denser and thicker materials with greater ease. This means that higher anode voltages can be used for imaging larger samples or samples composed of heavier elements. [2]

The energy spectrum of the generated X-ray beam consists of two components: wide-band braking radiation (commonly called by the German *bremsstrahlung*), and lines of characteristic radiation. The name of the second component comes from the fact that the spectral positions of these lines are specific to the material of the anode.

The shape of the spectrum depends on the tube voltage, as well as on filtration – placing layers of various materials in the beam's way (fig. 1.1). [1, 2]

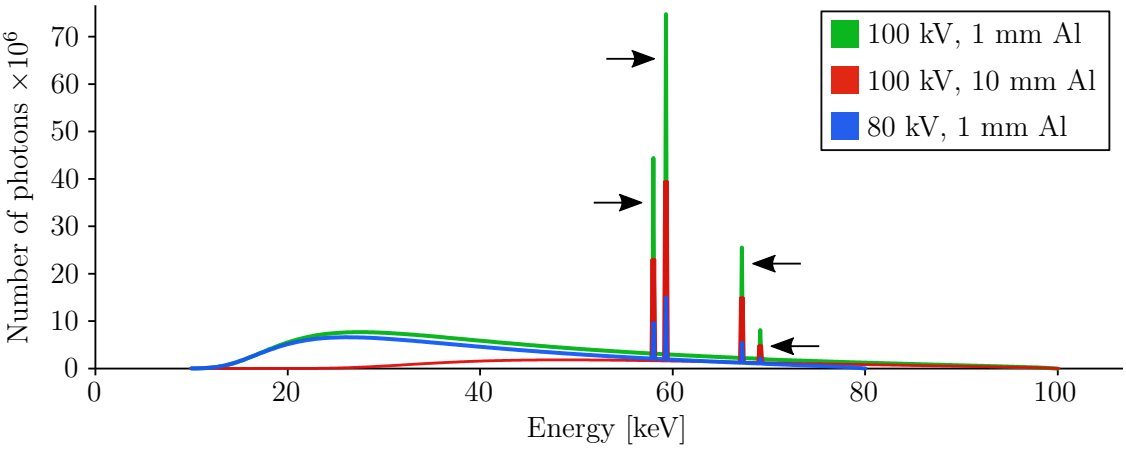

Fig. 1.1: An example of three energy spectra of X-rays generated by a Tungsten anode. Tube voltage for the green and red spectra was 100 kV, with the former filtered by a 1 mm Al sheet, and the latter by 10 mm of Al. Tube voltage for the blue spectrum was 80 kV, and the beam was filtered by 1 mm of Al. All spectra were measured 1 meter from the anode, meaning the rays were additionally filtered by a meter of air. Peaks of characteristic radiation are marked by arrows. The spectra were simulated using the program *SpekCalc* [14, 15, 16].

Another key parameter besides voltage is tube current, the flow of electrons between the cathode and anode. It is proportional to the intensity of the emitted X-ray beam, but has no effect on the shape of the spectrum as a whole. [1, 2] A simplified schematic of an X-ray tube is shown in fig. 1.2.

The shape and size of the focal spot has an influence on the captured image, as well. Though it is often approximated as a point, a real focal spot's size is finite. In some cases, this may cause blurring or other disturbances to the homogeneity in images. [2]

Detection of radiation may be accomplished in various ways. One common approach is to place a layer of scintillating material directly in front of a photosensitive detector. The scintillator converts high-energy ionizing radiation into visible light, which is then detected. [2] Modern CT scanners usually utilize a two-dimensional detector array, but one-dimensional linear arrays and, in some cases, single detector elements may also be used. [1] Typical detectors commonly rely on *charge-coupled device* (CCD), complementary metal–oxide–semiconductor, or Flat panel technology to convert light into an electrical signal. The first two types can only be used to detect visible light, so a scintillator is necessary when detecting X-rays. Flat panels, on the other hand, can detect high-energy X-ray photons directly in some cases. [1]

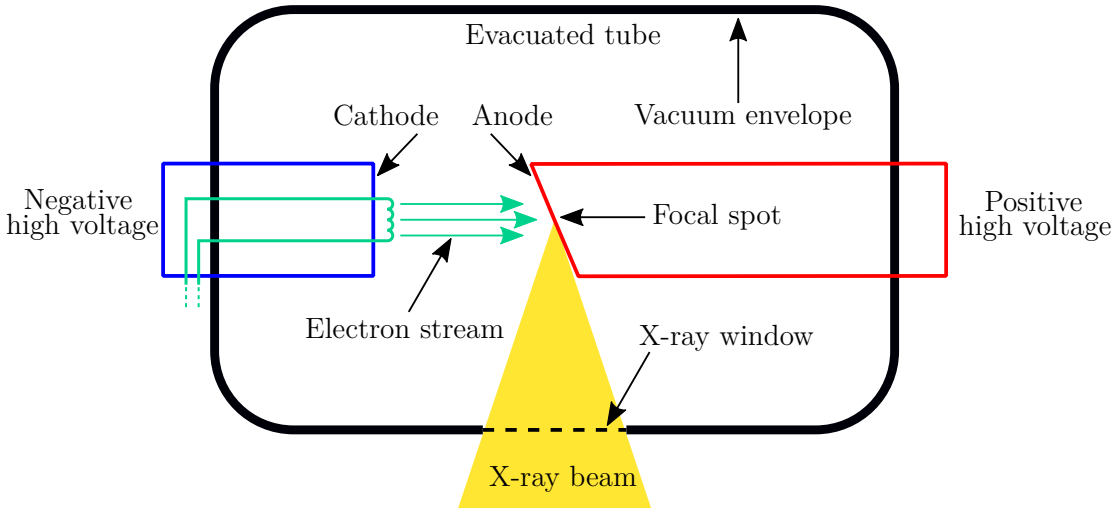

Fig. 1.2: A simplified schematic of an X-ray tube. Adapted from: [1].

The basic components of modern CT hardware can be arranged in one of several distinct geometries, each with its advantages and drawbacks. The most common are the parallel-beam, fan-beam, and cone-beam geometries, shown in fig. 1.3. [1]

In the parallel-beam CT geometry, all X-ray beams that form one projection are parallel to one another. One way to achieve this is to collimate the ray into a thin beam and have a single detector element detect this so-called pencil beam on the other side of the sample. This yields a single measurement, so linear movement of the source-detector pair is necessary to form a single 1-D projection. [1]

Fan-beam geometries use a thin fan of X-rays and a 1-D detector array to produce one-dimensional projections. The beam is generated by a small, ideally point-like source. If the beam is wide enough to illuminate the entire width of the scanned sample, there is no need for translation. This means there is no need to translate the source-detector pair, and the only movement is rotational, shortening scan times. [1] The detector array is most commonly arranged in one of two ways: A circular arc with its center at the X-ray source, or a linear arrangement of detector elements. In the first case, the angular step between beams hitting neighboring detector pixels is constant, whereas in the second, pixels are spaced out equally along a line, and angles between neighboring rays do not stay constant. [11]

Regarding this work, the *cone-beam computed tomography* (CBCT) geometry is most relevant. It can be described as an extension of the fan-beam geometry. A CBCT scanner uses a large two-dimensional planar detector, so a 2-D image of the entire sample, akin to a planar radiograph, is acquired instead of a thin 1-D projection. [1, 2]

There is a number of trajectories the source-detector pair can travel along when acquiring projections suitable for tomographic reconstruction. Perhaps the most

common is a circular trajectory, where the source stays in a single plane throughout the measurement. Other cone-beam scan geometries may involve additional vertical movement or tilt of the sample, and so on. [1]

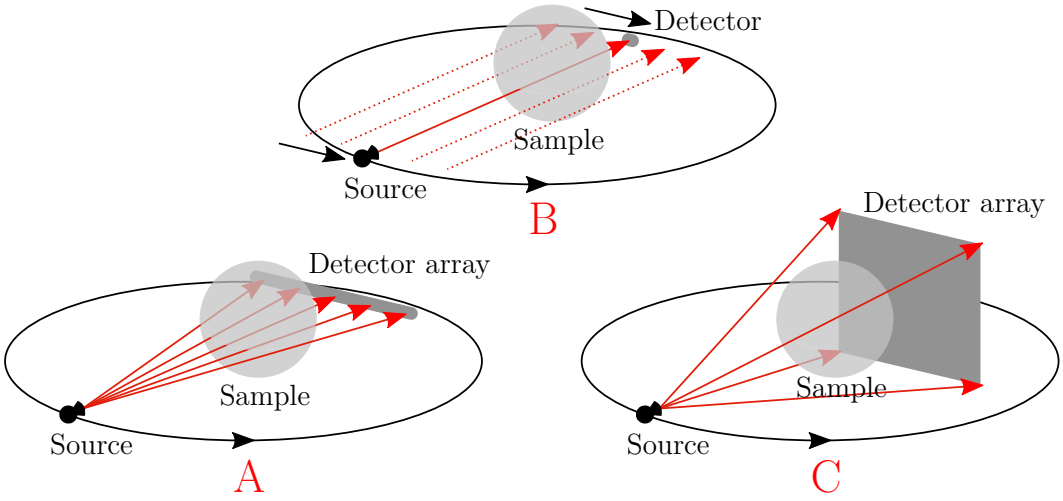

Fig. 1.3: Illustrative examples of typical CT geometries: the parallel-beam geometry (A), fan-beam geometry (B), and cone-beam geometry (C).

1.3 High-resolution CT

The term high-resolution CT refers to two different concepts, depending on whether the context is medical or not. Both are explained below, but in the scope of this work, only the non-medical one is relevant.

In the medical field, the term high-resolution CT refers to a technique, where a conventional medical scanner is used, but the acquisition parameters and reconstruction algorithms are altered to yield higher-resolution images. This approach is usually used to visualize the fine minutia of a patient's lungs. [17]

Outside of medical CT applications, the term is associated with specialized scanners that are specifically constructed to image small samples with high amounts of detail. [4] Other terms are also commonly used, such as micro-CT, nano-CT [4], or submicron CT [18], referring to the voxel resolutions reached. In some CT scanners, voxel resolutions can reach numbers as low as hundreds or even tens of nanometers. [4]

Such resolutions are commonly achieved in two ways. The first utilizes a small focal spot size and a detector with a relatively large pixel pitch – the distance between centers of two adjacent detector elements. [1] The sample is placed close

to the source, leading to substantial magnification of its projection on the detector due to the divergence of the cone beam.

Alternatively, samples may be placed very close to the detector and far from the source. This allows for a much larger source spot size, which leads to higher X-ray flux and better stability of CT measurements. [18] This approach utilizes detectors with a smaller pixel pitch [18, 19] and magnification of the image using optical elements inside the detector unit itself. In some cases, specialized X-ray optics are used [18, 19]; in others, X-rays are first converted to visible light by a scintillator, and then magnified using conventional microscope optics. [20]

2 Tomographic Reconstruction Methods

An object is a function of some parameter in space. Projections of the object are sets of line integrals, integrated values of the object function along straight lines. These line integrals, commonly referred to as rays, are acquired using some sort of energy which traverses the object function and interacts with its values. Alternatively, it is also possible to apply tomographic reconstruction techniques on projections of energy emitted from the object, which is common in fields such as nuclear medicine. [1, 2] This work focuses on transmission X-ray CT, where projections are acquired using X-rays and the object is a function of μ, as mentioned in chapter 1. The resulting cross-sectional image then displays the distribution of μ throughout the object. [11] The principles of CT are not restricted to only this case, however. [11]

2.1 Projections, Radon Transform, and the Sinogram

Let us consider a two-dimensional object function $f(x,\ y)$, a single thin slice of a sample, centered at the origin of a Cartesian coordinate system. In such case, a line integral may be parameterized by the two spatial variables $(x,\ y)$, but it is more convenient to express it in terms of $(\theta,\ t)$, where θ is the line's angle relative to the x axis and

$$t = x\cos(\theta) + y\sin(\theta). \tag{2.1}$$

In other words, t is the distance between the current ray and the central ray, which goes through the *axis of rotation* (AoR) located at the origin of the coordinate system. Using this notation, a line integral may be expressed as

$$P(\theta,\ t) = \int_{-\infty}^{\infty}\int_{-\infty}^{\infty} f(x,\ y)\delta(x\cos(\theta) + y\sin(\theta) - t)\,dx\,dy, \tag{2.2}$$

where δ is a one-dimensional delta function:

$$\delta(t) = \begin{cases} \infty & \text{if } t = 0 \\ 0 & \text{if } t \neq 0, \end{cases} \tag{2.3}$$

$$\int_{-\infty}^{\infty} \delta(t)\,dt = 1. \tag{2.4}$$

All values along a line given by (θ, t) are selected by the delta function and integrated to form a single value of P. [2, 11]

This integral transform of $f(x,\ y)$ to $P(\theta,\ t)$ is called the *Radon transform* (RT). To make the notation less cumbersome, it is useful to introduce the coordinate

system $(t,\ s)$, which is rotated counter-clockwise by the angle θ relative to $(x,\ y)$. [2, 11] This leads to

$$P(\theta,\ t) = \int_{-\infty}^{\infty} f(t,\ s)\, ds. \tag{2.5}$$

While both θ and t are continuous variables, in practice they have to be discretized to allow for the processing of P on a computer. [11] This becomes relevant later in the text, as discretized values need to be treated differently from the ideal continuous ones.

With a definition of the RT in place, it is now possible to define projections as sets of line integrals. There are several common ways to form projections from line integrals, each slightly different in practicality and ease of implementation. [11] Three of them – parallel-beam, fan-beam, and cone-beam projections, were already discussed from a more practical point of view in section 1.2. Here, they are described in a more abstract, mathematical sense.

In the simplest case, a projection is a set of $P(\theta_0, t)$, where θ_0 is a constant. It is a set of parallel line integrals, a parallel-beam projection (fig. 2.1). [11] Mathematically, these are very convenient, because they allow for a straightforward inversion of the RT to recover the original object function, as shown later.

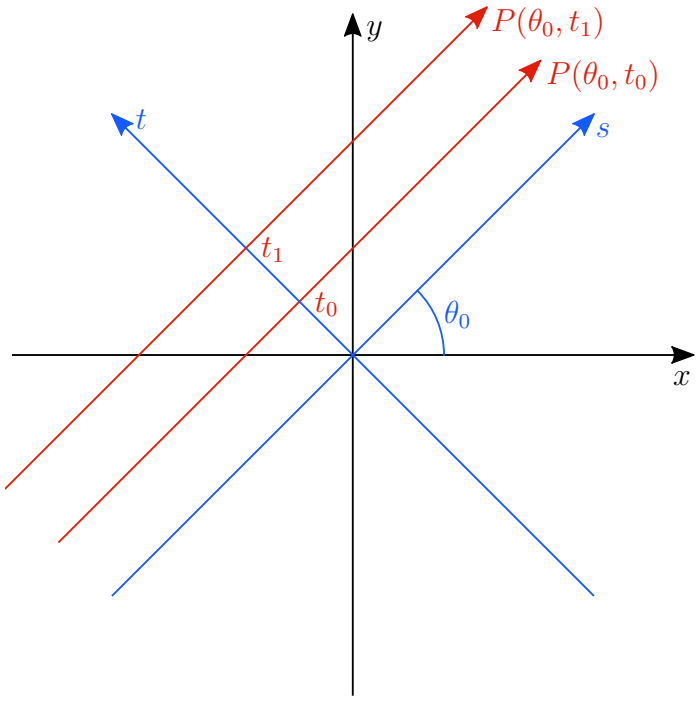

Fig. 2.1: A top-down schematic of a parallel-beam geometry. The reference Cartesian coordinate system is shown in black. A system rotated from the reference by the angle θ_0 is in blue. Rays are marked in red.

In practice, fan-beam projections are more convenient in terms of acquisition speed. Their rays originate from a point source and spread outward in the shape of a fan, making their mathematical description slightly more involved. When sampling is taken into account (meaning only a finite number of ray integrals is measured at discrete points), fan-beam projections can be further divided into two types: equiangular and equispaced. [11] The following description applies to the second type in particular, as it is more relevant to this thesis. There are only minor differences between both projection types, though, as explained by Kak and Slaney. [11]

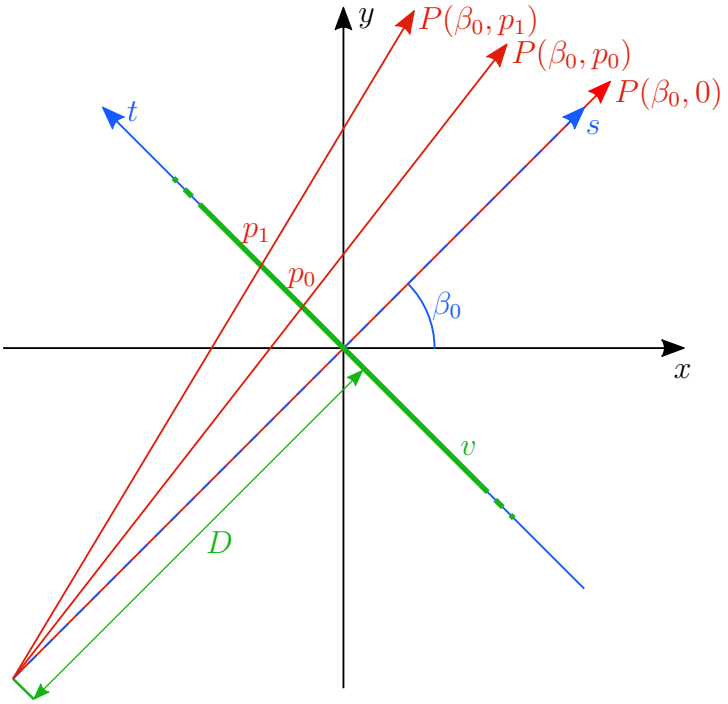

Fig. 2.2: A top-down schematic view of the fan-beam geometry. The detector line v is shown in green.

Note that since rays originate in a single point, the distance of this point from the origin, D, plays a key role. In a real setup, the detector is placed at a distance from the sample, but to describe the projections mathematically, it is advantageous to instead use a virtual detector parallel to the real one, which contains the origin. The latter is a scaled-down but otherwise equivalent version of the former. [11]

Since the rays in one fan-beam projection are not parallel to one another, it makes sense to express them in terms more convenient than (θ, t). A fan-beam projection can thus be expressed as $P(\beta, p)$. The first term, β, is the angle between the projection's central ray and the x axis. The second term, p, is the distance between the origin and the point on the virtual detector line v where a particular ray and v intersect. Refer to fig. 2.2 for an illustration of the geometry. The relationship

between $(\theta,\ t)$ and $(\beta,\ p)$ is

$$t = \frac{pD}{\sqrt{D^2 + p^2}} \tag{2.6}$$

$$\theta = \beta + \arctan\left(\frac{p}{D}\right). \tag{2.7}$$

Using the two equations above, fan-beam projections can be reshuffled, or rebinned, into parallel-beam ones. [1, 11]

The projections described above are 1-D projections of a 2-D object function. An intuitive extension to three-dimensional object functions in $(x,\ y,\ z)$ is to acquire multiple sets of 1-D projections at different values of z. This would be a very time-consuming process in practice, and a cone-beam geometry is far more suitable from this point of view. [11]

Before defining cone-beam projections, it is helpful to first describe line integrals in three dimensions. First, a new coordinate system (t, s, r) is created by rotating the $(x,\ y,\ z)$ coordinate system twice; by an angle θ around the z axis, forming $(t,\ s,\ z)$, and then by an angle γ around the t axis. [11] Using this coordinate system, a line integral is expressed as

$$P(\theta,\ \gamma,\ t,\ r) = \int_{-\infty}^{\infty} f(t,\ s,\ r)ds. \tag{2.8}$$

A cone-beam ray can then be expressed as $P(\beta,\ p,\ q)$. For a virtual detector plane w centered in the origin (as in the fan-beam case), a cone-beam projection is linked to eq. (2.8) by the following relations:

$$\theta = \beta + \arctan\left(\frac{p}{D}\right), \tag{2.9}$$

$$\gamma = \arctan\left(\frac{q}{D}\right), \tag{2.10}$$

$$t = \frac{pD}{\sqrt{D^2 + p^2}}, \tag{2.11}$$

$$r = \frac{qD}{\sqrt{D^2 + q^2}}. \tag{2.12}$$

In this notation, β refers to the same angle as it did in fan-beam projections. Instead of a 1-D detector line v, rays can now hit a 2-D plane w at a point $(p,\ q)$. [11] An illustration of the geometry is shown in fig. 2.3.

Note that for $p = 0$, the middle slice, a cone-beam dataset is equivalent to a fan-beam one. [11] Outside of this slice, however, this is not the case, as the fans are oblique and do not stay in one plane when β changes.

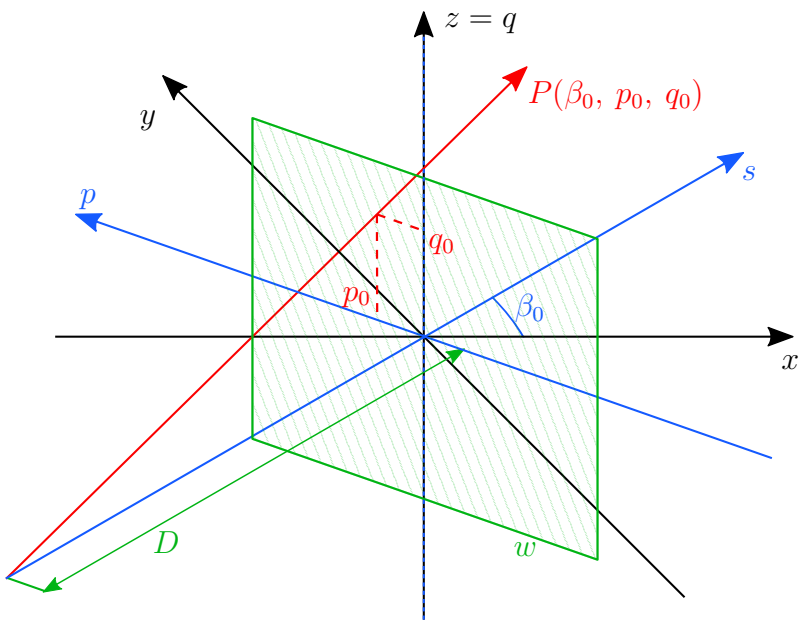

Fig. 2.3: A schematic illustration of the circular cone-beam geometry.

A set of parallel-beam or fan-beam projections for a range of θ (or β in the fan-beam case) may be visualized as a 2-D gray-scale image called a sinogram. Its name comes from the fact that the RT transforms a point in object space into a sine curve in Radon space, or a sine-like curve in the fan-beam case. [1, 21] An example of a parallel-beam sinogram for a synthetic test image is shown in fig. 2.4. Sinograms are a useful tool for visualizing certain properties of a given projection dataset, as well as for various forms of preprocessing before reconstruction. [1]

Tomographic reconstruction requires a set of angles acquired over a sufficient angular range. First, it should be noted that for circular orbits, the maximum reasonable range of a standard scan is 2π radians, a full circle. Anything more than that is redundant, as it will only result in an additional measurement of already acquired data. With this in mind, the minimal range required is often smaller than a full circle, and depends on the geometry used. [1]

For parallel-beam projections, a range of π radians is sufficient, since opposite projections are mirror images of each other, and hold the same information [11]:

$$P(\theta,\ t) = P(\theta + \pi,\ -t). \tag{2.13}$$

For fan-beam projections, a scan over the full 2π angular range, referred to as a full scan, is common. [1, 11] There exists a data sufficiency condition, however, which states that every line intersecting the object function must contain the fan's source point. [22] As a consequence, the minimal range for fan-beam projections is shorter

– π plus twice the fan angle (the angle between the central ray and a ray on the fan's edge). [1] Such a shortened scan protocol is referred to as a short scan. [11]

For cone-beam projections, a similar data sufficiency condition was formulated. [22, 23] Named Tuy's condition, it states that every plane intersecting the object function must contain the beam's source point. This condition is not satisfied in the circular cone-beam orbit, as the midplane contains the entire source trajectory, and any other plane parallel to it does not contain a single position of the source. [1, 22] As a result, slices of a reconstructed cone-beam dataset outside the midplane will always have missing data. The further from the midplane a slice is, the more information is missing. To rectify this, a more complicated scan trajectory may be used. [1, 22] In practice, when cone angles are small, errors are minor, and are therefore neglected. [22] In terms of angular range, the value π plus twice the fan angle is used, similar to the fan-beam case. [1]

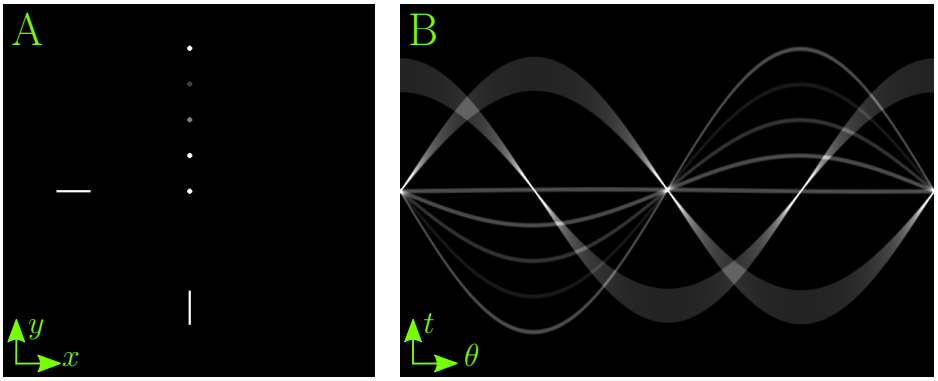

Fig. 2.4: A test image (A), containing several shapes of varying intensity levels at different distances from the center. Its sinogram (B) is shown with θ as the horizontal axis and t the vertical. The range of θ is $\langle 0,\ 2\pi)$, while the range of t was chosen so that the image's support is fully contained in all projections. Contrast of the sinogram has been enhanced.

2.2 Analytic Image Reconstruction

The geometry of three common types of projections was described in section 2.1. Additionally, requirements in terms of the angular range of data were discussed. With these foundations in place, the reconstruction process can be discussed.

Reconstruction algorithms are typically divided into two groups: analytic and iterative. Analytic algorithms are discussed first, as they are an established standard in CT. These methods are based on Fourier analysis. They assume that projection data are continuous and noiseless, and that they were acquired using a well-defined scan geometry, usually one described in section 2.1. [3] This somewhat limits the effectiveness of these algorithms, but they still remain useful, mainly because their implementations are fairly computationally inexpensive. [3] Noise is reduced by various methods outside the reconstruction algorithm itself, reducing its impact on reconstructions. Since real data is discrete, analytic methods are not directly applicable; fortunately, their discrete approximations exist. [2, 3]

2.2.1 Fourier Slice Theorem

Analytic reconstruction algorithms are based on the Fourier slice theorem, which relates a two-dimensional object function's RT with its *Fourier transform* (FT). [2, 3, 11] The FT is an integral transform. For an input function f, the FT returns its frequency spectrum F, a generally complex-valued function. This spectrum contains information on the amplitudes and phase shifts of sine curves with various frequencies, whose superposition forms the original function. The FT can be inverted to transform F back into f, and it can be generalized for higher dimensions. While the original definition of FT is applicable to continuous functions, there are other variants of it that can be applied to discrete signals. [2, 11]

The object's 2-D FT is defined as

$$F_f(u,\, v) = \int_{-\infty}^{\infty}\int_{-\infty}^{\infty} f(x,\, y)e^{-i2\pi(ux+vy)}dx\, dy, \tag{2.14}$$

where u and v are spatial frequencies along the x and y axes, respectively. The 1-D FT of an object's projection at angle θ_0 is

$$F_P(\omega) = \int_{-\infty}^{\infty} P(\theta_0,\, t)e^{-i2\pi\omega t}dt, \tag{2.15}$$

with ω denoting the spatial frequency along t. Taking eq. (2.5) into account, eq. (2.15) may be rewritten as

$$F_P(\omega) = \int_{-\infty}^{\infty}\int_{-\infty}^{\infty} f(t,\, s)e^{-i2\pi\omega t}ds\, dt. \tag{2.16}$$

Rewriting eq. (2.16) from the rotated (t, s) coordinate system to (x, y) using eq. (2.1) yields

$$F_P(\omega) = \int_{-\infty}^{\infty} \int_{-\infty}^{\infty} f(x,\ y) e^{-i2\pi\omega(x\cos(\theta_0)+y\sin(\theta_0))} dx\ dy. \tag{2.17}$$

When comparing eq. (2.17) with eq. (2.14), it is evident that the 1-D FT of a projection at θ_0 is equivalent to a slice of the object's 2-D FT going through the origin at angle θ_0 with the x axis. This relationship is what the Fourier slice theorem refers to, and it is central to analytical reconstruction algorithms. [11]

As a consequence of the Fourier slice theorem, it is possible to reconstruct the original object function by acquiring a sufficient range of parallel-beam projections, transforming them to the Fourier domain, inserting them into a 2-D spectrum at their corresponding angles, and applying the inverse 2-D FT. [11] This method of reconstructing the original object function is called direct Fourier reconstruction. [3]

If the reconstructed data were noiseless and continuous, this method would yield exact reconstructions of the analyzed object. In practice, however, only a finite set of discrete projections is available. To apply FT on discrete data, a *Fast Fourier transform* (FFT) algorithm is typically used, which requires the samples to be arranged in a Cartesian grid. This is not the case here, since the 1-D spectra of projections are inserted into the object's spectrum at their respective angles. In other words, The object's spectrum is sampled in polar coordinates. [3, 11]

A resampling step is necessary to apply the 2-D inverse FFT, and because the polar samples do not align with the Cartesian grid, interpolation has to be performed. [3, 11] Unfortunately, interpolation in the frequency domain causes considerable artifacts in the reconstructed image, discrepancies between reconstructed images and the actual object. These artifacts become even more severe for higher-frequency components, which are sampled more sparsely due to being farther from the origin. [11] The difference between a polar set of samples and a Cartesian grid is shown in fig. 2.5.

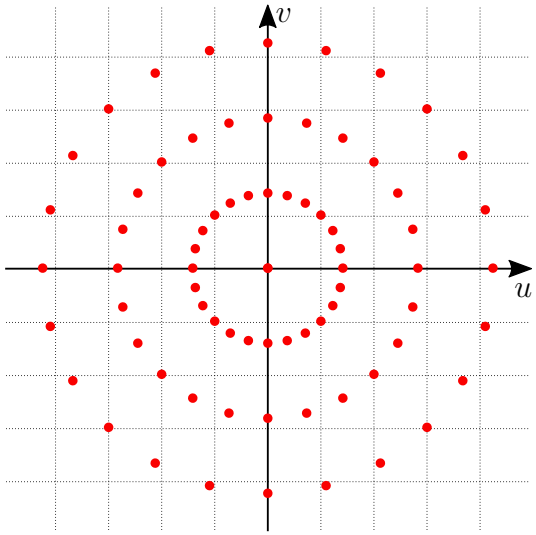

Fig. 2.5: A two-dimensional frequency spectrum with Cartesian components u and v. Polar samples are shown in red, illustrating their misalignment with a Cartesian grid, as well as the uneven sampling of different frequencies – higher-frequency components are sampled more sparsely.

2.2.2 Filtered Backprojection

Based on the Fourier slice theorem, the *filtered backprojection* (FBP) algorithm is in principle very close to direct Fourier reconstruction, but several key differences make it the preferable reconstruction method for practical applications. [11]

The inverse FT of the spectrum of an object function is

$$f(x,\ y) = \int_{-\infty}^{\infty}\int_{-\infty}^{\infty} F(u,\ v)e^{i2\pi(ux+vy)}du\ dv. \tag{2.18}$$

The integrand $F(u, v)$ can be rewritten in polar form $F(\omega, \theta)$ by making the following substitutions:

$$u = \omega\cos(\theta), \tag{2.19}$$

$$v = \omega\sin(\theta). \tag{2.20}$$

Then, the differential can be rewritten as

$$du\ dv = \omega\ d\omega\ d\theta, \tag{2.21}$$

where ω is the determinant of the Jacobian for the given change of variables. [11] After appropriately changing the limits of both integrals, this leads to

$$f(x,\ y) = \int_{0}^{2\pi}\int_{0}^{\infty} F(\omega,\ \theta)e^{i2\pi\omega(x\cos(\theta)+y\sin(\theta))}\omega\ d\omega\ d\theta. \tag{2.22}$$

Since two opposite parallel-beam projections are mirror images of each other, the following holds true for their spectra:

$$F_P(\omega, \theta) = F_P(-\omega, \theta + \pi). \tag{2.23}$$

Due to this relation, eq. (2.22) is equivalent to

$$f(x,\ y) = \int_0^{\pi} \int_{-\infty}^{\infty} F(\omega,\ \theta) e^{i2\pi\omega(x\cos(\theta)+y\sin(\theta))}\ |\omega|\ d\omega\ d\theta. \tag{2.24}$$

This is why, as mentioned at the end of section 2.1, a range of π radians is sufficient for parallel-beam CT reconstruction. Note that in eq. (2.24), the term ω now appears in its absolute value. [11]

It is helpful to rewrite eq. (2.24) as

$$f(x,\ y) = \int_0^{\pi} Q(\theta,\ t)\ d\theta, \tag{2.25}$$

where

$$Q(\theta,\ t) = \int_{-\infty}^{\infty} F_P(\omega,\ \theta) e^{i2\pi\omega t}\ |\omega|\ d\omega \tag{2.26}$$

and t is $x\cos(\theta) + y\sin(\theta)$, as defined in eq. (2.1). Equations 2.25 and 2.26 are the basis of the FBP algorithm. [11]

Equation (2.25) corresponds to the backprojection step of FBP, where projections $Q(\theta,\ t)$ are projected back into image space. This may not be immediately obvious, but a single value $Q(\theta_0,\ t_0)$ is inserted into object space along a line with distance t_0 from the origin and angle θ_0 relative to the x axis. This is the same line along which the value $P(\theta,\ t)$ was acquired. The final reconstruction is then a superposition of all such backprojected values. [11]

Setting $Q(\theta,\ t) = P(\theta,\ t$ in eq. (2.25) corresponds to a simple backprojection of the original, unaltered set of projections. This leads to a reconstruction that is heavily blurred. In mathematical terms, it is $f(x,\ y)$ convolved with a $\frac{1}{t}$ point-spread function (recall that according to eq. (2.1), t is the distance from origin). Such a reconstruction is not useful for further analysis; it is dominated by low spatial frequencies, which dampen details of the image. [2, 3]

Equation (2.26) compensates for the point-spread function of backprojection. It is a filtering operation performed in the Fourier domain on projection $P(\theta,\ t)$. Here, $|\omega|$ corresponds to the filter's frequency response. The resulting $Q(\theta,\ t)$ is referred to as a filtered projection. [11] The filter is commonly called a ramp filter, due to its frequency response being shaped like an inclined ramp. [3] For reference, see fig. 2.6.

For the sake of convenience, $|\omega|$ in eq. (2.26) may be substituted by a general symbol for a filter's frequency response, $H(\omega)$:

$$Q(\theta,\, t) = \int_{-\infty}^{\infty} F_P(\omega,\, \theta) e^{i2\pi\omega t} H(\omega)\, d\omega. \tag{2.27}$$

As an alternative, a filtered projection may also be expressed as a convolution of $P(\theta,\, t)$ with the impulse response of the filter $h(t)$, which is just the inverse FT of $H(\omega)$:

$$Q(\theta,\, t) = \int_{-\infty}^{\infty} P(\theta,\, t) h(t' - t)\, dt. \tag{2.28}$$

It was previously mentioned that analytic reconstruction algorithms, such as the one above, are derived for noiseless, continuous projection data. In reality, the available data are a set of noisy discrete samples incompatible with these methods. Fortunately, it is possible to formulate discrete approximations of these algorithms, which yield satisfactory results. [2]

Since discrete projections are intrinsically band-limited, the ramp filter also needs to have a zero response outside the signal's frequency range. The maximum frequency of a discrete signal is half of its sampling frequency f_s. Higher frequencies cannot be resolved and, when they are present in the original signal, they cause characteristic artifacts called aliasing in the sampled version. [2] Fortunately, in most cases, little energy is contained within these high frequencies, due to the limited spatial resolution of real imaging systems. The contribution of these high-frequency components to the object function is thus negligible. [2, 11]

A band-limited ramp filter, or Ram-Lak filter, is in principle a frequency-domain multiplication of $|\omega|$ and a rectangular window of unit height and a width corresponding to the projections' frequency bandwidth. [2, 3] Noise can be suppressed as part of this filtering step, too. A large portion of the noise spectrum's energy is contained in high-frequency components, the very same ones that are amplified the most by the Ram-Lak filter. This noise can be partially suppressed by multiplying the Ram-Lak filter's frequency response by an additional apodizing function, which gradually tapers off to low or zero values. A selection of commonly used apodized filters is shown in fig. 2.6. Naturally, such an apodized filter also dampens high frequencies of the object function, reducing spatial resolution. In practice, this drawback is outweighed by the increase in signal-to-noise ratio. [2]

Digital filtration requires some additional considerations. While the filter's response at $\omega = 0$ is zero in the continuous case, it is beneficial to set it to a small non-zero value in the discrete form to avoid undesirable changes in the intensity values of projections. [2, 24]

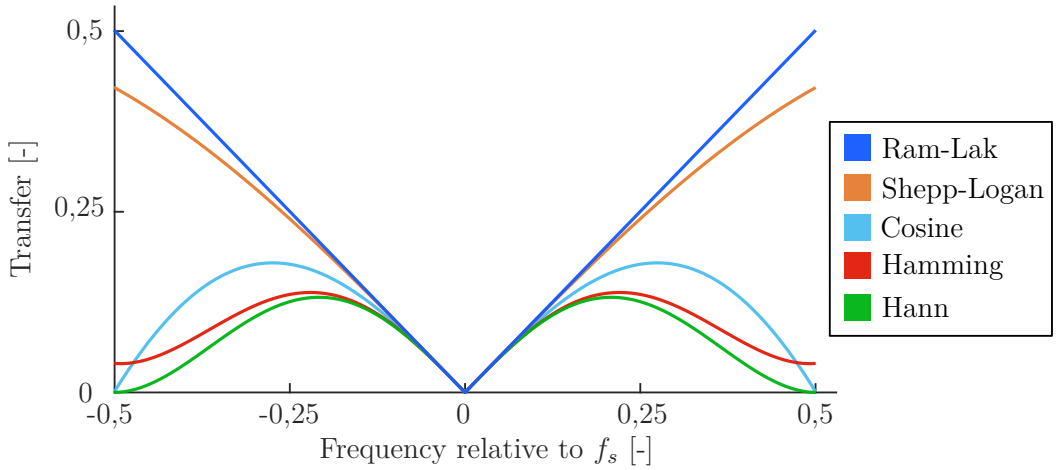

Fig. 2.6: Frequency responses of selected commonly used FBP filters.

Moreover, filtration by multiplication in the frequency domain is equivalent to circular convolution of the projection with a filter kernel in the spatial domain. This stems from a fundamental property of the FT; when the signal spectrum is discrete, the signal is periodic, and vice versa. Circular convolution can then lead to undesirable results due to neighboring periods of the signal and filter kernel contributing to the result. The solution is to simply pad both the signal and the filter in the spatial domain by a number of zeros large enough to effectively create a buffer zone between neighboring periods. [2, 24] As a side-note, while it is possible to filter projections in the spatial domain, frequency-domain filtration is generally quicker and thus more advantageous. [2, 24]

The integral form of the backprojection step in eq. (2.25) may then be approximated by a sum over all projections acquired across the necessary angular range. Since each projection has a finite number of samples, its backprojection will generally not align with the Cartesian pixel grid. Interpolation of backprojected values is necessary. This is similar to the issue encountered in direct Fourier reconstruction and illustrated in fig. 2.5. Fortunately, interpolation in the spatial domain causes far fewer artifacts than in the frequency domain. [11]

2.2.3 Fan-Beam and cone-beam reconstruction

While FBP and its discrete approximation are viable for parallel-beam projections, fan-beam projections require a slightly different approach. There are two common ways to tackle this problem. The first one has already been mentioned in section 2.1, albeit very briefly. Using eq. (2.6) and eq. (2.7), one can rebin every ray of a fan-beam dataset to a ray in a parallel-projection geometry. [2, 11] This rebinning operation is not computationally demanding, so it can be performed quite rapidly. Once

projections have been rebinned, FBP can be employed to reconstruct them. These rebinned rays are not spaced out equally, however, so one has to apply interpolation to obtain equispaced data. This is a potential source of errors. [2, 11]

The second approach modifies the FBP formula to accommodate fan-beam projections, creating the so-called weighted backprojection algorithm. The weighting scheme used depends on how projections were sampled. [11] Once again, only the equispaced case will be discussed, and a formula to reconstruct from such projections will be presented without derivation.

It is simpler to consider a full parallel-beam circular scan first. in this case, the FBP equation 2.25 may be modified to

$$f(r,\ \phi) = \frac{1}{2}\int_0^{2\pi}\int_{-\infty}^{\infty} P(\theta,\ t)h(t'-t)\ dt\ d\theta, \tag{2.29}$$

where $Q(\theta,\ t)$ was expressed according to eq. (2.28) and polar coordinates $(r,\ \phi)$ are used.

In general, two main modifications need to be made to perform reconstruction of fan-beam projections. The first is to weigh each ray by the cosine of the angle between it and the projection's central ray. The second is in the backprojection step, where the values are weighted by

$$U(r, \phi, \beta) = \frac{D + r\sin(\beta - \phi)}{D}. \tag{2.30}$$

The constant $\frac{1}{2}$ is often moved to $h(t)$, forming $g(t) = \frac{h(t)}{2}$. These modifications yield the weighted backprojection formula

$$f(r,\ \phi) = \int_0^{2\pi} \frac{1}{U^2(r, \phi, \beta)} \int_{-\infty}^{\infty} P(\theta,\ t)\frac{D}{\sqrt{D^2 + t^2}} g(t'-t)\ dt\ d\theta. \tag{2.31}$$

Once again, an approximation of this expression can be formulated for non-ideal discrete data, making it possible to implement the weighted backprojection algorithm on computer. [11]

Reconstruction of three-dimensional data presents additional challenges when compared to its 2-D counterpart. While the RT can be generalized to higher dimensions and a Fourier slice theorem has been formulated for 3-D data, neither of these have seen widespread practical use. Instead, different algorithms have been developed that are suited specifically for the popular cone-beam geometry. [22]

Among the most widespread is the *Feldkamp-Davis-Kress* (FDK) algorithm, which is specifically made for the circular trajectory. [25] As noted before, Tuy's condition is not satisfied for the circular orbit, so FDK cannot provide theoretically exact reconstructions. Errors caused by data incompleteness include an erroneous

decrease of attenuation values in planes away from the central slice, cross-talk between slices, and others. These cone-beam artifacts depend on the cone angle, and for a reasonably small angle, they are not significant. Coupled with the algorithm's robustness and ease of implementation, and the practicality of the circular orbit, this makes FDK a very popular choice. [22]

The FDK algorithm is in fact an extension of the fan-beam weighted backprojection algorithm into three dimensions. First, cone-beam projections are weighted by the cosine of the angle between the given ray and the central ray. Next, a 1-D ramp filter is applied to each row of each projection separately. Finally, a weighted backprojection is performed. [22] In other words, each row of a cone-beam projection is treated as a fan-beam projection.

This also explains, in an intuitive sense, how the cone-beam artifacts mentioned earlier are formed. In the midplane, FDK is reduced to a 2-D fan-beam reconstruction, which is theoretically exact. [11] Outside of it, though, the fans are slanted at an angle relative to the central slice.

Other popular 3-D reconstruction schemes include Grangeat's and Katsevich's algorithms. These approach the problem of cone-beam reconstruction in different ways, allowing for more flexibility in terms of the scan orbit, and theoretically exact reconstructions if Tuy's condition is satisfied. [22] They are outside the scope of this work, however, and only the FDK algorithm is used.

2.3 Iterative Image Reconstruction

Section 2.2 introduced analytic reconstruction algorithms, which are based primarily on Fourier analysis. There exists another major group of reconstruction algorithms – the iterative methods, which use the principles of linear algebra. Unlike the analytic approach, which is formulated for continuous data and discretized after the fact, iterative methods take the discrete nature of real data into account from the very beginning. [2, 3, 11] In this section, the basic principles of iterative methods are shown for 2-D data for the sake of simplicity, but an extension to the third dimension is straightforward.

Before an iterative algorithm can be applied, a discrete, bounded model of the object function f must be formed. This model can be expressed as

$$f(x,y) = \sum_{k=1}^{K} \sum_{m=1}^{M} f_{k,m} g_{k,m}(x,y), \tag{2.32}$$

where $g_{k,m}(x,y)$ is a basis function which defines the spatial extent of sample $f_{k,m}$ in the object's discrete model. The most common form of $g_{k,m}(x,y)$ is a square pixel, although a smooth Kaiser-Bessel window (also known as a blob) is also popular. [2, 3]

Samples of the object are most commonly arranged in a regular grid, forming a 2-D matrix. When they are ordered into a 1-D vector $\vec{f} = [f_n]$, $n \in \{1, 2, \ldots, N\}$, where $N = K \times M$, then $\vec{f}$ can be thought of as a single point representing the object in an N-dimensional space. [11]

Next, a discrete model of the RT – or forward projection, is formed as follows:

$$p_m = \sum_{n=1}^{N} w_{m,n} f_n. \tag{2.33}$$

All N pixels of the object are weighted by a certain value and summed together to form a ray sum, an approximation of a ray integral. Equation (2.33) can be written in matrix form as

$$\vec{p} = \mathbf{W}\vec{f}, \tag{2.34}$$

where $\vec{p}$ is an M-dimensional vector of projection data and $\mathbf{W}$ is the system matrix, which contains weights $w_{m,n}$. The m-th row of $\mathbf{W}$ describes the contribution of all values of $\vec{f}$ to a single p_m, while the n-th row specifies how a single pixel f_n contributes to every value of $\vec{p}$. Obviously, since a ray traversing the object model interacts with only a small fraction of the total number of pixels, most weights will have a value of zero, making $\mathbf{W}$ sparse. [2, 3]

There are multiple ways how to determine the non-zero elements of $\mathbf{W}$. When rays are modeled as lines through the object, then the weight $w_{m,n}$ is the length of intersection of ray m with pixel n. [3] Another, somewhat more precise approximation of a ray is a stripe with finite width. In this case, $w_{m,n}$ is the intersection area of ray m and pixel n, relative to the pixel's total area. [2]

The system matrix $\mathbf{W}$ fully describes the scan geometry. It places no restraints on the shape of the scan orbit, position and tilt of the detector and other parameters of the scan, since every ray is modeled separately. This makes iterative methods extremely flexible and suitable for both traditional (e.g. circular cone-beam) and unconventional setups. [2]

Equation (2.34) is a system of linear equations. For the case where $n = m = 2$, it can be written out as

$$\begin{aligned} p_1 &= w_{1,1} f_1 + w_{1,2} f_2 \\ p_2 &= w_{2,1} f_1 + w_{2,2} f_2. \end{aligned}$$

The values p_m are known – they are the measured projection values. The goal of CT is to recover f_n; this task is referred to as an inverse problem. [26] For the example above, inverting the system of equations is easily done by constructing the inverse matrix $\mathbf{W}^{-1}$ (provided $\mathbf{W}$ is regular) and reformulating eq. (2.34) as

$$\mathbf{W}^{-1}\vec{p} = \vec{f}. \tag{2.35}$$

Several factors make eq. (2.35) unusable in practice. First, typical sizes of $\mathbf{W}$ are usually too large for the calculation of its inverse to be realistic, if at all possible. [2] Moreover, $\mathbf{W}$ is hardly ever a square matrix. Second, solving the system of equations for $\vec{f}$ is what is called an ill-posed problem.

In simple terms, if a problem has no solution, more than one solution, or is unstable, then it is ill-posed. Instability refers to small inaccuracies in measured data causing disproportionately large errors in the result. In the reconstruction process, instability and lack of a unique solution are caused by noise in the measurements, which is conveniently omitted form eq. (2.34), but is unavoidable in reality. [26]

Instead of using eq. (2.35) to reconstruct $\vec{f}$, an algebraic method can be employed to solve the problem in an iterative manner. Such an algorithm starts at an initial estimate $\vec{f_0}$, and ideally converge to a solution close to the true $\vec{f}$ in a reasonable amount of steps. [3]

One of the most well-known and oldest algebraic methods is the *algebraic reconstruction technique* (ART). In each iteration, ART updates the reconstruction by evaluating a single ray sum through the current image, comparing it to the original measured projection value, and adding a difference term to the image. In contrast to this, another popular method, the *simultaneous iterative recontruction technique* (SIRT), calculates the contributions of all rays first and only then updates the reconstruction by an average of all these values. While SIRT converges more slowly than ART, it tends to yield smoother, subjectively better-looking reconstructions. [11]

A compromise between ART and SIRT is the *simultaneous algebraic recontruction technique* (SART). Here, values of the image are updated after going through equations of all rays making up one projection. The SART algorithm is an example of using ordered subsets to speed up convergence while keeping reconstruction quality high. The idea of ordered subsets is updating the pixels of the image only after going through a certain subset of the linear equations representing ray sums. For SART, each subset contains one projection, but different subset sizes may also be chosen in other algorithms. [11, 27]

In addition to ART, SIRT, and SART, many other algorithms have been proposed. For instance, instead of adding an update term to the image, some techniques multiply the image's pixel values by a correction value in each iteration. [27] Even though algebraic methods are among the simplest iterative algorithms available, one can already incorporate some prior information into the reconstruction process. For example, a non-negativity constraint is commonly applied, where in each iteration, pixels with negative values are set to zero. This stems from the knowledge that the underlying physical parameter (μ cannot have negative values in the case of transmission X-ray CT). [11, 27]

The performance of algebraic algorithms is hampered in low-dose CT, where statistics of the acquisition process cause significant noise in measured data. In such cases, a statistical model may be applied to improve the result. The uncertainty in CT data comes from a range of sources, including photon counting statistics, electronic noise of the detector, conversion of X-rays to photons of visible light in the scintillator, and others. To account for all of these is nearly impossible, so a simpler model, often one based on a Poisson or Gaussian distribution, is usually used as an approximation. Such a statistical model can be incorporated into a weighted least squares cost function, which is then minimized. [3]

Nevertheless, even statistical weighting cannot ensure convergence of the reconstruction algorithm to a satisfactory result. In such case, one can introduce some prior knowledge about the object to make the solution adhere more closely to expectations. This is accomplished by adding a regularizer to the cost function, which typically smooths the result. The regularizer's contribution to the overall solution should be regulated to achieve a good compromise between spatial resolution and smoothness in the final image. A typical regularizer can be constructed as follows:

$$R(\vec{f}) = \sum_{m=1}^{M} \sum_{k \in \nu_m} \psi_{m,k}(f_m - f_k), \tag{2.36}$$

where ν_m is a set of indices for neighbors of sample f_m and $\psi_{m,k}$ is a function that determines the regularizer's smoothing strength and related characteristics. [3] Common examples of $\psi_{m,k}$ include a hyperbolic function, which tends to preserve edges while smoothing in more homogeneous areas, or the absolute value, which tends to yield piecewise-constant images. [3]

With a noise model and a regularizer in place, an algorithm must now be chosen to minimize the cost function. Once again, this calls for an iterative approach. Typical choices include coordinate descent methods, conjugate-gradient schemes, or algorithms based on maximum likelihood expectation maximization. Various other methods – as well as modifications of the ones mentioned – have been studied and applied with the intent to speed up convergence to a satisfactory solution. [3]

Iterative reconstruction methods have seen a lot of interest in recent years. This is due to their flexibility and ability to yield good results in cases where analytic methods fail, such as when projection data is heavily corrupted by noise. [3] One of the most intensely researched aspects in this area is the incorporation of state-of-the-art machine learning techniques into the reconstruction process.

In [28], a convolutional neural network is used to tune the strength of an iterative algorithm's regularization term on a pixel-by-pixel basis. During training, the network adjusts the strength of the regularization term in each iteration, and is then rewarded based on whether this change brought the reconstruction closer

to the ground truth according to an objective criterion. Researchers have also used deep neural networks to estimate an optimal prior object model in order to suppress noise in reconstructed images. A large dataset of images is used to train a denoising operator, which is then plugged into an iterative reconstruction scheme as the regularizing term. [29]

Other researchers focus on optimizing statistical algorithms in order to speed up their convergence. This is in effort to mitigate a major disadvantage of iterative methods: compared to analytic schemes, they are much more demanding in terms of the amount of processing power needed, and they take a fairly long time to converge to a satisfactory result. Works by Sridhar et al. [30] and Ha and Mueller [31], among others, attempt to tackle this issue by parallelizing the reconstruction algorithms and utilizing graphical processing units and multiple workstations. The authors aim to achieve fast convergence rates while not sacrificing the flexibility of iterative algorithms in terms of the scan geometry, statistical modeling, and other areas.

Widespread use of iterative reconstructions is still somewhat limited, due to their high hardware demands. However, with the rise of graphical processing units, the ability to efficiently parallelize computer programs, and more sophisticated hardware and software in general, iterative algorithms have become a realistic option for CT reconstruction. This has led to their re-emergence as a major and growing area of research in the field of *computed tomography* (CT) and inverse problems in general. Their advantages over analytic algorithms are significant, and include the ability to incorporate prior knowledge, flexibility in terms of scan geometry, or better performance for incomplete, noisy, and sparse projection data. [3, 27]

2.4 Determination of the position of the AoR

An important aspect of CT reconstruction is to correctly determine where the AoR projects onto the detector. This parameter must be known in order to perform accurate CT reconstruction, and errors result in so-called tuning-fork artifacts [1, 32, 33] or double edges [1]. It is common to calibrate the AoR prior to measurement, using a dedicated phantom and a corresponding alignment algorithm. [34] Even after calibration, however, the AoR may shift due to mechanical instability of the rotation stage or changes in the setup of the scanner. [33] It is therefore often necessary to perform additional checks of this parameter for every measured dataset.

Manual determination of the AoR can be done through visual assessment of reconstructions for different AoR estimates. This process can be time-consuming, however, so a number of automatic AoR determination algorithms has been proposed. These algorithms can be grouped into several categories, based on the general approach used. The first category is based on finding and aligning a fixed point

in projection data, the second exploits some form of symmetry in recorded datasets, and the third evaluates reconstructed images.

The first group of algorithms relies on detecting a reference point in all projections of a given dataset, and using this information to find the AoR. Azevedo et al. [35] use the center of mass as reference. Generally, the center of mass of the sample copies a sinusoidal path in parallel-beam projection data. A sine function is thus fit on this path, and its parameters are used to determine the AoR. The authors of [35] also described a related method to find the AoR in full-scan fan-beam data by averaging the center of mass for all projections of a scan. In [36], Jun and Yoon use an approach based on finding the center of attenuation in projections. This is a similar concept to the center of mass, but it is based on values of the sample's linear attenuation coefficient. Once the center of attenuation is determined in all projections, it is aligned and used as a virtual AoR. Approaches that fall into this category often require non-truncated data, which is not always possible to ensure, particularly in some scan geometries described later in this work.

Approaches in the second category are based on the symmetry of projection data acquired along a circular trajectory. In parallel-beam CT, opposite projections are ideally mirror images of one another. The AoR may thus be found by registering two projections measured 180 degrees apart, with one of them flipped horizontally. Such an approach was explored by Yang et al. [37]. Registration is done by detecting significant features in both projections and matching corresponding features. This way, orientation vectors are acquired and used to calculate the most probable shift between both projections, and thus the position of the AoR. [37]

Vo et al. [38] use properties of the sinogram in Fourier space to find the AoR. They extend a parallel-beam sinogram from a π range to a 2π one by duplicating it and flipping it about an estimated AoR. Components of the frequency spectrum of such an extended sinogram are constrained to a double-wedge region, the width of which is given by the scanned object's extent in the scanned FoV. If the AoR is misplaced, the spectrum contains components outside this region. Therefore, finding such an AoR position, where these erroneous components are minimized, results in determination of the correct AoR. [38]

While intuitive, these approaches can not generally be applied to fan-beam or CBCT, where opposite projections are not mirror images of each other due to varying magnification throughout the scanned volume. [39] Min et al. [39] adapt the idea of projection symmetry to find the AoR of a full-scan fan-beam sinogram. The sinogram is rebinned to parallel-beam and divided into two equal parts. Then, one of these parts is flipped to correspond with the second one, and each of its rows is registered using cross-correlation. The resulting positions of cross-correlation peaks are then averaged, resulting in an estimate of the AoR shift.

Lin et al. [32] proposed a method for finding the AoR in CT data with a displaced sample. Symmetric features of a fan-beam sinogram scanned over an angular range of 2π are exploited in this approach. By aggregating information from all projections into two one-dimensional vectors for the left and right side of the sinogram, this method becomes suitable for fan-beam data. The two vectors are then compared at different AoR positions to find such a location, where they are most similar.

Finally, a number of methods evaluate reconstructions using some objective metric sensitive to artifacts formed due to AoR shifts. Donath et al. [33] suggest several such metrics. In the discrete case, they are based on the sum of the absolute value of pixels in an image, the number of its negative pixels, and the entropy of its histogram. The value of any of these three is optimized as a function of the position of the AoR, yielding the best estimate of the argument.

Cheng et al. [40] evaluate tomograms based on their total variation, which quantifies the total magnitude of differences between neighboring elements of the image. Since AoR errors cause streak-like artifacts or double edges, they are assumed to increase the total variation value of a reconstruction. The metric is thus minimized to find the optimal AoR position.

Yang et al. [41] opted for training a convolutional neural network to estimate the correct AoR position. Their method shows great accuracy and good robustness to noise. In order to perform well, the algorithm requires training on a solid database of images, and its performance may be diminished if it is applied on samples that do not resemble the training data. [32] In general, algorithms that fall into this category can be applied to any dataset regardless of geometry, as they do not operate on projection data, but on the cross-sectional images themselves. The main disadvantage of these methods is the increased amount of computation required when compared to the other categories mentioned, and therefore a higher time-cost. [32]

2.4.1 AoR estimation methods suitable for FoV extension techniques

The overview of AoR estimation methods in this chapter is not exhaustive, as this is an active area of research, and the possible approaches are numerous. A vast majority of algorithms fall into one of the three mentioned categories, however. In terms of this work, the sinogram symmetry approach of Lin et al. [32] and the reconstruction evaluation algorithms of Donath et al. [33] and Cheng et al. [40] are the most attractive. All three of these are suitable for the particular scanner geometry and scan protocol used here for FoV extension. Therefore, these methods are further described in more detail.

Estimating AoR Position Using Sinogram Symmetry

The AoR estimation method described by Lin et al. [32] is based on the symmetric property of a fan-beam sinogram:

$$\int_{-p'}^{p_0}\int_{0}^{2\pi} P(\beta,\ p)d\beta\ dp - \int_{p_0}^{p'}\int_{0}^{2\pi} P(\beta,\ p)d\beta\ dp = 0. \tag{2.37}$$

Here, p' is an arbitrary value of p, assuming that p_0, the location of the AoR projection, is equal to zero. For a real sinogram, p' is limited by the detector array's finite size. This is the foundation for AoR estimation, which consists of finding a position of p_0 that ideally satisfies the equation. [32]

Equation (2.37) is valid only if the ray going through the AoR is orthogonal to the detector plane. When this is not the case, projections need to be transformed from the real detector onto a virtual one, where this assumption holds true. This transform is described in section 4.2.3, and must be re-evaluated every time the position of p_0 is changed. [32]

The measured projection data is discrete – values are known only at a finite number of detector bins. On one side of p_0, values at real detector bins can be taken, and no further processing is required. These real values can be denoted D_i, $i \in \{1, 2, \cdots, N\}$, with corresponding values V_i at the virtual detector. Interpolation between measured values is necessary to ensure the other side is evaluated at points V_i', which are the same distance from p_0 as the corresponding V_i. [32] Once all V_i and V_i' are known for all projection angles β_j, eq. (2.37) needs to be rewritten for discrete data:

$$\sum_{i=1}^{N}\sum_{j=1}^{M} P(\beta_j,\ V_i) - \sum_{i=1}^{N}\sum_{j=1}^{M} P(\beta_j,\ V_i') = 0, \tag{2.38}$$

where M is the total number of projections.

The final consideration one has to make is that for real data, eq. (2.38) is not satisfied due to noise, measurement errors, a non-uniform response of detector elements, and other factors. One can overcome this by forming an objective function that evaluates the difference between values on both sides of p_0. Then, an optimal p_0 can be found by minimizing this function.

Estimating AoR Position by Evaluating Tomograms

Both Donath et al. [33] and Cheng et al. [40] employ methods based on reconstruction evaluation, and their approaches are similar. Although both works are originally developed for parallel-beam CT, operating on reconstructions should theoretically make them independent of the acquisition geometry, which makes it possible to adapt them for fan-beam or cone-beam setups.

Donath et al. [33] suggest three separate reconstruction quality metrics. The first of these is the integral, or sum in the discrete case, of absolute values in the reconstruction:

$$Q_1(\tilde{f}) = \frac{1}{m_0} \sum_{i=1}^{X} \sum_{j=1}^{Y} \left| \tilde{f}(i,\ j) \right|. \tag{2.39}$$

Here, $\tilde{f}$ is a reconstructed image for the current AoR estimate, X and Y are the number of rows and columns of the reconstruction voxel grid, and m_0 is the mean projection weight calculated as the mean sum of values in each projection. Q_1 is at its minimum for the correct AoR position. [33]

The second is the integral, or sum, of negativity:

$$Q_2(\tilde{f}) = -\frac{1}{m_0} \sum_{i=1}^{X} \sum_{j=1}^{Y} u(-\tilde{f}(i,\ j))\tilde{f}(i,\ j), \tag{2.40}$$

where u is the Heaviside step function:

$$u(\alpha) = \begin{cases} 1, \alpha \geq 0 \\ 0, \alpha < 0 \end{cases} \tag{2.41}$$

As f is assumed to be a non-negative function, Q_2 will be minimized by finding the right AoR position. [33]

Finally, the third proposed metric is the entropy of the reconstruction's histogram. Artifacts caused by AoR errors introduce additional structures, which are assumed to spread out the histogram of gray values of the image This can be quantified by the histogram's entropy, which, for a discrete grayscale image, is

$$H(\tilde{f}) = -\sum_{g=0}^{G} p_g \log_2(p_g), \tag{2.42}$$

where p_g is the fraction of pixels in image $\tilde{f}$ with a particular gray value, and G is the number of possible gray levels. The maximum possible entropy value H_{max} occurs when all gray value fractions are equal. The final metric is then defined as

$$Q_3(\tilde{f}) = \frac{H}{H_{max}}. \tag{2.43}$$

Once again, minimizing Q_3 is assumed to lead to the correct AoR value.

The authors also express concern over the influence of noise on the metrics. To suppress noise in projection data, they opt to average several neighboring sinograms, and apply a Gaussian smoothing filter before reconstruction.

Cheng et al. [40] use a similar approach, but employ total variation as the metric:

$$TV(\tilde{f}) = \sum_{i=1}^{X} \sum_{j=1}^{Y} \tilde{f}_{Gr}(i,\ j), \tag{2.44}$$

where

$$\tilde{f}_{Gr}(i,\ j) = \sqrt{\tilde{f}_x(i,\ j)^2 + \tilde{f}_y(i,\ j)^2}, \tag{2.45}$$

$$\tilde{f}_x(i,\ j) = \frac{\tilde{f}(i+1,\ j) - \tilde{f}(i-1,\ j)}{2}, \tag{2.46}$$

$$\tilde{f}_y(i,\ j) = \frac{\tilde{f}(i,\ j+1) - \tilde{f}(i,\ j-1)}{2}. \tag{2.47}$$

AoR errors cause streak-like artifacts or double edges, so they are assumed to increase the total variation value of a reconstruction, because there are more differences between neighboring image elements. A gradient descent optimization scheme is thus applied to minimize the total variation as a function of AoR position. The method is also used to correct errors in the projection angle. [40]

2.5 Tomographic Reconstruction Software Packages

Prototyping new CT reconstruction algorithms is not an easy task. Practical application of basic operators, such as backprojection or formulation of the system matrix, is straightforward in principle, but may prove to be a major obstacle in reality. Fortunately, several publicly available software packages offer efficient implementations of these basic building blocks, allowing researchers to focus on more high-level parts of their reconstruction algorithms.

Among the most popular packages is the ASTRA toolbox, developed jointly by the University of Antwerp, Belgium, and the Centrum Wiskunde Informatica in Amsterdam, the Netherlands. [42, 43] In ASTRA, the core operators of CT reconstruction are implemented in the CUDA architecture, allowing for their acceleration on a Graphics processing unit. These operators then serve as building blocks for algorithms written in the C++ programming language. Finally, the toolbox allows its users to access all these tools in a user-friendly way, through high-level programming languages Matlab and Python. [42, 43] Only the Matlab interface is used in this work, so the subsequent text will only refer to this language.

The toolbox is composed of several modules which interact with each other in order to perform the desired reconstruction scheme. First are the data objects, which contain projection data and reconstructed volumes. They are stored outside of Matlab, allowing the lower-level layers of ASTRA to access them. [42, 43]

Linked to these data objects is information about their geometry. A volume geometry describes the dimensions of a generally anisotropic voxel grid, although in most cases, isotropic voxels are used. On the other hand, a projection geometry describes the size and number of projections, the relative distances between the beam source, scanned volume, and detector, and the trajectory of the source-detector pair.

Standard circular parallel-beam, fan-beam, and cone-beam projection geometries can be passed to the toolbox in a simplified manner, but any arbitrary scan trajectory can be modeled using ASTRA's vector-based geometry feature. In that case, the geometry is described completely and individually for each projection. This allows the user to specify non-standard scan trajectories, as well as misalignments of the source or detector, sample drift, and similar deviations from an ideal scan. [42, 43]

Information from the projection and volume geometries is used to implicitly determine a system matrix, which expresses how the object volume and its projections are connected. Depending on the data at hand, the system matrix can reach considerable sizes, so instead of storing the entire matrix explicitly, ASTRA uses ray-tracing techniques to generate only those values that are currently needed. [44] The user can then configure and run one of several built-in algorithms, including FDK and SIRT, or access the forward and backprojection operators themselves to develop new custom reconstruction schemes. [42, 43]

3 Limits of CT in Terms of Field of View

Projection data can be considered suitable for CT reconstruction if they fulfill a certain set of conditions. These conditions include all projection values being positive definite, the scan covering a sufficient angular range for the given geometry, and the object having a finite support contained entirely in the FoV. [1] The third condition is particularly limiting. Put into simpler terms, it means that the entire sample must fit into each of the acquired projections, the size of which is limited by the scanner's detector. This can cause problems in most CT applications, but particularly in high-resolution CT systems, where in some cases, samples may need to fit into an FoV in the order of single millimeters in diameter. [4]

When a sample extends beyond the reconstruction circle, the area fully supported by projection data, parts of the sample are visible in some projections, but not in others; the projections are truncated. Truncation results in artifacts, which in this case take the form of streaks and an erroneous accumulation of attenuation at the reconstruction circle's edges. The latter is caused by the way the reconstruction algorithm treats projection data; it attempts to place all the additional attenuation from outside the FoV on the edge of the image. [1]

Fortunately, imaging of samples larger than the FoV is possible, although it requires a slightly different procedure for data processing and reconstruction. There are two ways to approach this problem, depending on whether one wants to image the entire sample or only a specific part. In the first case, an FoV extension technique must be employed. [1] In the second case, a so-called local scan can be performed. [1, 45]

3.1 Local Tomography

Local tomography, also called *region-of-interest* (RoI) tomography, aims to reconstruct a part of a larger sample from truncated projections. [45, 46] The RoI is always in the scanner's FoV, while other parts of the sample outside this region sweep into and out of view. [1] Reconstructing such data is challenging; the so-called interior problem does not have a unique solution when a traditional FBP-type reconstruction algorithm is used. This is due to the intrinsically non-local character of the FBP algorithm. [45] Naive reconstruction of such data results in artifacts mentioned earlier; these are referred to as RoI artifacts in the subsequent text. [1]

Certain samples are particularly suitable for interior scanning. For example, if parts of the sample outside the FoV are made from a low-attenuating material, RoI artifacts may be negligible. Likewise, if the aim of imaging is not to evaluate the

sample quantitatively, but rather to inspect its shape or defects, RoI artifacts can be ignored. [1]

Various techniques have been used to improve the quality of RoI reconstructions. One approach is to combine high-resolution data of the region of interest with a coarse scan of the entire object. Implementing this strategy in practice is difficult, as the two sets of data have to be registered (aligned in terms of position) perfectly. Another, much simpler method is to pad the sides of the truncated projections, usually by a value from the edges of acquired data. [46]

In [47], [48], [49], and related works, researchers try to not only reduce RoI artifacts, but artificially extend the FoV by extrapolating measured data. This way, parts of the sinogram outside the original FoV are approximately recovered. Extrapolation is accomplished by looking at sine (or sine-like) curves that traverse measured values of the truncated sinogram, but also extend beyond them. Usually, the minimum of values measured along the curve is taken and used for completing the given curve. A superposition of all such extrapolations then forms a "completed" sinogram. [47, 48]

As an alternative, a statistical method can be employed that, based on available data, extends the sinogram so that an objective likelihood function is maximized. This approach also allows for regularization, as well as imposing certain consistency conditions on the extrapolated sinogram. [49]

Local tomography is an intensely studied area, and the list of approaches given here is hardly exhaustive. In addition to local tomography, a similar but distinct discipline, called interior tomography, exists. Unlike local tomography, which produces only approximate results, interior techniques aim for theoretically exact reconstruction of an RoI. [45] This is achieved through various means, such as introducing prior knowledge about the scanned region and using non-FBP-based algorithms. [45] These techniques are beyond the scope of this work.

3.2 Field of View Extension Techniques

In contrast to RoI imaging techniques, FoV extension attempts to overcome the limits of a CT scanner's detector and reconstruct tomograms of large samples in their entirety. In principle, there are two distinct ways to extend the FoV of a CBCT scanner: axially, for samples too long to fit into a single projection, and laterally, for samples too wide. [1] Obviously, both of these problems can be solved by increasing the detector's size, but this may not always be an option due to financial, spatial, or technical limitations. Instead, a number of approaches has been developed and described in the literature to extend the FoV in CT without the need for changes in scanner hardware. The following is a brief overview of some of these approaches.

3.2.1 Axial Field of View Extension

One solution to axial FoV extension is to simply perform multiple circular scans at different positions along the AoR, allowing for a small overlap between the edges of adjacent scans. Once all individual scans are reconstructed, they can be registered by matching up distinct features present in the overlaps. After registration, the individual smaller volumes are stitched, or combined, into one larger one. [50]

As an alternative, the authors of [51] have used a calibration phantom to precalculate the transformation matrices describing the relative shift between different CT volumes. Once all data is scanned and reconstructed, these precalculated transforms are applied to move volumes to their correct positions and allow for accurate volume stitching. While conceptually simple, such approaches may become challenging due to cone-beam artifacts mentioned in section 2.2.3, inaccuracies in sample stage movements, and other related complications. [51]

Axial FoV extension may also be achieved using a scan trajectory where the source-detector system changes its axial position throughout the scan. A helical trajectory is commonly used, where the source and detector simultaneously rotate around the sample and move linearly along the AoR. [1] An reconstruction algorithm suitable for this scan trajectory is then applied; typically, a Katsevich-type algorithm is used. First developed in 2002 [52], and subsequently expanded upon in works such as [53], [54], and others, Katsevich's formula is based on FBP and allows for theoretically exact reconstruction free of cone-beam artifacts when Tuy's condition is satisfied. [22] Although not as common, other reconstruction schemes, such as Grangeat's algorithm, are also applicable to the helical orbit. [22]

Helical scanning is popular in the medical sphere, where it is useful for scanning long portions of a patient's body. [2] It can also be utilized in industrial and scientific applications [1], when cone-beam artifacts need to be avoided or for particularly long and thin samples. The main disadvantage of a helical cone-beam trajectory is the much higher complexity of data acquisition compared to a circular scan. Reconstruction tends to be sensitive to sample deviations from the ideal position throughout the scan, so a very precise and accurate translational/rotational sample stage is required. [1]

3.2.2 Lateral Field of View Extension

Lateral FoV extension can be accomplished in several different ways. Many of these are commonly used in synchrotron X-ray tomography, a technique that utilizes a monochromatic and practically parallel-beam radiation source. [5] This setup has a number of advantages over conventional X-ray sources, such as a high photon density and excellent signal-to-noise ratio. [4] Techniques of lateral FoV extension

in synchrotron CT are introduced first, due to their relative conceptual simplicity. Then, techniques suitable for conventional CBCT are described.

Field of View Extension in Synchrotron CT

One approach of scanning large objects in synchrotron CT is to simply perform multiple overlapping local scans, reconstructing all subvolumes individually, and stitching the reconstructions together. When RoI artifacts caused by truncation are negligible, this method is very effective. This is not always the case, however, particularly for dense or very large samples. [5]

In a different but equally popular technique, the detector moves with respect to the sample's AoR. Note that in parallel-beam synchrotron CT, translating the detector is effectively equivalent to translating the sample along with its AoR. A naive approach would be to acquire multiple projections at one angle of rotation, then rotating the sample to acquire the next view. In practice, it is more efficient to scan a set of projections across the entire required angular range, then shift the sample along with its AoR and acquire another set of projections at this new position. This is repeated until the sample is scanned in its entirety, at which point all projections at corresponding view angles are merged, forming one large dataset. Before images can be merged, they have to be registered. For this, there must be sufficient overlap between neighboring images, so that their common features can be aligned. Finally, the merged set of projections is reconstructed. [5]

The authors of [5] additionally propose a new means of achieving a wider FoV. In it, multiple scans are performed, too, but without any AoR shift in between the scans. Instead, the object is shifted with respect to the AoR. After acquiring a sufficient number of datasets, projections can again be stitched together to form larger images. Whereas neighboring projections have a constant overlap in the previous method, the amount of overlap changes with the view angle in this case. This approach can be efficient when scanning samples with a relatively high aspect ratio, a significant difference between the sample's width and depth. Moreover, the authors have proposed an algorithm to combine this approach with the previous one, increasing the flexibility of both. [5]

The last commonly implemented method in synchrotron X-ray CT is referred to as half-object acquisition in [5]. Another suitable name for this technique is an offset scan, since it is a scan with an offset AoR. Projections are acquired across a full circular range of 2π radians. This is equivalent to two scans across a semi-circular range, with the AoR shifted between both. Since only a single scan is performed, no movement of the AoR between scans is necessary, reducing the possibility of errors caused by this shift. The AoR always stays in view, so it is possible to estimate its

position from the overlap between opposing projections. [5]

Field of View Extension in CBCT

An approach based on offset scanning is applicable to CBCT systems, as well. In practice, it is common to shift the detector to one side to achieve an offset AoR throughout acquisition. The displaced detector is shifted by less than half its width, resulting in an overlap of projection data around the AoR. This redundancy is accounted for by appropriately weighting the data. [6, 7, 8, 9]

In some cases, cone-beam data is rebinned to parallel-beam and an FBP algorithm is then used for reconstruction. [8, 9] Note that although the rebinned rays are parallel in the horizontal direction, they still diverge vertically, forming a tent-shaped beam. Interpolation has to be applied during rebinning, which may lead to lower spatial resolution of images. [9] Due to this, some approaches forgo the rebinning step, reconstructing the offset data using a cone-beam algorithm instead. [6, 7, 9, 60]

Other approaches to FoV extension in CBCT have been explored, as well. In [55], two separate scans are performed for different positions of the AoR. The smaller cone-beam projections are then rebinned into large, parallel-beam ones and FBP reconstruction is applied. The authors of [56] also propose a multi-scan approach, but avoid the rebinning step. Instead, they employ a different reconstruction algorithm based on differentiated backprojection, called backprojection-filtration. Three separate scans are performed at various AoRs and combined through this algorithm.

In [57], only a single scan is performed, but a unique hardware setup allows for the scanned object to be larger than the detector's FoV. The sample is placed on two off-centered rotational stages positioned on top of each other. As a result, the scanned object rotates with two degrees of freedom, and parts of it sweep in and out of view during acquisition. The acquired data is truncated, but contains enough information about the object for full reconstruction. Projections are therefore rebinned to wider, parallel-beam ones, and a standard FBP reconstruction scheme is applied.

4 Lateral FoV Extension for the Nano3DX

The focus of this work is to extend the FoV of the Rigaku Nano3DX X-ray microscope, and in particular the lateral extent of the FoV. Methods to extend the FoV mentioned in section 3.2.2 were considered. Out of these, extending the FoV by offsetting the sample AoR to one side was deemed the most suitable. It is convenient and easy to implement when compared to the other methods mentioned. It requires only a single scan over a 2π angular range, and allows for a FoV almost twice as wide as the detector array. Errors caused by shifting the AoR between scans, which can occur in multi-scan FoV extension techniques, are avoided here. On the other hand, the maximum potential amount of FoV extension is limited compared to methods where multiple scans are acquired. This drawback is presumably outweighed by the convenience of less image processing required before reconstruction. The implemented FoV extension method is referred to as the *offset-scan* approach from this point forward.

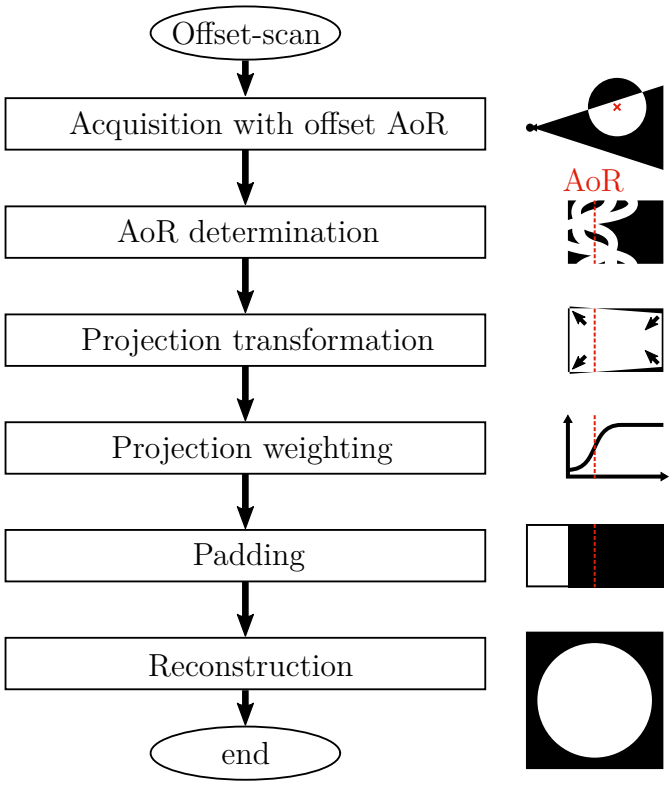

Fig. 4.1: Flowchart of the proposed method, along with pictograms for easier orientation.

The offset-scan method consists of several steps, which are summarized in fig. 4.1. First, projections of a sample with a shifted AoR are acquired. The next step is to determine the position of the AoR's projection. Projections are then transformed

onto a virtual detector to ensure the central ray is orthogonal to the detector plane. After the transform, rays around the AoR are weighted to account for redundancy. Finally, projections are padded to move the AoR to their middle, and the dataset is reconstructed. Individual steps are described in more detail in sections 4.2.2 through 4.2.5.

4.1 Rigaku Nano3DX

The Rigaku Nano3DX is an X-ray microscope capable of performing high-resolution CT measurements. [58] It utilizes a geometric setup where the sample is placed close to the detector and far from the radiation source, leading to a large *source-origin distance* (SOD), and a comparatively small *origin-detector distance* (ODD) (fig. 4.2). The X-ray image is converted to visible light upon hitting a layer of scintillating material. It is then magnified using optical elements contained within interchangeable units mounted in front of the detector. Multiple different optical units are available, offering varying amounts of magnification, resolutions, and FoV sizes. Finally, the magnified image is recorded upon hitting the detector array; during the course of this work, the Rigaku XSight Micron LC camera with a CCD array was used. [59]

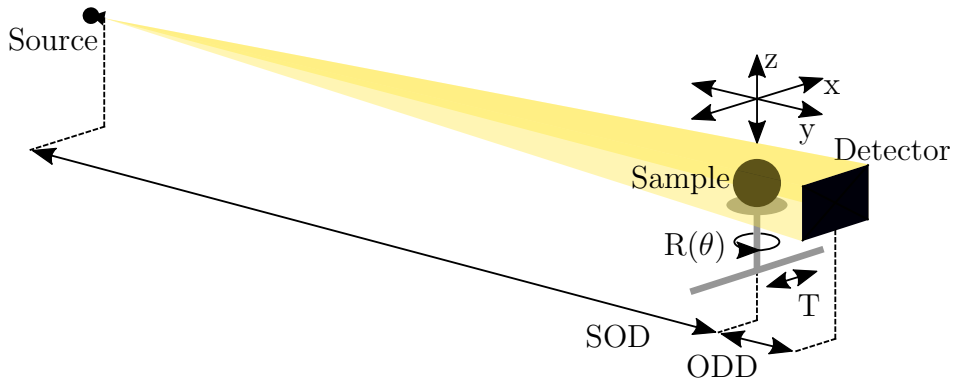

Fig. 4.2: Geometry of the Nano3DX, showing translation of the sample along the x, y, and z axes, rotation around the AoR parallel to the z axis, and translation of the AoR along the T-stage. The SOD is fixed. The ODD can be changed by translating the detector along the y axis. The figure is only illustrative; it is not to scale.

Advantages of the geometry utilized in the Nano3DX are mentioned in section 1.3. Most notably, this geometry results in very small divergence of the X-ray beam, and consequently a small amount of cone-beam magnification. Nevertheless, this amount is not negligible. To achieve a high degree of precision in reconstructed

data, the Nano3DX is treated as a CBCT scanner throughout this work, rather than a parallel-beam one.

The sample stage of the Nano3DX has five degrees of freedom, allowing for ample positioning of the sample for CT measurement. The user can move the specimen freely along all three axes of the scanned volume, as well as rotate it around an AoR parallel to the detector plane. The fifth and final degree of freedom, called the T-stage, controls the position of the AoR by shifting it along a line parallel to the detector and perpendicular to the AoR.

4.2 Field of View Extension Method

4.2.1 Projection Acquisition

The process of offset-scan projection acquisition is similar to a standard Nano3DX scan protocol. Exposure time per projection and angular step between consecutive projections are set according to the guidelines of the scanner's manufacturer. The two main differences from a regular scan are the angular range and the AoR offset. In standard scans, the angular range is shorter than a full 2π range to reduce the time necessary for acquisition, whereas an offset scan requires a full 2π range.

Offset of the sample's AoR is facilitated by a shift in the T-stage. While the detector can be moved towards, or away from, the sample stage, its position in the other two axes is fixed, so movement of the T-stage is the only means of shifting the AoR off-center. In CBCT, displacement of the detector is not equivalent to displacement of the AoR (fig. 4.3). Crucially, when the AoR is moved with respect to the source-detector system, the central ray is not perpendicular to the detector plane. [32] This must be taken into account.

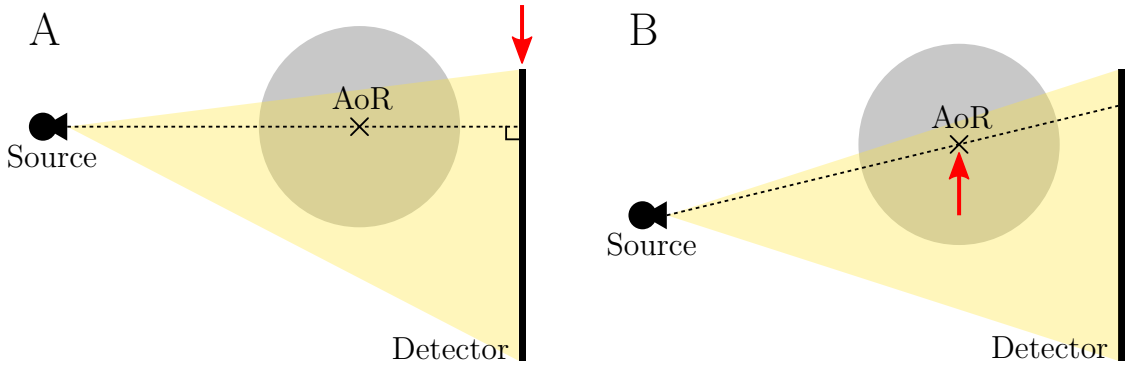

Fig. 4.3: An illustration of the difference between shifting the detector (left) and the AoR (right) in CBCT. The ray going through the AoR is orthogonal to the detector plane in the first case, but not in the second.

4.2.2 AoR Position Estimation

The most important aspect of the offset-scan method is to determine where the AoR projects onto the detector. Two approaches from section 2.4.1 are suitable for the offset-scan method: the sinogram symmetry approach of Lin et al. [32], and an algorithm based on reconstruction, based on the work by Donath et al. [33]. These automatic methods have the potential to accelerate AoR estimation tremendously, but they are also prone to fail or behave unexpectedly in some cases, such as when the noise level in a dataset is high. Therefore, a semi-automatic AoR determination approach is suggested (fig. 4.4).

In the proposed approach, both implemented automatic methods are applied, and their results are shown to the user, who can choose and, if needed, further adjust the better of the two. This user interaction can be accomplished via a graphical user interface, which allows for easy and intuitive manipulation. This workflow has the effect of speeding up the AoR estimation process, while increasing robustness in case the automatic methods fail.

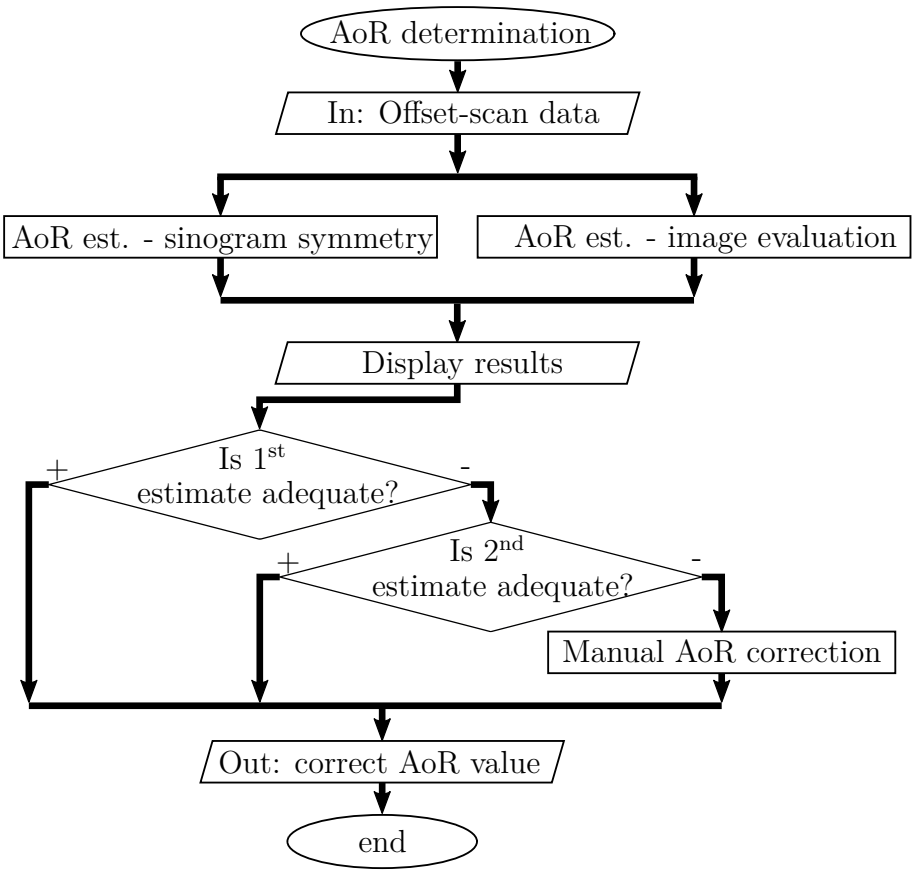

Fig. 4.4: Flowchart of the proposed AoR estimation workflow.

Estimation Through Sinogram Symmetry

Only the central slice of the dataset is used for AoR determination through the sinogram symmetry method in this work. Lin et al. [32] suggest the variance between both sides of the sinogram as an objective function to be minimized. Other functions are possible, if they satisfy the requirement of being optimal for the correct AoR. This means that the value of the function must either increase or decrease as the AoR estimate approaches the correct value. The implementation utilized in this work uses the Euclidean distance between both halves, as in fig. 4.5. Based on eq. (2.38) and the Euclidean distance, an objective function Q_s is formulated and minimized to estimate the position of the AoR:

$$Q_s(p_0) = \frac{1}{N}\sqrt{\sum_{i=1}^{N}\left(\sum_{j=1}^{M} P(\beta_j,\, V_i) - \sum_{j=1}^{M} P(\beta_j,\, V_i')\right)^2}, \tag{4.1}$$

where p_0 is the current assumed AoR position in sinogram P, and M and N are the number of projections and number of overlapping pixels, respectively.

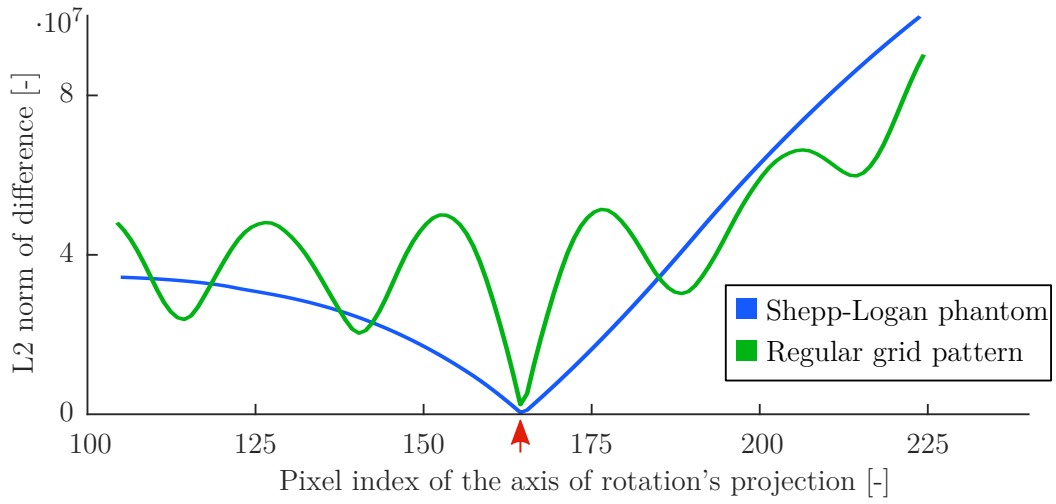

Fig. 4.5: Euclidean distance between both halves of a sinogram as a function of the position of the AoR's projection. Two such curves are shown, blue for a sinogram of the Shepp-Logan phantom, and green for a sinogram of a regular grid pattern. The minima of both curves, marked by a red arrow, correspond to the estimated position of the projected AoR.

Estimation Through Tomogram Evaluation

The central slice sinogram of the acquired dataset is used for the tomogram evaluation method, too. In order to suppress noise, a smoothing filter with a Gaussian

kernel is applied to the sinogram prior to reconstruction. The filter used here has a standard deviation of $\sigma = 3$, with a kernel size of 13 by 13 pixels. [33] These parameters were chosen empirically, based on tests of the AoR estimation method.

For a given AoR estimate, the sinogram is reconstructed using the ASTRA implementation of a fan-beam FBP-type algorithm, which is equivalent to reconstructing the central slice using FDK. To decrease the time-cost of reconstruction, the tomogram is subsampled by a certain factor. For the particular data used to test the offset-scan method, introduced in section 4.3, a factor of four was chosen as a compromise between speed-up and spatial resolution. For different datasets, this factor can be automatically adjusted as a function of their size.

After reconstruction, a formula based on eq. (2.40) is used to acquire a score for the current reconstruction. In this work, the reconstruction algorithm is implemented in such a way that the size of the FoV changes with the position of the AoR. To account for this, eq. (2.40) is divided by the total number of pixels in the current FoV. Division by m_0, the average projection weight, is not used here, because the projections are truncated. These modifications lead to the metric Q_r:

$$Q_r(\tilde{f}) = -\frac{1}{XY}\sum_{i=1}^{X}\sum_{j=1}^{Y} u(-\tilde{f}(i,\, j))\tilde{f}(i,\, j), \tag{4.2}$$

where X and Y are the width and height of the current FoV in pixels. The minimum of Q_r is then found and taken as the correct AoR estimate. Examples of such curves are shown in fig. 4.6.

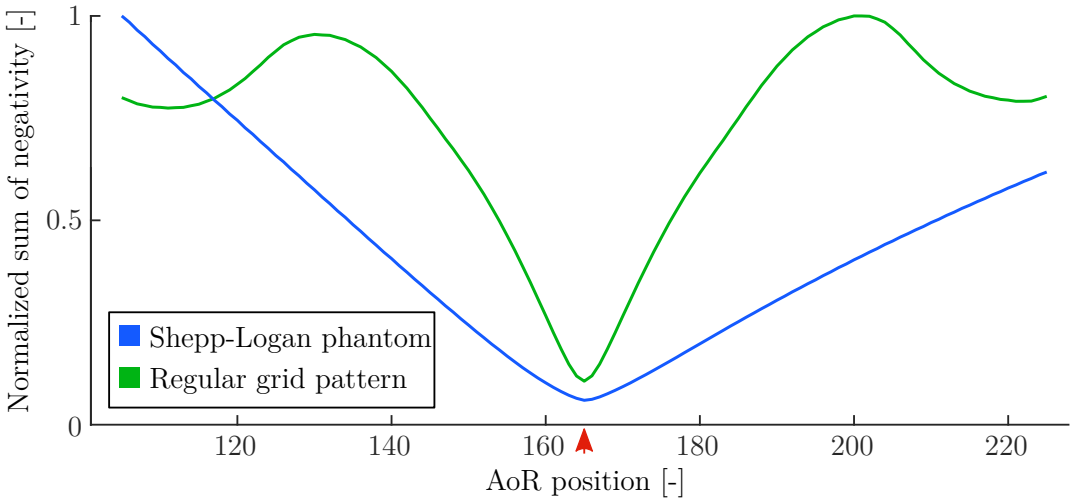

Fig. 4.6: Example of an AoR estimate based on the sum of negative values in reconstructed images. Two examples are shown, one for the Shepp-Logan phantom, and another for a regular grid pattern. The minima of both curves, highlighted by a red arrow, mark the AoR estimate.

Automatic AoR Estimation Trials

Both methods were tested on a selection of synthetic images, primarily the ones mentioned in section 4.3. Manually determined AoR values were used as the ground truth, with which the methods' results were compared. Various types of noise were added to the synthetic data, including Gaussian noise, Poisson noise, impulse noise, ring artifacts, and a gradual decrease of projection intensity throughout the scan. Altogether, 110 synthetic datasets were used, with the aforementioned noise applied both individually in different amounts, and together. The latter simulated a real scan situation with a multitude of noise sources, while the former served to isolate the effects of different noise types on AoR estimation. Additionally, both methods were applied to six physical offset-scan datasets, to examine how they perform in a real-world setting. Based on these tests, neither method could be deemed conclusively superior to the other, leading to both implementations being used in the final proposed approach.

A major advantage of the algorithm based on sinogram symmetry is its relatively fast computation time. In tests on synthetic data, it performed very well, even in the presence of Gaussian, Poisson, and impulse noise. On the other hand, the presence of ring artifacts was detrimental to the performance of this method. In the sinogram domain, ring artifacts manifest themselves as streaks, biases of individual detector bins. This artificially increases the difference of corresponding bins on either side of the sinogram, and potentially leads to false results. A gradual decrease in projection intensity did not severely influence the method's accuracy, but it did lead to a smaller difference between the value of the metric's optimum and nearby values. This might lead to a decreased robustness when additional types of noise are present. When applied to real data, the method performed fairly well, yielding estimates within five pixels of the correct value for all tested datasets. To work reliably in the presence of noise, this method needs a sufficient overlap of projection data in the region around the AoR. The position of the AoR must therefore be at a reasonable distance from the edge of projections.

The tomogram evaluation method tended to perform well in many cases where the sinogram symmetry method failed, namely in the presence of ring artifacts. On the other hand, it performed poorly in the presence of impulse noise. Datasets with high-contrast, heterogeneous features are particularly well-suited for this algorithm. On the other hand, highly homogeneous samples often led to incorrect results. Additionally, the estimates took significantly longer to compute than the sinogram symmetry method. When applied to real data, it showed worse results than the sinogram symmetry method in about half the cases, and better results in the other half.

Overall, the sinogram symmetry method correctly predicted the AoR for nearly half of all synthetic datasets, and was within several pixels of the correct estimate in the vast majority of tested cases. The tomogram evaluation method was correct in more than 58% of cases, and within two pixels of the correct AoR in almost 70%. When combined, at least one of the two methods was correct more than three quarters of the time, and within two pixels of the AoR in more than 95%. The threshold of two pixels was chosen arbitrarily to show that even when the estimate is not correct, it often tends to be close to the correct value.

These results, summarized in table 4.1, exemplify the merit of applying both methods during AoR estimation, and showcase the need for occasional manual correction of the automatic estimates. For real data, at least one of the two methods was within two pixels of the manually determined AoR for four out of the six datasets.

Tab. 4.1: Performance of AoR estimation methods on synthetic data.

Method	Correct estimation [%]	Within two pixels of the correct AoR [%]
Sinogram symmetry	47.27%	93.64%
Tomogram evaluation	58.18%	69.09%
Both methods	75.45%	96.36%

4.2.3 Projection Transform

Reconstruction algorithms based on FBP, such as FDK, assume that the beam's central ray intersects the AoR, is perpendicular to it, and is orthogonal to the detector plane. [1] In this work, the sample and its AoR are offset, and the assumption above does not hold true. This is rectified by transforming projections onto a virtual detector, slightly rotated relative to the real one. Note that a similar approach was recently described by Lin et al. [60], but it is independently derived here.

Interpolation has to be used, since the virtual detector grid does not line up with the real one. This can potentially degrade the spatial resolution of images. [9] However, when cone angles are relatively small, the applied transform is subtle and interpolated datapoints are spatially close to actual measurements. Therefore, loss of spatial resolution is assumed to be minimal.

All values in this section are in pixels for the sake of convenience, and can be scaled after the fact if necessary. Individual detector columns are indexed from the left by $i \in \{1, 2, \ldots, K\}$, and rows from the top by $j \in \{1, 2, \ldots, L\}$. The coordinate system used is centered on the point where the AoR intersects the middle row of the detector, with the x axis parallel to the detector plane, and the y axis orthogonal

to it. It is also assumed that the ray hitting the central column of the detector is orthogonal to it, which can be ensured by proper alignment before the actual measurement. Figure 4.7 illustrates the transform.

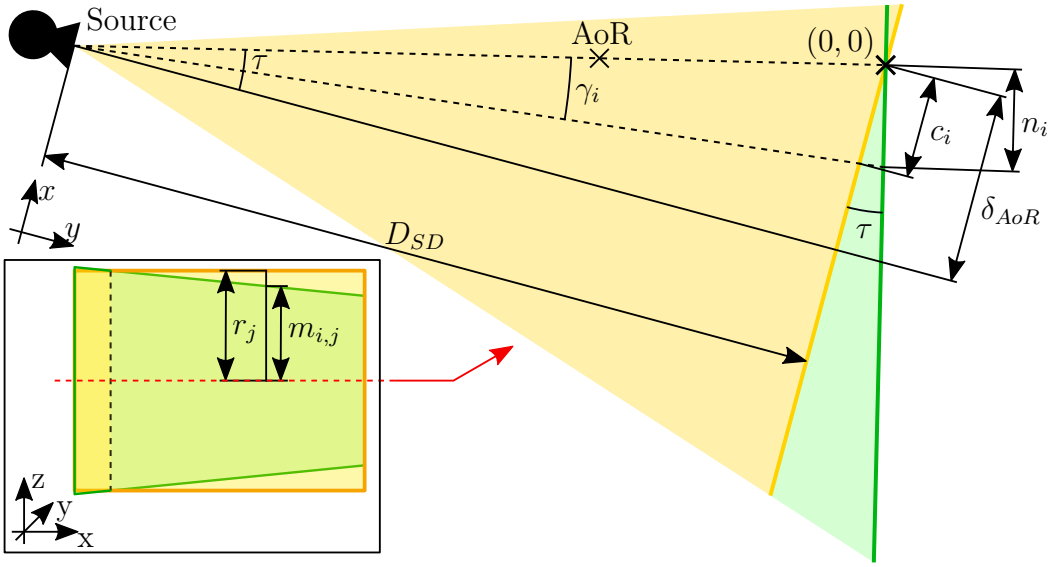

Fig. 4.7: An illustration of the transform of projections onto a virtual detector. Both detectors are viewed from the viewpoint of the X-ray source in the lower left, as well as from the top. Important points and distances are labeled. The real detector is shown in yellow, the virtual one in green.

The virtual detector is rotated around the AoR by an angle τ relative to the real one:

$$\tau = \arctan\left(-\frac{\delta_{AoR}}{\mathrm{SDD}}\right), \tag{4.3}$$

where δ_{AoR} is the signed distance of the projection of the AoR from the detector's midpoint, and the *source-detector distance* (SDD) equals the sum of SOD and ODD.

The midpoint of each column is a certain distance away from the AoR's projection:

$$c_i = i - \frac{K+1}{2} + \delta_{AoR}. \tag{4.4}$$

Next, the angle between the ray going through the AoR and rays hitting each detector column is obtained:

$$\gamma_i = \arctan\left(\frac{c_i}{\mathrm{SDD}}\right), \tag{4.5}$$

The values τ and γ_i are then used to determine where values measured at real detector bins project onto the virtual detector. Distances from the AoR of these projections along the virtual detector are calculated using the sine rule:

$$n_i = c_i \cdot \frac{\sin(\frac{\pi}{2} - \tau + \gamma_i)}{\sin(\frac{\pi}{2} - \gamma_i)}. \tag{4.6}$$

The relationships between angles used in eq. (4.6) are shown in the left part of fig. 4.8. Since the virtual detector is rotated by τ from the original array, each of its columns is at a different distance from the source. This causes a change in cone beam magnification at each detector bin:

$$M_i = \frac{\mathrm{SDD} + \sin(\tau) \cdot n_i}{\mathrm{SDD}}. \tag{4.7}$$

Using M_i, the distance of each pixel from the middle row of the detector is

$$m_{i,j} = \frac{r_j}{M_i}, \tag{4.8}$$

where r_j is the distance of detector rows from the middle row:

$$r_j = j - \frac{H_r + 1}{2}. \tag{4.9}$$

The points where measured samples project onto the virtual detector are described by n_i and $m_{i,j}$. It is now a matter of applying an appropriate interpolation scheme to acquire equispaced samples at the virtual detector. Here, the pixel pitch of the real detector was preserved for the sake of convenience, and cubic spline interpolation was used.

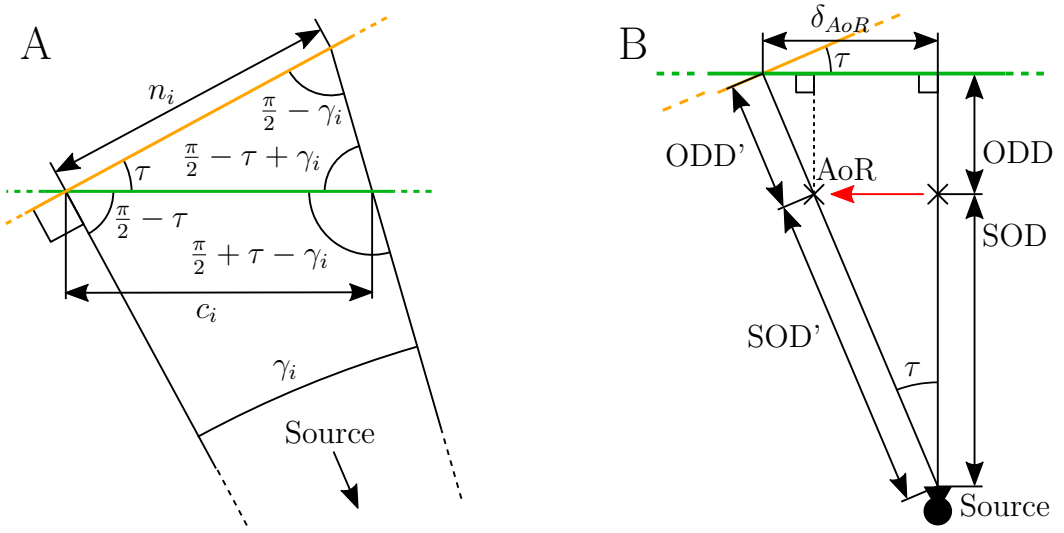

Fig. 4.8: Geometric relationships between the real and virtual detector. Angles used for calculating n_i are shown in A, and distances between the source and the virtual and real detectors are shown in B.

This transform shifts all projection angles by τ. Additionally, the distances between the X-ray source, AoR, and detector all change. To arrive at the new

values SOD' and ODD', Pythagoras' theorem can be applied:

$$\mathrm{SOD}' = \sqrt{\mathrm{SOD}^2 + \left(\delta_{AoR} \cdot \frac{\mathrm{SOD}}{\mathrm{SDD}}\right)^2}, \tag{4.10}$$

$$\mathrm{ODD}' = \sqrt{\mathrm{ODD}^2 + \left(\delta_{AoR} \cdot \frac{\mathrm{ODD}}{\mathrm{SDD}}\right)^2}. \tag{4.11}$$

An illustration of these distances is shown in fig. 4.8 on the right. An example of a transformed synthetic projection is shown in fig. 4.9.

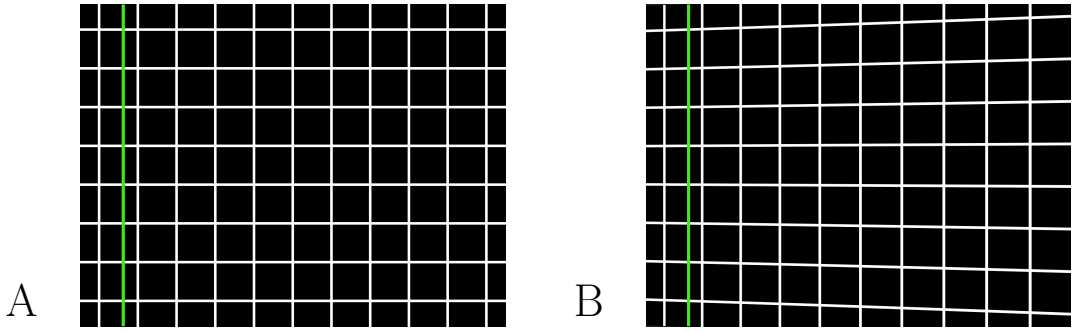

Fig. 4.9: An example of a transformed projection, exaggerated to better demonstrate the effect. The transform is applied on the original projection (A) to obtain the transformed one (B).

A transform of the sinogram is necessary in the AoR estimation method described in [32], too. It is, however, simplified to require less computation (fig. 4.10). The datapoints do not need to be equispaced, but they must be distributed symmetrically around the current AoR. Therefore, datapoints on one side of the AoR can be taken directly, and on the other side, interpolation is used to obtain values at matching points. Also, since only a single sinogram is processed in this case, the transform operates on 1-D data instead of 2-D projections.

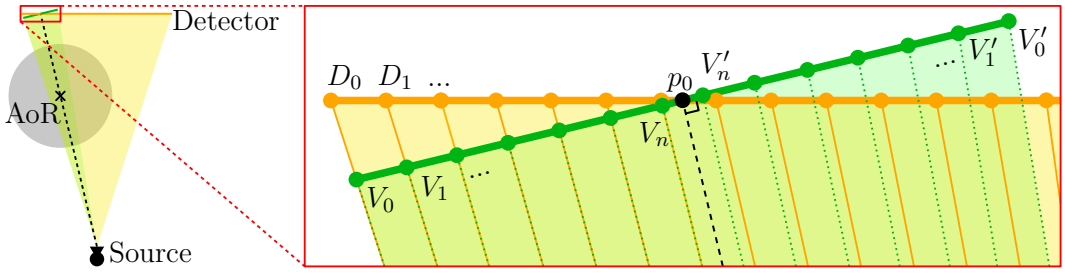

Fig. 4.10: Projection transform used for AoR estimation. Values to the left of p_0 are taken directly, virtual values to the right are obtained through interpolation. Only a small section is transformed to obtain values from V_0 to V'_0.

4.2.4 Projection Weighting

The transformed projections then need to be weighted. Data in a small region around the AoR is scanned twice throughout the 2π scan, whereas in the outer regions of the sample volume, each ray is recorded only once. Weighting redundant data in fan-beam and cone-beam projections is a common issue, and it has been described thoroughly in the literature. Notably, Parker has used a sinusoidal weighting function to account for superfluous rays in short-scan data. [61] A number of other works, such as [62] and [63] have since expanded upon Parker's original work.

Weighting redundant data in an offset scan is in principle very similar to weighting short-scan data. An intuitive approach is to remove redundant parts of projections by setting their values to zero. This is a poor solution, as streak artifacts form in FBP-based reconstructions of such data, due to the sharp discontinuity created at the boundary between removed and intact data. [61, 62] To avoid creating such sharp disruptions in projection data, a smooth weighting function can be applied. In addition to smoothness, such a function must fulfill two other requirements: the weight for non-redundant data is one, and the sum of weights for two datapoints carrying the same information must also be equal to one. [61, 62]

A sinusoidal profile is a common and appropriate choice for this type of weighting function. In the case of offset data, a constant weight of one is applied to data in peripheral parts of the sample volume. Around the AoR, a sine wave weights the overlapping central region, gradually decreasing in value from one to zero as it approaches the edge of measured data. [9] This weighting function can be expressed as

$$w(p) = \begin{cases} 1 & \text{if } \; p > p' \\ \frac{1}{2}\sin\left(\frac{\pi p}{-2p'}\right) + \frac{1}{2} & \text{if } \; -p' < p < p' \\ 0 & \text{if } \; p < -p', \end{cases} \tag{4.12}$$

where $\langle -p',\, p' \rangle$ is the range of overlapping data around the AoR's projection at p_0. [9] An offset-scan sinogram weighted by eq. (4.12) is shown in fig. 4.11. In this figure, the sinogram has been padded with zeroes to move the AoR to the center of projection data. Other approaches have been proposed, but these are based on the same general principles as the one described, and result in very similar profiles of weighting functions. [6, 7, 8]

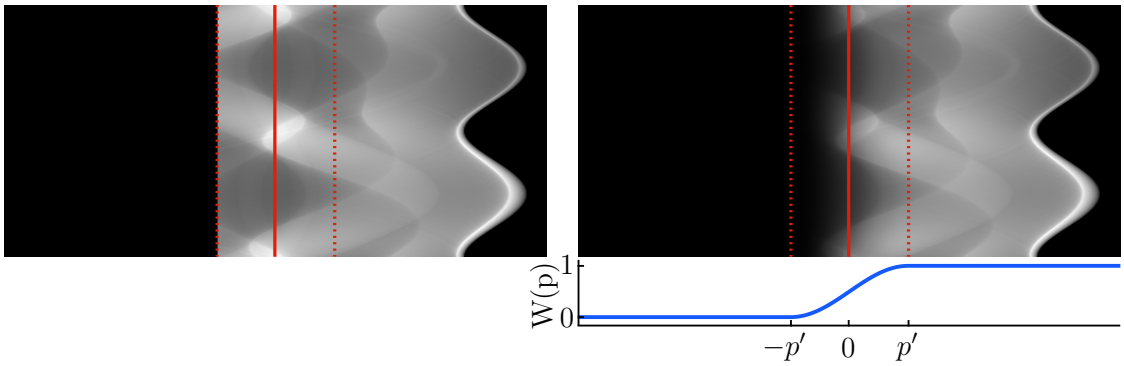

Fig. 4.11: An unweighted offset-scan sinogram is shown on the left, padded with zeroes on its left side, so the AoR (the solid red line) is in the middle. The dashed red lines show the overlap range $\langle -p', p' \rangle$. The same sinogram with the weighting function 4.12 applied is on the right. A profile through the weighting function is shown below the sinogram.

4.2.5 Padding and Tomographic Reconstruction

After determining the AoR's, transforming projections, and weighting the overlapping region, an appropriate reconstruction algorithm can be applied to recover a tomographic slice of the sample. In the proposed approach, projections are padded by zeroes first to move the AoR to the center of projections. Since no fan-to-parallel rebinning operation is applied, a common cone-beam reconstruction algorithm can be used, such as FDK. Rebinning can decrease the spatial resolution of data, so avoiding it potentially helps preserve finer details in images. [9] Note that interpolation has to be applied in a previous step, when projections are transformed onto the virtual detector. Avoiding a second such operation here is desirable.

The ASTRA toolbox implementation of the FDK algorithm was used for reconstruction of both standard and offset-scan data throughout this work. The filter used during reconstruction was a cosine-apodized ramp filter with a cut-off at 0.85-times the Nyquist frequency. Additionally, all projection datasets were padded by ten pixels on the left and right prior to reconstruction to reduce potential truncation artifacts.

4.3 Practical tests of the offset-scan method

The offset-scan FoV extension method was tested using various synthetic and real samples. The results were compared to standard reconstructions of data obtained using a larger detector array, and the merits of the offset-scan approach were evaluated through both subjective quality assessment and objective metrics.

The following text first introduces the images used for creating synthetic data. Next the process of simulating data acquisition is briefly described. Choice and projection acquisition of real samples is then also elaborated on. A summary of methods chosen to evaluate both synthetic and real data follows. Finally, a summary of results and discussion for both synthetic and real data closes out this chapter.

4.3.1 Materials and methods

Synthetic Data Creation

Five synthetic images were used in this study. The first four represented samples with features of various levels of complexity (fig. 4.12). An image containing five concentric rings was chosen as the least complex type of structure. Next, a forty-pronged Siemens star and a regular grid pattern represented objects containing more elaborate, yet still regular structures with a single brightness level. The Shepp-Logan phantom [64] served as an example of a somewhat irregular structure with multiple brightness levels. The last was a line-pair phantom, which was used to compare the resolution of offset-scan reconstructions to those created using a larger detector (fig. 4.13). The phantom consisted of patterns of 0.5, 0.25, 0.125, and 0.0625 *line pairs* (LP) per pixel, with five LP in each group. The original size of all images was 2966 by 2966 pixels.

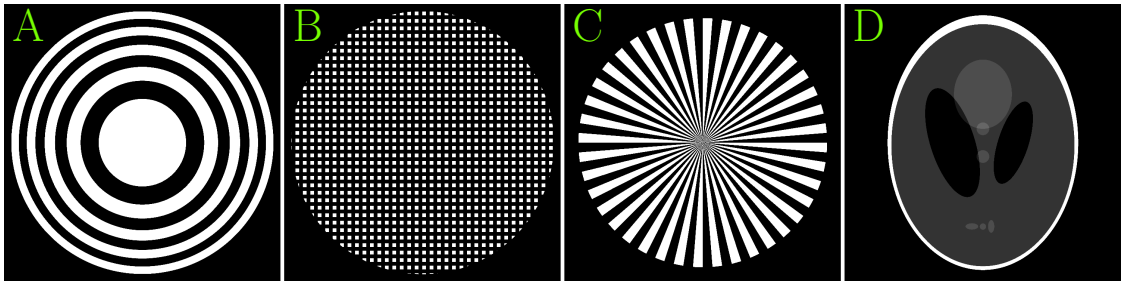

Fig. 4.12: Synthetic data used for validation of the proposed method: concentric rings (A), grid pattern (B), forty-pronged Siemens star (C), Shepp-Logan phantom (D).

Two sets of projections were formed for each image, using the forward projection operation implemented in the ASTRA toolbox. The first, offset-scan dataset used a 1648-pixel linear detector array, with its FoV extended 1.8-fold by offsetting the AoR. The second used a wider, 2966-pixel linear detector array, which accommodated the entire support of the image, and served as a reference standard CT measurement. Such datasets are referred to as a full-detector in the subsequent text. Both types of projection data featured 1600 views over a 2π angular range. This particular

amount of views was chosen to correspond with the amount recommended by the manufacturer of the Nano3DX. This resulted in a total of ten projection sets, five offset-scan and five full-detector. Two of these are shown in fig. 4.14. All projection sets were then reconstructed and evaluated.

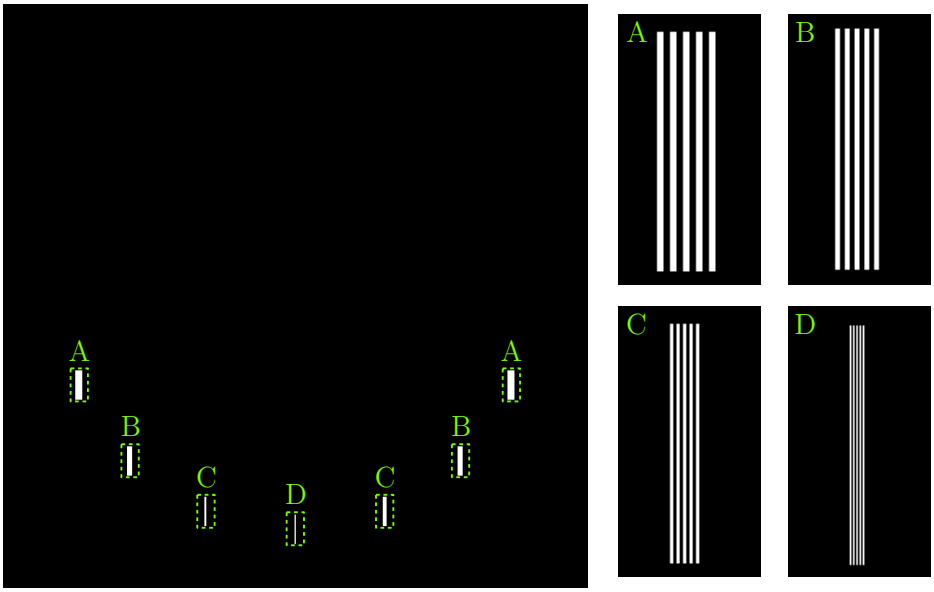

Fig. 4.13: Phantom used to compare the resolution of the offset-scan approach to that of a standard reconstruction. Details labeled A, B, C, and D show patterns of 0.5, 0.25, 0.125, and 0.0625 LP per pixel, respectively. The phantom is symmetric laterally.

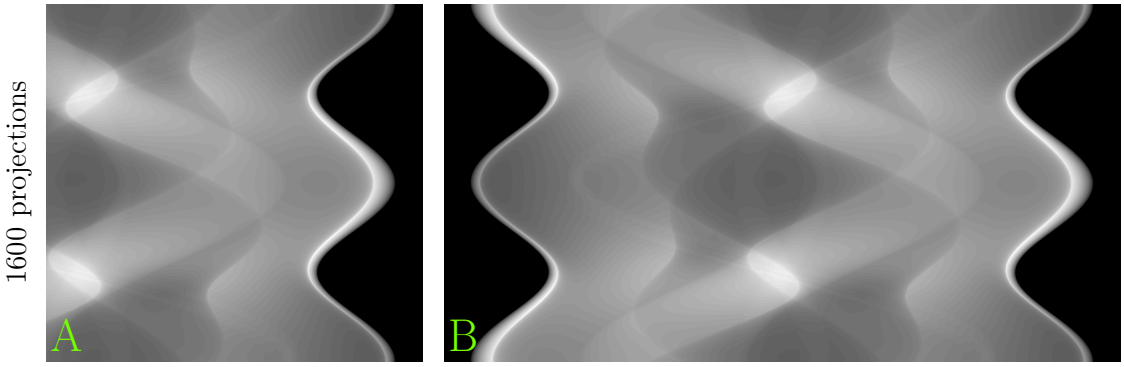

Fig. 4.14: An example of an offset-scan (A) and full-detector (B) sinogram of the Shepp-Logan phantom.

Real data acquisition

Three samples were chosen to test the offset-scan method in a real measurement setting. The samples varied in complexity, and covered a range of typical measurement scenarios. The structurally simplest specimen was a solid plastic construction toy piece. A pill was chosen as an example of a more complicated sample. Lastly, a carbon fiber reinforced polymer, which contains a multitude of irregular structures, was chosen as the most complex specimen.

In order to compare offset-scan reconstructions with a reference conventional CT scan, each sample was scanned twice with different FoVs. This was accomplished by switching the optical unit in front of the detector between the two scans. The units used here facilitated 2.5× and 5× magnification, leading to effective nominal pixel sizes of 2.16 and 1.08 micrometers, respectively. The optical units are referred to as the 2.5× unit and the 5× unit from this point forward. The 5× unit was used for offset scans, whereas full-detector reference scans were carried out using the larger 2.5× unit. The FoV of the 5× unit was extended about 1.8 times laterally by offsetting the AoR. This resulted in a total of six datasets, whose parameters are summarized in table 4.2. A copper anode with a tube voltage of 40 kV was used for X-ray generation. The anode current was 30 mA. Note that while the 2.5× lens unit offers twice the axial extent of the 5×, only the central 50% of full-detector projections were reconstructed, since the areas outside this range were not present in offset-scan datasets, and thus irrelevant for the comparison.

Tab. 4.2: Parameters of measurements.

Dataset	offset-scan	reference scan
Pixel size [µm]	2.16	2.16
Binning	2×	1×
Projection size [pixels]	1650 × 1250	3298 × 2500
Original FoV width [mm^2]	3.6 × 2.8	7.2 × 5.6
Approximate FoV extension	1.8×	–
Number of projections	1600	820
Angular range	360°	184.5°

Exposure times were adjusted individually for each scan, and are summarized in table 4.3. They were chosen to ensure a sufficient level of signal for the given measurement setups, as recommended by the manufacturer of the Nano3DX. Binning was used when acquiring offset-scan data, leading to a comparable pixel size in both offset-scan and reference projections. For the full-detector scans, a short-scan angular range of 184.5 degrees was chosen to both acquire a sufficient amount of

projection data for a CBCT scan, and decrease scan time when compared to a full 2π scan. The angular step between projections was the same for all offset-scan and full-detector datasets.

No additional pre-processing, such as noise reduction, cupping artifact reduction, or ring artifact reduction, was applied prior to the reconstruction process described in section 4.2.5. This led to a reduced quality of resulting tomograms, but also allowed a more direct comparison of reconstructions without any added bias introduced by image processing.

Tab. 4.3: Exposure times per projection and total measurement times for each of the six measured datasets.

Sample	Time per projection [s] 5× / 2.5×	Total time [s] 5× / 2.5×
Construction toy piece	7.5 / 23	14 494 / 21 473
Pill	7.5 / 25	14 494 / 23 146
Carbon fiber reinforced polymer	4.5 / 16	10 153 / 15 570

Assessment of results

Evaluation of the resulting reconstructions is split into subjective visual assessment and objective *image quality assessment* (IQA) metrics (listed in table 4.4). IQA metrics are useful for quantifying the quality of an image by condensing it into a single scalar value using well-defined mathematical operations. [65] Here, they are used to provide an easy means of comparing offset-scan and full-detector reconstructions. Visual evaluation is then used to try and identify any specific differences and nuances. The following is a description of evaluation of synthetic data, followed by a summary of how real reconstructions were assessed.

Tab. 4.4: A summary of IQA methods used for objective evaluation in this work.

Image quality index	Metric type	Application	Based on:
PSNR	Full-reference	Simulated data	Difference of images
FSIM	Full-reference	Simulated data	Structural similarity
NIQE	No-reference	Real data	Natural scene statistics

Objective assessment of simulated data consisted of the full-reference IQA metrics *peak signal-to-noise ratio* (PSNR) [65] and *Feature Similarity Index* (FSIM) [65, 66]. It is advantageous to use full-reference metrics when the original undistorted image is available, as was the case here. When calculating PSNR, a built-in Matlab

function was used to obtain the images' mean squared error, which is the basis of the used metric. For FSIM, the Matlab code provided by its authors [66] was utilized. A copyright notice for the code is included in appendix B.

PSNR was chosen for its ubiquity, ease of computation, and clear meaning as a measure of difference between the reference and distorted images. Its main disadvantage is poor correspondence with subjective quality assessment. Therefore, FSIM was used as a secondary metric to more closely simulate a human observer's judgment of image quality. It uses phase congruence to measure the significance of local image structures. To account for changes in contrast, which phase congruence is invariant to, gradient magnitude of the image is incorporated into the final value of FSIM. [65, 66]

Subjective assessment of simulated data consisted of comparing offset-scan and full-detector reconstructions, and identifying any visible differences. In particular, attention was paid to any potential artifacts or changes in scale or shape of offset-scan data. For the LP phantom, profiles of line pairs were plotted for both reconstructions and compared to examine the effect of the offset-scan method on spatial resolution.

For the reconstruction of real data, objective evaluation was performed using the *Natural Image Quality Evaluator* (NIQE) [67]. NIQE is a no-reference metric, which can be utilized when an undistorted original is not available. It needs to be trained on a dataset of images, but it does not require any information about the quality of images in this dataset, because it is a so-called opinion-unaware metric. It is also not confined to identifying any specific type of image distortion. [65, 67] NIQE divides an image into multiple patches and extracts natural scene statistical features from these areas at two scales. A multivariate statistical Gaussian model is constructed from these features. Evaluation then consists of comparing this model to a reference one, constructed using the training dataset. The distance between the two models is the final metric of quality, meaning higher-quality images receive lower scores. [65, 67]

In this work, the Matlab implementation of NIQE was used. It was trained on a dataset of 62 tomographic slices from nine Nano3DX datasets of biological and industrial samples; thus, the final model was based on a wide range of typical Nano3DX data. Evaluation was carried out as follows: a NIQE value was assigned to every slice of a reconstruction, values for the first and last ten slices were discarded to avoid the influence of incomplete data, and the rest was averaged to yield a single value for one dataset.

Subjective evaluation of real reconstructed slices was in part similar to the process used for simulated results, but it was confounded by the complex nature of real data. It was important to distinguish between differences caused by FoV extension,

other unrelated artifacts, and differences caused by factors other than the offset-scan method. Furthermore, the surface of each sample was determined by applying a global threshold on intensity values, and three-dimensional surface models were also compared visually. The threshold used was set manually.

4.3.2 Results

Evaluation of reconstructions shows that the implemented FoV extension technique produces images on a par with a standard measurement using a wider detector. There is no perceivable degradation of reconstructions caused by the offset-scan method itself. The following section describes the results of evaluating both simulated and real tomographic data with a laterally extended FoV.

Synthetic Data

Objective metrics calculated for simulated data (listed in table 4.5 and table 4.6) show that offset-scan reconstructions are only slightly lower than full-detector ones. This may be caused by the fact that full-detector datasets intrinsically contain less noise when a full 2π scan range is used, since every ray is ideally measured twice. For offset-scan data, this is only true in a small region around the AoR, whereas data corresponding to more distal areas of the sample are measured once.

Tab. 4.5: Objective image quality metrics for simulated data. The last column features the percentual difference of offset-scan values when compared to full-detector ones, for easier comparison (the higher the number, the better).

Dataset	PSNR [dB] (full detector)	PSNR [dB] (offset scan)	Difference of offset-scan compared to full-scan [%]
Concentric rings	22.8882	22.1044	-3.42
Grid	14.3046	13.9259	-2.65
Siemens star	16.1927	14.1861	-12.39
Shepp-Logan	28.2305	27.2413	-3.50

For the concentric circles dataset (fig. 4.15), there is hardly any perceivable difference between the two reconstructions. Both PSNR and FSIM values are comparatively high, and there is little difference between the metrics for either reconstruction.

Tab. 4.6: Objective image quality metrics for simulated data. The last column features the percentual difference of offset-scan values when compared to full-detector ones (the higher the number, the better).

Dataset	FSIM [-] (full detector)	FSIM [-] (offset scan)	Difference of offset-scan compared to full-scan [%]
Concentric rings	0.9866	0.9837	-0.29
Grid	0.9112	0.8946	-1.82
Siemens star	0.9584	0.9247	-3.52
Shepp-Logan	0.9778	0.9737	-0.42

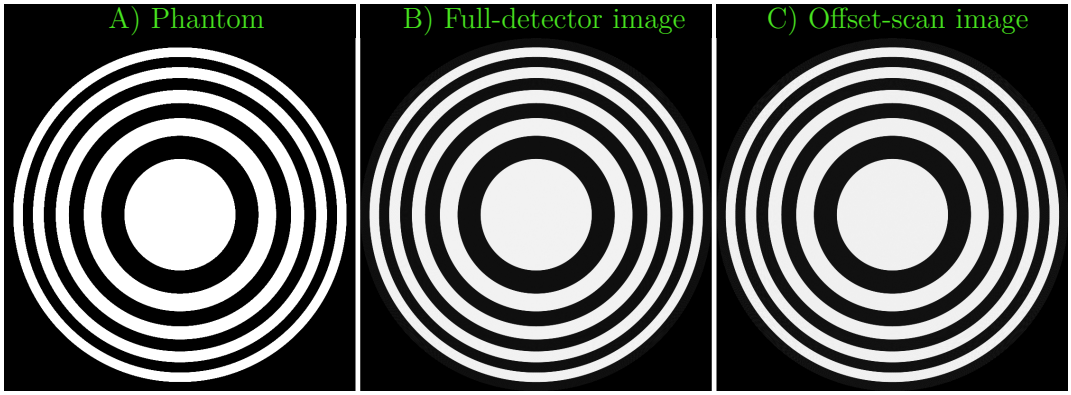

Fig. 4.15: Concentric circles (A) and their full-detector (B) and offset-scan (C) reconstructions.

The grid pattern images (fig. 4.16) contain many high-contrast edges, which are the source of streaks in reconstructions. As a result, these images have the lowest PSNR and FSIM of all evaluated samples. The offset-scan values of both metrics are relatively close to full-detector ones, however, which speaks in favor of the implemented FoV extension method. It means that the streak artifacts are not more pronounced in the offset-scan dataset, but rather that both images are affected to a similar degree.

The largest discrepancy between full-detector and offset-scan values of both PSNR and FSIM was observed for the Siemens star. Upon closer inspection (fig. 4.17), the offset-scan data are distorted in the center, close to the prongs' meeting point. This is not a fault in the offset-scan method itself, but rather in an insufficient amount of angular sampling required for the amount of detail present in this particular image. After doubling the number of projection views to 3200, the observed distortion disappears, as shown in fig. A.1 in appendix A. It is of note that in the full-detector reconstruction, no such artifacts appear even in the 1600-view dataset.

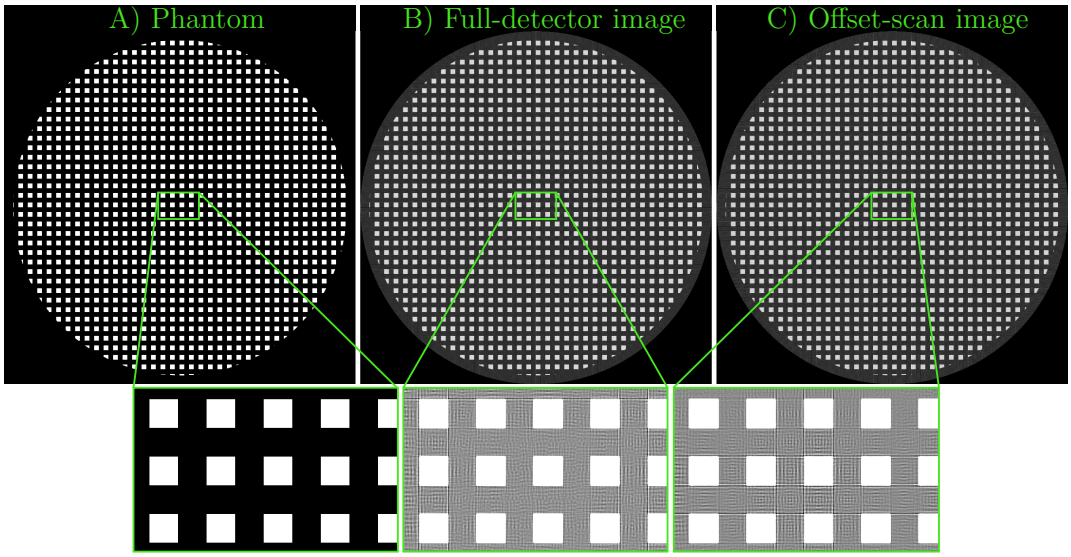

Fig. 4.16: A grid pattern (A) and its full-detector (B) and offset-scan (C) reconstructions, with details of the center area. The contrast of the detail cutouts is increased to show the artifacts present.

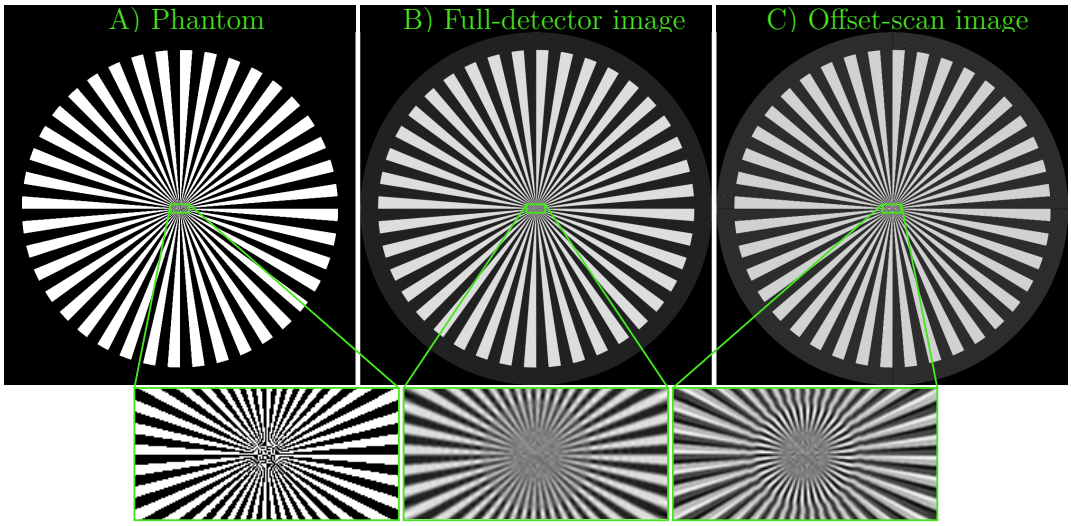

Fig. 4.17: A 40-pronged Siemens star and its full-detector and offset-scan reconstructions, with details of the central area.

The Shepp-Logan phantom (fig. 4.18) shows relatively high values of both FSIM and PSNR. This is likely due to the phantom containing less high-contrast edges compared to the other datasets, which led to less streak artifacts in reconstructions. Inspection of both the images reveals no noticeable differences.

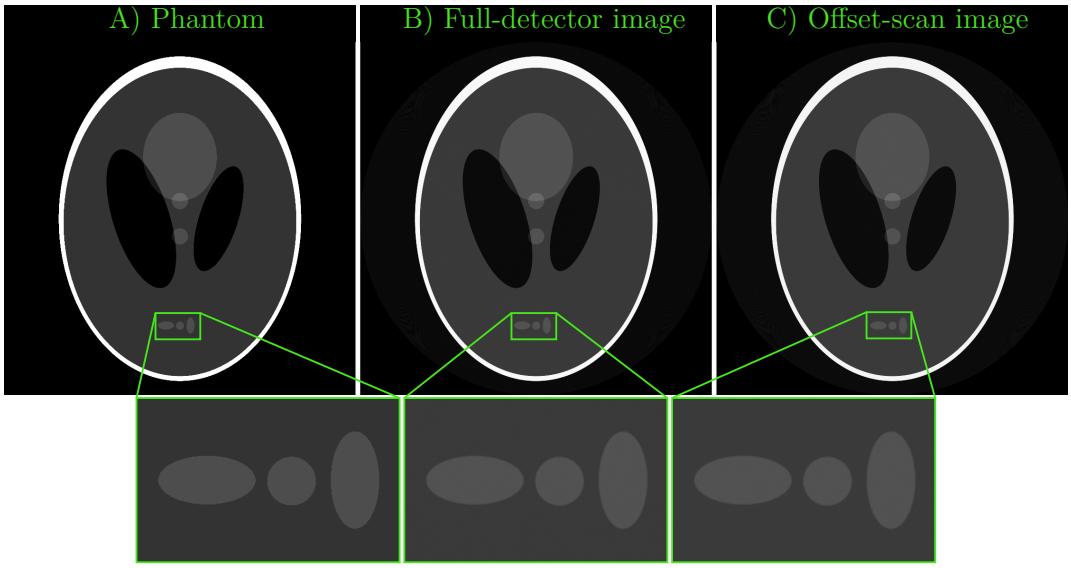

Fig. 4.18: The Shepp-Logan phantom (A) and its full-detector (B) and offset-scan (C) tomograms, with details showing the three small ellipses in the lower part of the phantom.

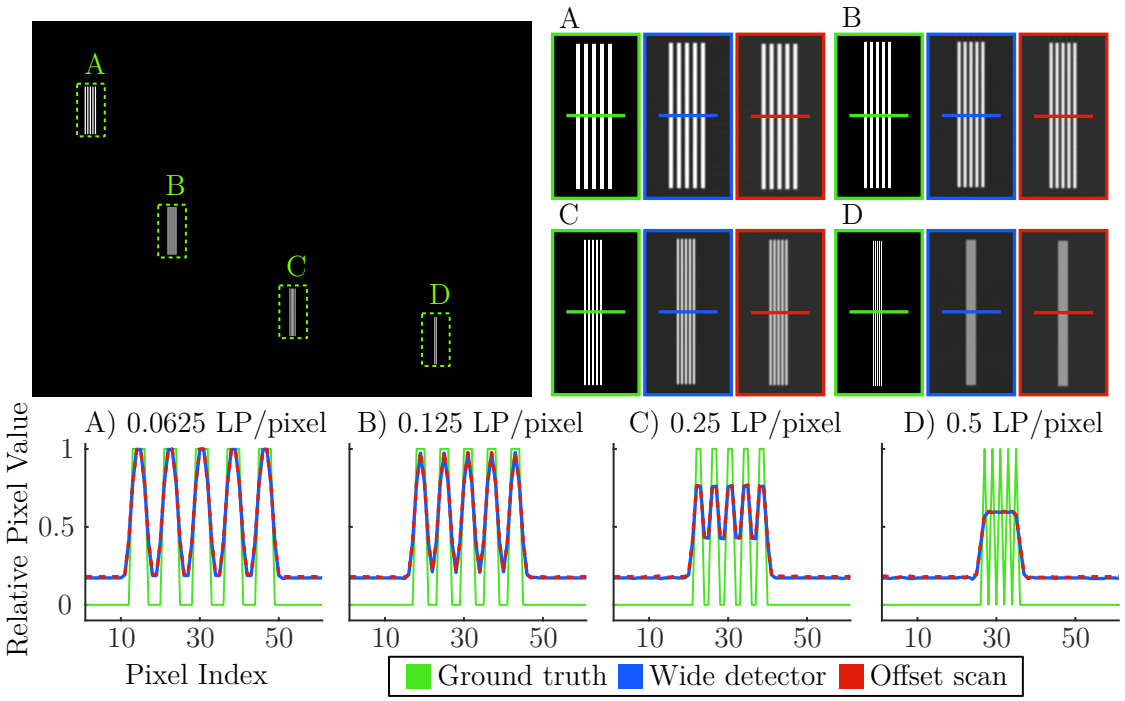

Fig. 4.19: Profiles through patterns of LP of various widths in both full-detector and offset-scan data. The top left shows the lower left part of the LP phantom. Details of marked ground truth, full-detector, and offset-scan areas are shown in the upper right. The details' borders are colored according to which image they represent. Profiles were taken along the marked lines in these details, and plotted below.

Line profiles from both reconstructions of the LP phantom are plotted in fig. 4.19. They show that both images are similar in terms of perceived resolution. Neither reconstruction was able to resolve the most detailed LP pattern. Presumably, this is due to the inherent low-pass nature of the backprojection operation, coupled with apodization of the ramp filter. Therefore, loss of detail caused by utilizing offset-scan FoV extension does not appear to be a concern, at least for the particular scan geometry and setup used.

Real data

Mean NIQE values for all reconstructions are listed in table 4.7. According to these values, full-detector and offset-scan data show similar levels of quality. This somewhat mirrors the objective evaluation of simulated data, although it should be noted that the measurement geometry was not exactly the same here. Most notably, full-detector data was only acquired over a short-scan range, instead of a full 2π one.

Tab. 4.7: Mean NIQE index values for all three datasets. The last column features the percentual difference of offset-scan values when compared to full-detector ones (the lower the number, the better).

Sample	Mean NIQE, full-detector data	Mean NIQE, offset-scan data	Difference of offset- and full-scan [%]
Construction toy piece	5.0047	5.5381	10.65
Pill	4.4242	4.2683	-3.52
Carbon fiber reinforced polymer	4.8276	4.8374	0.20

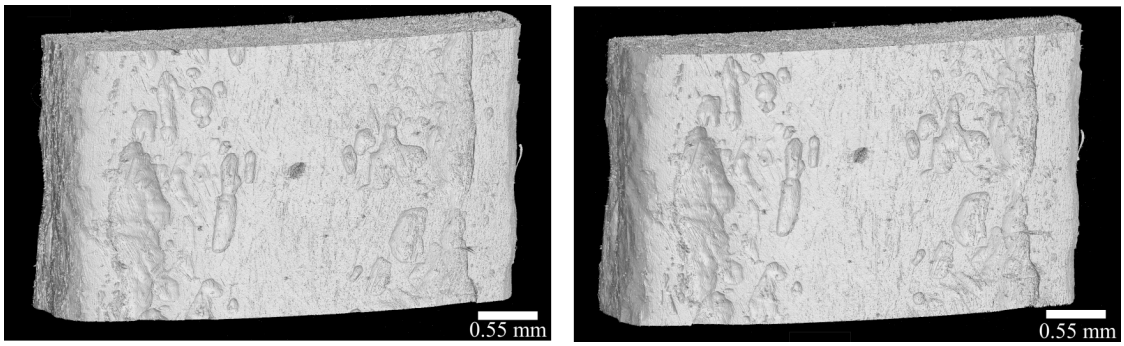

Fig. 4.20: Rendered surface model of the reconstructions of the carbon fiber reinforced polymer. The surface of the full-detector reconstruction is on the left, the offset-scan surface is on the right.

Three-dimensional surface models of both reconstructions of the polymer sample are shown in fig. 4.20. Renders for the other two samples are included in fig. A.2 in appendix A. VGStudio Max 3.3 was used for surface determination and rendering. The models contain moderate amounts of noise, which is due in part to the aforementioned lack of preprocessing. Superficially, there is little difference between the shapes of corresponding surface models, suggesting that offset-scan and full-detector data are both equally viable for further volumetric analysis.

In figures 4.21, 4.22, and 4.23, an effort was made to show details of corresponding areas. There are minor differences, such as a slightly different orientation of the sample. Manipulation of samples between offset and full-detector scans was necessary, and resulted in slight changes in their position. No correction of these differences was performed, as these do not impact objective or subjective evaluation.

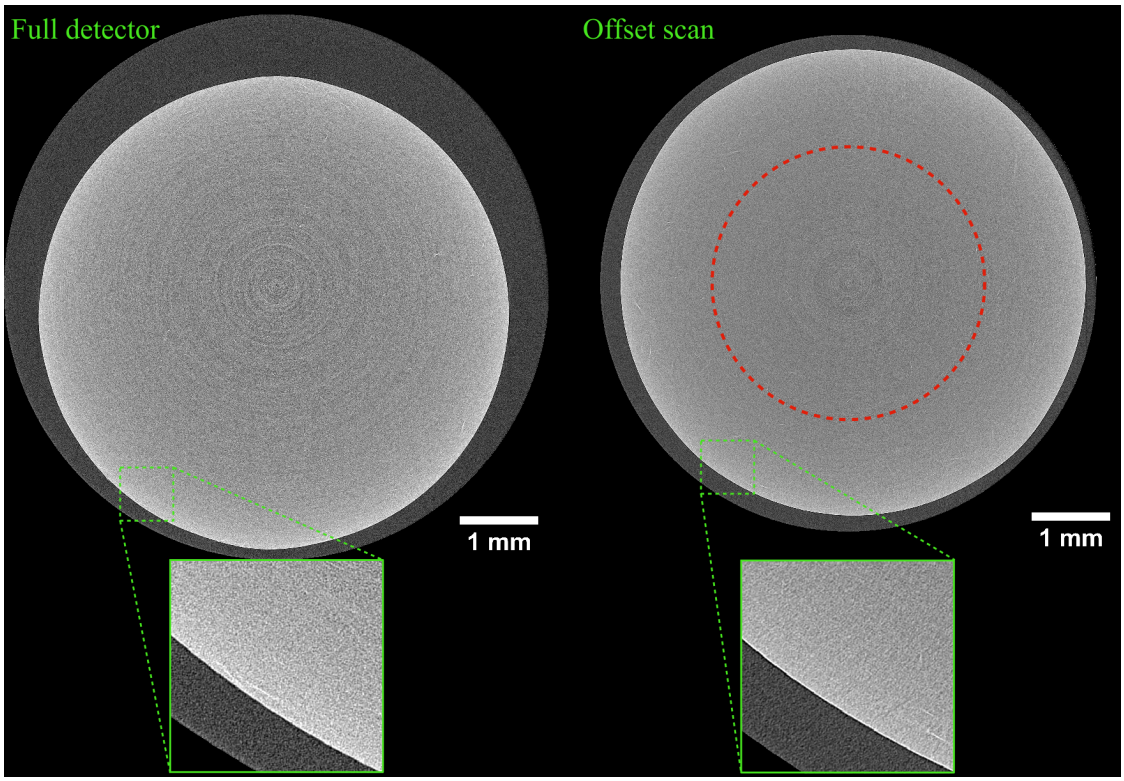

Fig. 4.21: Cross-sections of both reconstructions of the construction toy piece. The original FoV of the 5× unit is shown by a green circle in the offset-scan slice. Magnified details are included, showing the difference in ring artifact prominence.

Figure 4.21 shows representative slices of the toy piece sample reconstructed from both offset-scan and full-detector data. The sample is a homogeneous plastic piece, and a beam hardening artifact is visible in both slices. The magnitude of the artifact is similar in both cases. The discrepancy between NIQE indices for both datasets of this sample is large compared to the other two examples. Because NIQE

is not aware of specific types of distortion, it is not clear what this difference was caused by. Visual inspection of reconstructed slices did not reveal any significant subjective quality difference.

Slices of reconstructions of the pill (fig. 4.22) show noticeable beam hardening and streak artifacts, resulting in disproportionately high gray values and streaks along the edges. Once again, the severity of artifacts in both images is approximately the same, and no additional errors are apparent in the offset-scan case. Interestingly, the NIQE indices for this sample indicate the offset-scan dataset is of higher quality than the full-scan one. This may be due to a lower number of ring artifacts, an effect of binning that is discussed later. Other factors may have contributed to the slight superiority of offset-scan data quality in this case, but these were not successfully identified here.

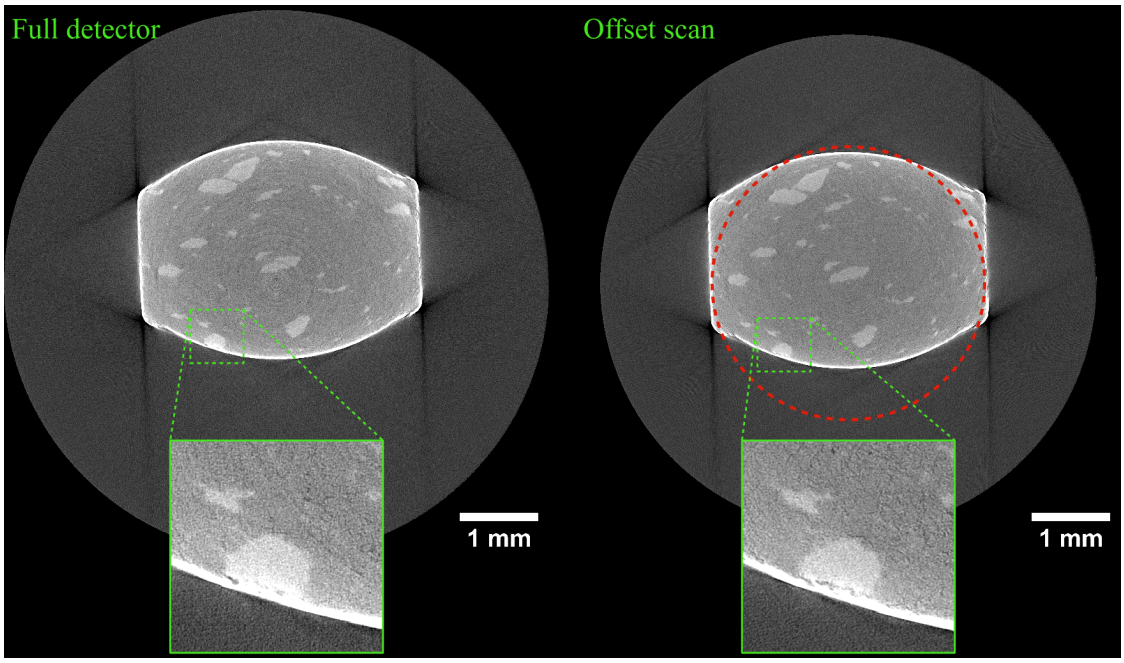

Fig. 4.22: Cross-sections of both reconstructions of the pill sample. The original FoV and details are shown as in fig. 4.21.

The final and most complex sample is represented by slices in fig. 4.23. Because the sample was significantly less dense and thinner than the previous two, no severe streak or cupping artifacts are present. However, motion artifacts degrade both slices. This is likely due to motion of different parts of the sample relative to one another throughout the scan, because the artifacts vary with position, and are present in both reconstructions. In terms of shapes of structures and contrast, no significant difference was identified. The quality of both datasets according to NIQE is almost the same.

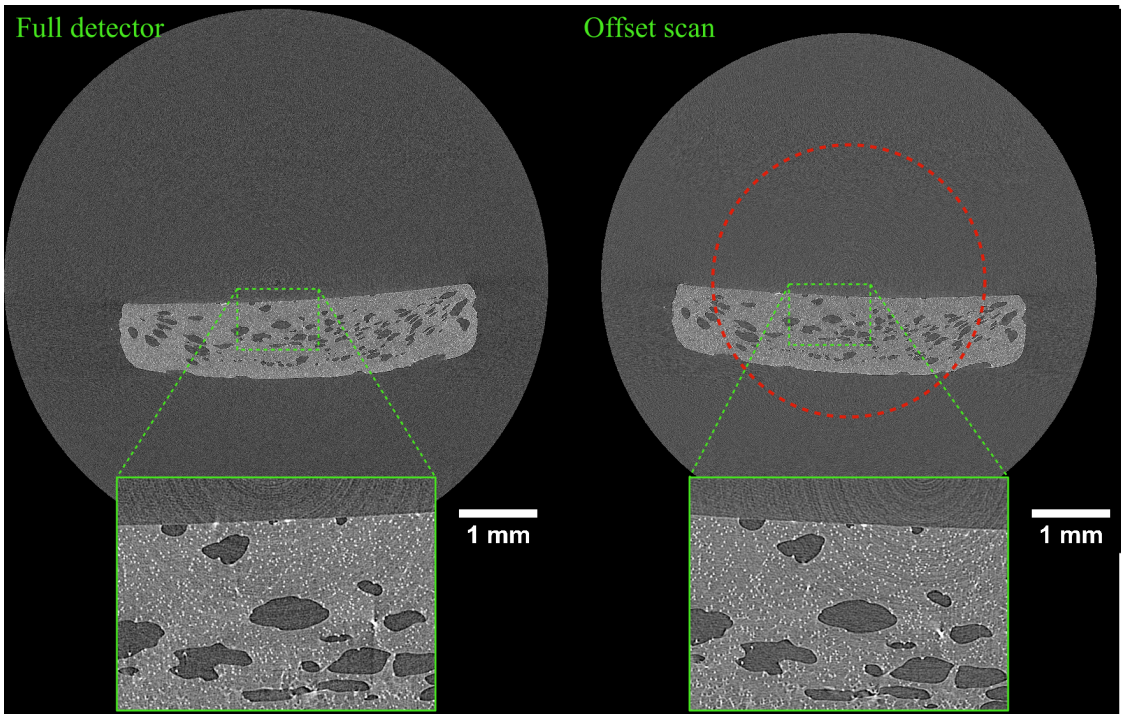

Fig. 4.23: Cross-sections of both reconstructions of the carbon fiber reinforced polymer. The original FoV and details are shown as in fig. 4.21.

There are differences between the test offset-scan and full-detector datasets that do not stem directly from the applied FoV extension method, but rather are a by-product of the particular scan settings used. Offset-scan slices, particularly the toy and pill samples (fig. 4.21 and 4.22), contain a lower amount of ring artifacts, which are caused by unbalanced responses of individual elements of the detector array. Binning tends to reduce these effects, as it groups responses of neighboring pixels, reducing their variance. As a result, using the offset-scan technique with the 5× optical unit and binning can lead to reconstructions with a similar FoV, quality, and resolution as a standard measurement with a 2.5× lens unit, while reducing the amount of ring artifacts. Additionally, binning leads to a reduced scan duration, as it effectively increases the sensitive area of detector elements at the cost of a larger pixel size. For the three test samples, offset scans acquisitions required about two thirds of the time necessary for their full-detector counterparts.

Conclusion

Computed tomography is a popular method for non-destructive evaluation of samples. A major limitation of CT is the size of the FoV, which is generally given by the size of the detector array used. To extend the FoV of a CT scanner, a larger detector may be used. Though straightforward, this solution is often infeasible due to financial, technical, or other constraints. Instead, one may utilize a different data acquisition and processing strategy, which allows for a FoV larger than the detector array used. Such an approach can provide results comparable to data acquired using a larger detector, and it is often more practical than a hardware-based solution.

A method for extending the FoV of the Rigaku Nano3DX X-ray microscope was proposed in this work. In particular, the FoV of this device was extended laterally by offsetting the AoR of the scanned sample to one side. The Nano3DX already offers a means of offsetting the AoR, so the implemented method requires no modification of the scanner's hardware. The proposed approach is relatively simple to implement and compatible with standard cone-beam reconstruction algorithms.

The method was tested on synthetic and real data, which were both chosen to contain a wide range of structures of varying complexity. Samples for real data were additionally picked to resemble some of the typical use cases of the device. The validity of the implemented FoV extension method was evaluated subjectively and objectively, based on comparisons between its results and reconstructions of data acquired using a wider detector.

Results of the tests are considered to be in favor of the proposed FoV extension method. For both simulated and real data, the quality of reconstructions with an extended FoV is comparable with reconstructions of a standard measurement using a larger detector. The achieved extended FoV during tests was roughly 1.8 times that of the original. The amount of extension using this method is limited to less than twice the size of the detector array, but this limitation is compensated by the ease of implementation this approach offers.

The increased FoV allows the Nano3DX to acquire projection data for a wider range of samples, and the implemented approach has the potential to be seamlessly integrated into existing scan protocols. Further tests are planned to test the limits of the proposed method and investigate the robustness of automatic AoR determination. Once this is finished, the method is to be incorporated into already existing tomographic software developed by Rigaku.

Bibliography

[1] MARTZ JR., Harry E., Clint M. LOGAN, Daniel J. SCHNEBERK and Peter J. SHULL. *X-ray imaging: fundamentals, industrial techniques, and applications*. Boca Raton: Taylor & Francis, CRC Press, 2017. ISBN 978-0-8493-9772-1.

[2] JAN, Jiří. *Medical image processing, reconstruction, and restoration: concepts and methods*. Boca Raton, FL: CRC Press, Taylor and Francis Group, 2006. ISBN 978-0-8247-5849-3.

[3] FESSLER, J.A. Fundamentals of CT Reconstruction in 2D and 3D. *Comprehensive Biomedical Physics* [online]. Amsterdam: Elsevier, 2014, 2014, s. 263-295 [cit. 2019-11-01]. DOI: 10.1016/B978-0-444-53632-7.00212-4. ISBN 9780444536334.

[4] KAMPSCHULTE, M., A. LANGHEINIRCH, J. SENDER, et al. Nano-Computed Tomography: Technique and Applications. *RöFo - Fortschritte auf dem Gebiet der Röntgenstrahlen und der bildgebenden Verfahren*. 2016, **188**(02), 146-154. DOI: 10.1055/s-0041-106541. ISSN 1438-9029.

[5] KYRIELEIS, A., M. IBISON, V. TITARENKO and P.J. WITHERS. Image stitching strategies for tomographic imaging of large objects at high resolution at synchrotron sources. *Nuclear Instruments and Methods in Physics Research Section A: Accelerators, Spectrometers, Detectors and Associated Equipment*. 2009, **607**(3), 677-684. DOI: 10.1016/j.nima.2009.06.030. ISSN 01689002.

[6] WANG, Ge. X-ray micro-CT with a displaced detector array. *Medical Physics*. 2002, **29**(7), 1634-1636. DOI: 10.1118/1.1489043. ISSN 00942405.

[7] GREGOR, J., S.S. GLEASON and M.J. PAULUS. Conebeam X-ray computed tomography with an offset detector array. In: *Proceedings 2003 International Conference on Image Processing (Cat. No.03CH37429)*. Barcelona: IEEE, 2003, II-803-6. DOI: 10.1109/ICIP.2003.1246802. ISBN 0-7803-7750-8. ISSN 1522-4880.

[8] LIFENG YU, C. PELIZZARI, XIAOCHUAN PAN, H. RIEM, P. MUNRO and W. KAISSL. Application of asymmetric cone-beam CT in radiotherapy. In: *IEEE Symposium Conference Record Nuclear Science 2004*. Beijing: IEEE, 2004, s. 3249-3252. DOI: 10.1109/NSSMIC.2004.1466376. ISBN 0-7803-8700-7. ISSN 1082-3654.

[9] CHEN, Yunbin, Hao CHEN, Shoutao LI and Yuan WANG. An ICT Reconstruction Algorithm for Rotation Off-Centered Scan. In: *DIR 2015*. Ghent: NDT.net, 2015, s. 1-10. ISSN 1435-4934. Available at: pdfs.semanticscholar.org/c1e6/65f144a4b05e60d199f188e8787668446929.pdf

[10] FRAKNOI, Andrew, David MORRISON and Sidney C. WOLFF. *Astronomy*. Houston: OpenStax, 2016. ISBN 1-947172-24-7. Available at: https://openstax.org/details/books/astronomy

[11] KAK, Avinash C. and Malcolm SLANEY. *Principles of computerized tomographic imaging*. New York: IEEE Press, 1999. ISBN 08-794-2198-3.

[12] HOHEISEL, Martin. Review of medical imaging with emphasis on X-ray detectors. *Nuclear Instruments and Methods in Physics Research Section A: Accelerators, Spectrometers, Detectors and Associated Equipment*. 2006, **563**(1), 215-224. DOI: 10.1016/j.nima.2006.01.123. ISSN 01689002.

[13] DU PLESSIS, Anton, Stephan Gerhard LE ROUX and Anina GUELPA. Comparison of medical and industrial X-ray computed tomography for non-destructive testing. *Case Studies in Nondestructive Testing and Evaluation*. 2016, **2016**(6), 17-25. DOI: 10.1016/j.csndt.2016.07.001. ISSN 22146571.

[14] POLUDNIOWSKI, Gavin G. and Philip M. EVANS. Calculation of x-ray spectra emerging from an x-ray tube. Part I. Electron penetration characteristics in x-ray targets. *Medical Physics*. 2007, **34**(6Part1), 2164-2174. DOI: 10.1118/1.2734725. ISSN 00942405.

[15] POLUDNIOWSKI, Gavin G. and Philip M. EVANS. Calculation of x-ray spectra emerging from an x-ray tube. Part II. X-ray production and filtration in x-ray targets. *Medical Physics*. 2007, **34**(6Part1), 2175-2186. DOI: 10.1118/1.2734726. ISSN 00942405.

[16] POLUDNIOWSKI, Gavin G., Guillaume LANDRY, François DEBLOIS, Philip M. EVANS and Frank VERHAEGEN. SpekCalc: a program to calculate photon spectra from tungsten anode x-ray tubes. *Physics in Medicine and Biology*. 2009, **54**(19), N433-N438. DOI: 10.1088/0031-9155/54/19/N01. ISSN 0031-9155.

[17] KAZEROONI, Ella A. High-Resolution CT of the Lungs. *American Journal of Roentgenology*. 2001, **177**(3), 501-519. DOI: 10.2214/ajr.177.3.1770501. ISSN 0361-803X.

[18] GELB, Jeff, Michael FESER, Andrei TKACHUK, et al. Sub-micron X-ray Computed Tomography for Non-Destructive 3D Visualization and Analysis. *Microscopy and Microanalysis*. 2009, **15**(S2), 618-619. DOI: 10.1017/S1431927609093623. ISSN 1431-9276.

[19] FELLA, Christian, Andreas BALLES, Randolf HANKE, Arndt LAST and Simon ZABLER. Hybrid setup for micro- and nano-computed tomography in the hard X-ray range. *Review of Scientific Instruments*. 2017, **88**(12), 123702-1 - 123702-11. DOI: 10.1063/1.5011042. ISSN 0034-6748.

[20] TOUŠ, Jan, Martin HORVÁTH, Ladislav PÍNA, Karel BLAŽEK and Bruno SOPKO. High-resolution application of YAG:Ce and LuAG:Ce imaging detectors with a CCD X-ray camera. *Nuclear Instruments and Methods in Physics Research Section A: Accelerators, Spectrometers, Detectors and Associated Equipment*. 2008, **591**(1), 264-267. DOI: 10.1016/j.nima.2008.03.070. ISSN 01689002.

[21] LI, Baolei, Yaojun ZHANG a Yang MO. Measurement of center of rotation for projection in x-ray two-dimensional computed tomography system. *Proc. of SPIE*. 2010, 2010-8-24, **7544**(75445O), 75445O-. DOI: 10.1117/12.885217.

[22] ZENG, Gengsheng Lawrence. 3D Image Reconstruction. *Medical Image Reconstruction*. Berlin, Heidelberg: Springer Berlin Heidelberg, 2010, 2010, s. 87-123. DOI: 10.1007/978-3-642-05368-9_5. ISBN 978-3-642-05367-2.

[23] TUY, Heang K. An Inversion Formula for Cone-Beam Reconstruction. *SIAM Journal on Applied Mathematics*. 1983, **43**(3), 546-552. DOI: 10.1137/0143035. ISSN 0036-1399.

[24] ZENG, Gengsheng L. Revisit of the Ramp Filter. *IEEE Transactions on Nuclear Science*. 2015, **62**(1), 131-136. DOI: 10.1109/TNS.2014.2363776. ISSN 0018-9499.

[25] FELDKAMP, L. A., L. C. DAVIS and J. W. KRESS. Practical cone-beam algorithm. *Journal of the Optical Society of America A*. 1984, **1**(6), 612-619. DOI: 10.1364/JOSAA.1.000612. ISSN 1084-7529.

[26] KABANIKHIN, S. I. Definitions and examples of inverse and ill-posed problems. *Journal of Inverse and Ill-posed Problems*. 2008, **16**(4), 317-357. DOI: 10.1515/JIIP.2008.019. ISSN 0928-0219.

[27] BEISTER, Marcel, Daniel KOLDITZ and Willi A. KALENDER. Iterative reconstruction methods in X-ray CT. *Physica Medica*. 2012, **28**(2), 94-108. DOI: 10.1016/j.ejmp.2012.01.003. ISSN 11201797.

[28] SHEN, Chenyang, Yesenia GONZALEZ, Liyuan CHEN, Steve B. JIANG and Xun JIA. Intelligent Parameter Tuning in Optimization-Based Iterative CT Reconstruction via Deep Reinforcement Learning. *IEEE Transactions on Medical Imaging*. 2018, **37**(6), 1430-1439. DOI: 10.1109/TMI.2018.2823679. ISSN 0278-0062.

[29] YE, Dong Hye, Somesh SRIVASTAVA, Jean-Baptiste THIBAULT, Ken SAUER and Charles BOUMAN. Deep Residual Learning for Model-Based Iterative CT Reconstruction Using Plug-and-Play Framework. In: *2018 IEEE International Conference on Acoustics, Speech and Signal Processing (ICASSP)*. Calgary, AB, Canada: IEEE, 2018, 2018, s. 6668-6672. DOI: 10.1109/ICASSP.2018.8461408. ISBN 978-1-5386-4658-8. ISSN 2379-190X.

[30] SRIDHAR, Venkatesh, Gregery T. BUZZARD and Charles A. BOUMAN. Distributed Framework for Fast Iterative CT Reconstruction from View-subsets. *Electronic Imaging*. 2018, **2018**(15), 102-1-1027. DOI: 10.2352/ISSN.2470-1173.2018.15.COIMG-102. ISSN 2470-1173.

[31] HA, Sungsoo and Klaus MUELLER. A GPU-Accelerated Multivoxel Update Scheme for Iterative Coordinate Descent (ICD) Optimization in Statistical Iterative CT Reconstruction (SIR). *IEEE Transactions on Computational Imaging*. 2018, **4**(3), 355-365. DOI: 10.1109/TCI.2018.2833622. ISSN 2333-9403.

[32] LIN, Qiang, Min YANG, Fanyong MENG, Liang SUN and BIN TANG. Calibration method of center of rotation under the displaced detector scanning for industrial CT. *Nuclear Instruments and Methods in Physics Research Section A: Accelerators, Spectrometers, Detectors and Associated Equipment*. 2019, **2019**(922), 326-335. DOI: 10.1016/j.nima.2018.11.131. ISSN 01689002.

[33] DONATH, Tilman, Felix BECKMANN and Andreas SCHREYER. Automated determination of the center of rotation in tomography data. *Journal of the Optical Society of America A*. 2006, **23**(5), 1048-1057. DOI: 10.1364/JOSAA.23.001048. ISSN 1084-7529.

[34] LIU, Tong and Andrew A. MALCOLM. Comparison between four methods for central ray determination with wire phantoms in micro-computed-tomography systems. Optical Engineering. 2006, textbf45(6), 1-5. DOI: 10.1117/1.2214717. ISSN 0091-3286.

[35] AZEVEDO, S.G., D.J. SCHNEBERK, J.P. FITCH and H.E. MARTZ. Calculation of the rotational centers in computed tomography sinograms. IEEE Transactions on Nuclear Science. 1990, **37**(4), 1525-1540. DOI: 10.1109/23.55866. ISSN 00189499.

[36] JUN, Kyungtaek and Seokhwan YOON. Alignment Solution for CT Image Reconstruction using Fixed Point and Virtual Rotation Axis. *Scientific Reports*. 2017, **7**(1), 1-11. DOI: 10.1038/srep41218. ISSN 2045-2322.

[37] YANG, Yimeng, Feifei YANG, Ferdinand F. HINGERL, et al. Registration of the rotation axis in X-ray tomography. *Journal of Synchrotron Radiation*. 2015, **22**(2), 452-457. DOI: 10.1107/S160057751402726X. ISSN 1600-5775.

[38] VO, Nghia T., Michael DRAKOPOULOS, Robert C. ATWOOD and Christina REINHARD. Reliable method for calculating the center of rotation in parallel-beam tomography. Optics Express. 2014, textbf22(16), 19078-19086. DOI: 10.1364/OE.22.019078. ISSN 1094-4087.

[39] MIN, Yang, Gao HAIDONG, Li XINGDONG, Meng FANYONG and Wei DONGBO. A new method to determine the center of rotation shift in 2D-CT scanning system using image cross correlation. NDT&E International. 2012, **2012**(46), 48-54. DOI: 10.1016/j.ndteint.2011.09.001. ISSN 09638695.

[40] CHENG, Chang-Chieh, Yu-Tai CHING, Pai-Hung KO and Yeukuang HWU. Correction of center of rotation and projection angle in synchrotron X-ray computed tomography. Scientific Reports. 2018, textbf8(1), 1-9. DOI: 10.1038/s41598-018-28149-8. ISSN 2045-2322.

[41] YANG, Xiaogang, Francesco DE CARLO, Charudatta PHATAK a Doga GÜRSOY. A convolutional neural network approach to calibrating the rotation axis for X-ray computed tomography. *Journal of Synchrotron Radiation*. 2017, **24**(2), 469-475. DOI: 10.1107/S1600577516020117. ISSN 1600-5775.

[42] VAN AARLE, Wim, Willem Jan PALENSTIJN, Jan DE BEENHOUWER, Thomas ALTANTZIS, Sara BALS, K. Joost BATENBURG and Jan SIJBERS. The ASTRA Toolbox: A platform for advanced algorithm development in electron tomography. *Ultramicroscopy*. 2015, **2015**(157), 35-47. DOI: 10.1016/j.ultramic.2015.05.002. ISSN 03043991.

[43] VAN AARLE, Wim, Willem Jan PALENSTIJN, Jeroen CANT, et al. Fast and flexible X-ray tomography using the ASTRA toolbox. *Optics Express*. 2016, **24**(22), 25129-25147. DOI: 10.1364/OE.24.025129. ISSN 1094-4087.

[44] BLEICHRODT, Folkert, Tristan VAN LEEUWEN, Willem Jan PALENSTIJN, Wim VAN AARLE, Jan SIJBERS and K. Joost BATENBURG. Easy implementation of advanced tomography algorithms using the ASTRA toolbox with Spot operators. *Numerical Algorithms*. 2016, **71**(3), 673-697. DOI: 10.1007/s11075-015-0016-4. ISSN 1017-1398.

[45] WANG, Ge and Hengyong YU. The meaning of interior tomography. *Physics in Medicine and Biology*. 2013, **58**(16), R161-R186. DOI: 10.1088/0031-9155/58/16/R161. ISSN 0031-9155.

[46] KYRIELEIS, A., V. TITARENKO, M. IBISON, T. CONNOLLEY and P.J. WITHERS. Region-of-interest tomography using filtered backprojection: assessing the practical limits. *Journal of Microscopy*. 2011, **241**(1), 69-82. DOI: 10.1111/j.1365-2818.2010.03408.x. ISSN 00222720.

[47] CHITYALA, Ravishankar, J. Michael FITZPATRICK, Joseph M. REINHARDT, Kenneth R. HOFFMANN, Stephen RUDIN and Daniel R. BEDNAREK. Artifact reduction in truncated CT using sinogram completion. *Proceedings of SPIE–the International Society for Optical Engineering*. 2005, 2005-4-29, **2005**(5747(3), 2110-2117. DOI: 10.1117/12.595450.

[48] ZAMYATIN, Alexander A. and Satoru NAKANISHI. Sinogram Correction Methods Using Sinogram Decomposition. In: *2006 IEEE Nuclear Science Symposium Conference Record*. San Diego, CA, USA: IEEE, 2006, 2006, s. 3438-3440. DOI: 10.1109/NSSMIC.2006.353740. ISBN 1-4244-0560-2. ISSN 1082-3654.

[49] XU, Jingyan, Katsuyuki TAGUCHI and Benjamin M. W. TSUI. Statistical Projection Completion in X-ray CT Using Consistency Conditions. *IEEE Transactions on Medical Imaging*. 2010, **29**(8), 1528-1540. DOI: 10.1109/TMI.2010.2048335. ISSN 0278-0062.

[50] ZHENG, Dandan, Jun LU, Ariel JEFFERSON, et al. A protocol to extend the longitudinal coverage of on-board cone-beam CT. *Journal of Applied Clinical Medical Physics*. 2012, **13**(4), 141-151. DOI: 10.1120/jacmp.v13i4.3796. ISSN 15269914.

[51] JI, Changguo. Accurate 3D data stitching in circular cone-beam micro-CT. *Journal of X-ray science and technology*. 2010, **2010**(18(2), 99-110. DOI: 10.3233/XST-2010-0246.

[52] KATSEVICH, Alexander. Theoretically Exact Filtered Backprojection-Type Inversion Algorithm for Spiral CT. *SIAM Journal on Applied Mathematics*. 2002, **62**(6), 2012-2026. DOI: 10.1137/S0036139901387186. ISSN 0036-1399.

[53] KATSEVICH, Alexander. An improved exact filtered backprojection algorithm for spiral computed tomography. *Advances in Applied Mathematics*. 2004, **32**(4), 681-697. DOI: 10.1016/S0196-8858(03)00099-X. ISSN 01968858.

[54] VARSLOT, T., A. KINGSTON, G. MYERS and A. SHEPPARD. High-resolution helical cone-beam micro-CT with theoretically-exact reconstruction from experimental data. *Medical Physics*. 2011, **38**(10), 5459-5476. DOI: 10.1118/1.3633900. ISSN 00942405.

[55] JIAN, Fu, Lu HONGNIAN, Li BING, Zhang LEI and Sun JINGJING. X-CT imaging method for large objects using double offset scan mode. *Nuclear Instruments and Methods in Physics Research Section A: Accelerators, Spectrometers, Detectors and Associated Equipment*. 2007, **575**(3), 519-523. DOI: 10.1016/j.nima.2007.03.008. ISSN 01689002.

[56] CHEN, Ming, Huitao ZHANG and Peng ZHANG. BPF-based reconstruction algorithm for multiple rotation—translation scan mode. *Progress in Natural Science*. 2008, **18**(2), 209-216. DOI: 10.1016/j.pnsc.2007.07.012. ISSN 10020071.

[57] WANG, Bo, Yongshun XIAO, Daiwei YU and Zhiqiang CHEN. A Novel Designed Small Angle CT System based on Overlay Rotation. In: *2017 IEEE Nuclear Science Symposium and Medical Imaging Conference (NSS/MIC)*. Atlanta: IEEE, 2017, 2017, s. 1-4. DOI: 10.1109/NSSMIC.2017.8532679. ISBN 978-1-5386-2282-7. ISSN 2577-0829.

[58] TAKEDA, Yoshihiro and Kensaku HAMADA. A primer on the use of the nano3DX high-resolution X-ray microscope. *Rigaku Journal*. 2015, **31**(1), 10-15. Available at: http://www.rigaku.com/downloads/journal/RJ31-1/RigakuJournal31-1_10-15.pdf

[59] XSight Micron LC: X-RAY IMAGING DETECTOR: Compact 2D X-ray CCD and sCMOS camera. *Rigaku* [online]. Tokyo: Rigaku Corporation and its Global Subsidiaries, 2020 [cit. 2020-05-05]. Available at: www.rigaku.com/products/detectors/micron-lc

[60] LIN, Qiang, Min YANG, Qiong WU, Bin TANG a Xiaomin ZHANG. A Reconstruction Method Through Projection Data Conversion Under the Displaced Detector Scanning for Industrial Cone-Beam CT. *IEEE Transactions on Nuclear Science*. 2019, **66**(12), 2364-2378. DOI: 10.1109/TNS.2019.2951448. ISSN 0018-9499.

[61] PARKER, Dennis L. Optimal short scan convolution reconstruction for fan beam CT. *Medical Physics*. 1982, **9**(2), 254-257. DOI: 10.1118/1.595078. ISSN 00942405.

[62] WESARG, Stefan, Matthias EBERT and Thomas BORTFELD. Parker weights revisited. *Medical Physics*. 2002, **29**(3), 372-378. DOI: 10.1118/1.1450132. ISSN 00942405.

[63] SCHÄFER, Dirk, Peter VAN DE HAAR and Michael GRASS. Modified Parker weights for super short scan cone beam CT. In: *15th International Meeting on Fully Three-Dimensional Image Reconstruction in Radiology and Nuclear Medicine*. Xi'an: SPIE, 2017, s. 49-52. DOI: 10.12059/Fully3D.2017-11-3106003.

[64] SHEPP, L. A. a B. F. LOGAN. The Fourier reconstruction of a head section. *IEEE Transactions on Nuclear Science*. 1974, **21**(3), 21-43. DOI: 10.1109/TNS.1974.6499235. ISSN 0018-9499.

[65] ATHAR, Shahrukh a Zhou WANG. A Comprehensive Performance Evaluation of Image Quality Assessment Algorithms. *IEEE Access*. 2019, **7**(1), 140030-140070. DOI: 10.1109/ACCESS.2019.2943319. ISSN 2169-3536.

[66] LIN ZHANG, LEI ZHANG, XUANQIN MOU and D. ZHANG. FSIM: A Feature Similarity Index for Image Quality Assessment. *IEEE Transactions on Image Processing*. 2011, **20**(8), 2378-2386. DOI: 10.1109/TIP.2011.2109730. ISSN 1057-7149.

[67] MITTAL, A., R. SOUNDARARAJAN and A. C. BOVIK. Making a "Completely Blind" Image Quality Analyzer. *IEEE Signal Processing Letters*. 2013, **20**(3), 209-212. DOI: 10.1109/LSP.2012.2227726. ISSN 1070-9908.

List of symbols, physical constants and abbreviations

AoR	axis of rotation
ART	algebraic reconstruction technique
CBCT	cone-beam computed tomography
CCD	charge-coupled device
CT	computed tomography
FBP	filtered backprojection
FDK	Feldkamp-Davis-Kress
FFT	Fast Fourier transform
FoV	field of view
FSIM	Feature Similarity Index
FT	Fourier transform
IQA	image quality assessment
LP	line pairs
μ	linear attenuation coefficient
NDE	nondestructive evaluation
NIQE	Natural Image Quality Evaluator
ODD	origin-detector distance
PSNR	peak signal-to-noise ratio
RoI	region-of-interest
RT	Radon transform
SART	simultaneous algebraic recontruction technique
SIRT	simultaneous iterative recontruction technique
SOD	source-origin distance
SDD	source-detector distance

List of appendices

A Supplementary figures

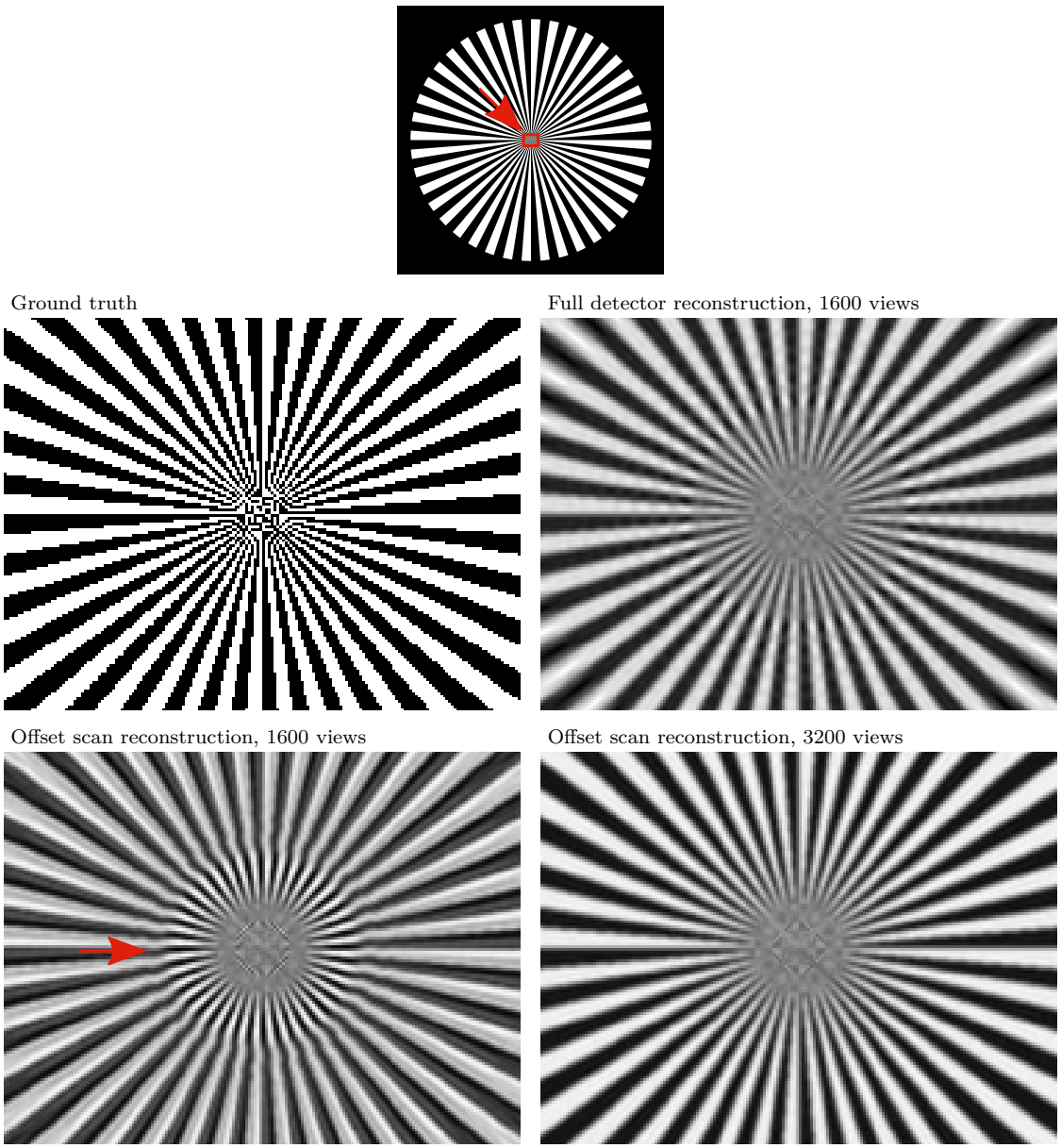

Fig. A.1: Details of the offset-scan Siemens star phantom reconstruction. The top picture shows the location of the shown details. The middle row features the ground truth and a 1600 view full-detector reconstruction. The bottom row showcases a 1600 view offset-scan reconstruction, which appears distorted (an arrow marks the distorted area), and a 3200 view offset-scan reconstruction, which lacks such an artifact.

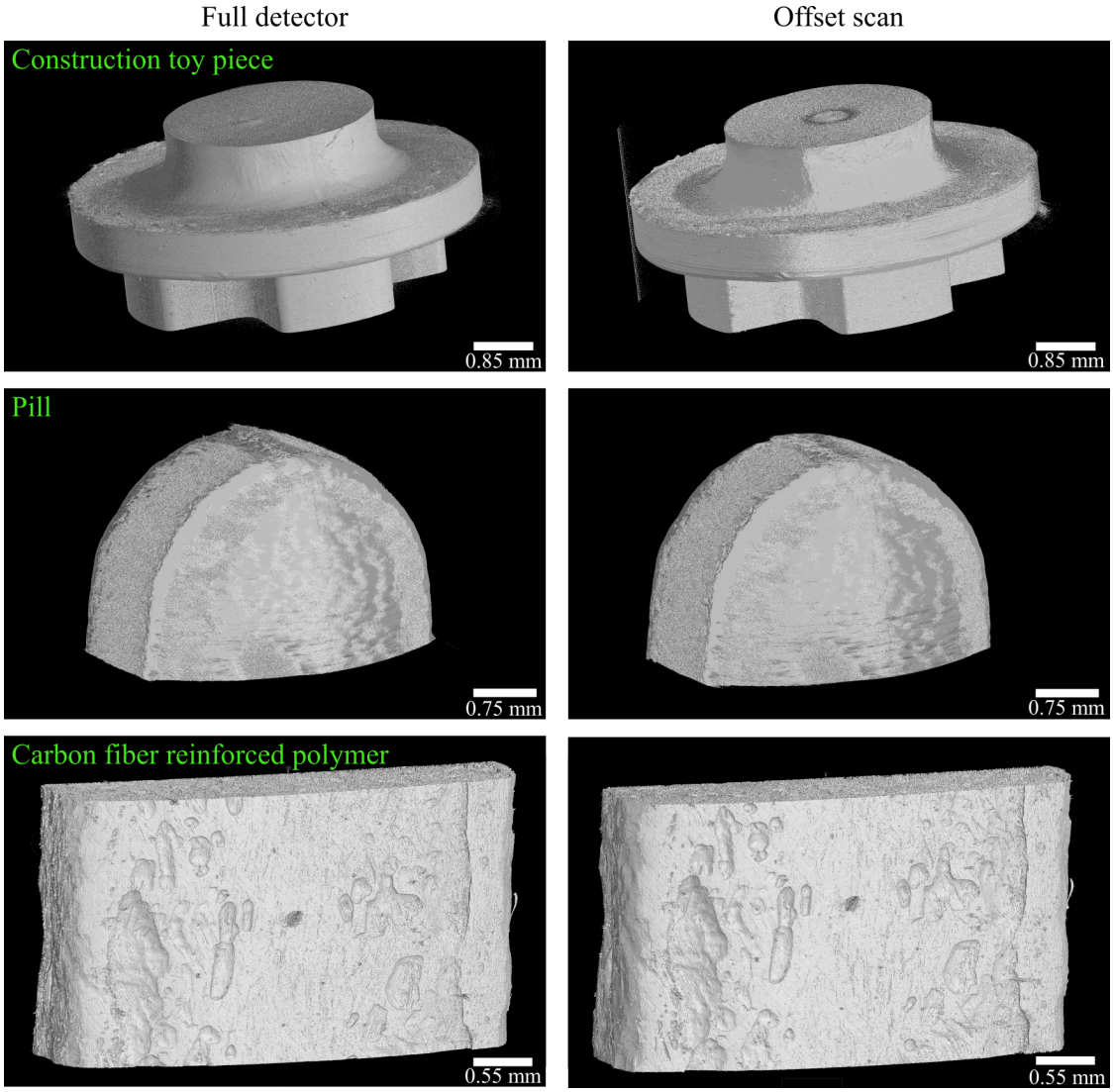

Fig. A.2: Rendered surface models of reconstructions of the three samples used for validation of the implemented FoV extension method's performance. The surface was determined by manually thresholding the gray levels of reconstructions. Full-detector reconstructions using L2160 optics are on the left, while L1080 offset-scan data are on the right. In some models, the lighting of the offset-scan dataset may differ from the full-detector one. This is caused by differences of the position of the sample.

B FSIM copyright notice